

KfK 4802  
Juni 1991

# **Laserspectroscopic Investigations of Isotope Shifts and Hyperfine Structure of Polonium Isotopes**

**D. Kowalewska**  
**Institut für Kernphysik**

**Kernforschungszentrum Karlsruhe**



KERNFORSCHUNGSZENTRUM KARLSRUHE

Institut für Kernphysik

KfK 4802

**Laserspectroscopic Investigations of Isotope Shifts and  
Hyperfine Structure of Polonium Isotopes**

D. Kowalewska \*

\* On leave from Poznan Technical University, Poznan (Poland)

Kernforschungszentrum Karlsruhe GmbH, Karlsruhe

Als Manuskript vervielfältigt  
Für diesen Bericht behalten wir uns alle Rechte vor

Kernforschungszentrum Karlsruhe GmbH  
Postfach 3640, 7500 Karlsruhe 1

ISSN 0303-4003

## Abstract

The isotope shifts and hyperfine structure have been measured for a series of polonium isotopes ( $^{200}\text{Po}$ ,  $^{202}\text{Po}$  and  $^{204}\text{Po}$  to  $^{210}\text{Po}$ ) by laser induced fluorescence on an atomic beam. The optical transition chosen for the investigations was the E1 transition  $6p^4\ ^3P_2 \rightarrow 6p^37s\ ^5S_2$  with the longest possible wavelength  $\lambda = 255.8\text{ nm}$ . In order to induce this UV transition, laser intracavity frequency doubling was applied. For that purpose a commercial ring dye laser system has been considerably modified, in particular the frequency selection scheme has been changed; the rebuilt laser system, as used in this work, is described.

The measurements of the hyperfine structure led to the first determination of the nuclear magnetic dipole moment of  $^{209}\text{Po}$ . From the measured isotope shifts relative changes of the nuclear mean square charge radii  $\delta \langle r^2 \rangle$  have been estimated. Applying a calibration based on a nuclear model, absolute  $\delta \langle r^2 \rangle$  values have been determined. The observed features are discussed in terms of theoretical predictions and compared with experimental data for neighboring elements.

## Laserspektroskopische Untersuchungen der Isotopieverschiebung und Hyperfeinstruktur von Polonium-Isotopen.

### Zusammenfassung

Isotopieverschiebungen und Hyperfeinstruktur wurden mittels laserinduzierter Fluoreszenz an einem Atomstrahl für eine Reihe von Polonium-Isotopen ( $^{200}\text{Po}$ ,  $^{202}\text{Po}$  und  $^{204}$  bis  $^{210}\text{Po}$ ) gemessen. Der benutzte optische Übergang war der E1-Übergang  $6p^4\ ^3P_2 \rightarrow 6p^37s\ ^5S_2$  mit der längstmöglichen Wellenlänge  $\lambda = 255.8\text{ nm}$ . Zur Erzeugung des UV-Lichtes wurde eine Intracavity-Frequenzverdopplung benutzt. Zu diesem Zwecke wurde ein käuflicher Ring-Farbstofflaser erheblich modifiziert, insbesondere wurde die Modenselektion geändert. Das aufgebaute Lasersystem wird beschrieben.

Die Hyperfeinstrukturmessungen führten zur erstmaligen Bestimmung des magnetischen Dipolmomentes von  $^{209}\text{Po}$ . Aus den gemessenen Isotopieverschiebungen wird die Variation der mittleren quadratischen Radien  $\delta \langle r^2 \rangle$  der Ladungsverteilungen der Atomkerne bestimmt. Die Eichung der  $\delta \langle r^2 \rangle$ -Werte erfolgt an einem theoretischen Modell. Die Beobachtungen werden in Zusammenhang mit theoretischen Voraussagen und im Vergleich zu Daten von Nachbarelementen diskutiert.

# Contents

## Abstract

1	Introduction	1
2	Experimental method and setup	3
	2.1 Choice of the atomic transition	3
	2.2 Spectral resolution vs sensitivity	4
	2.3 Experimental setup	4
3	The atomic beam apparatus	5
	3.1 Generation of the Po atomic beam	6
	3.2 Collimation of the atomic beam	7
	3.3 Detection system	7
4	Laser system	8
	4.1 Laser resonator configuration	10
	4.2 Dyes	16
	4.3 Pump waist	21
	4.4 Single-mode selection, frequency stabilization and scanning	21
	a) Single-mode selection	21
	b) Frequency stabilization	23
	c) Frequency scanning	24
	4.5 Intracavity losses	25
	4.6 Intracavity frequency doubling in a BBO crystal	27
	a) Theoretical considerations	27
	b) Practical use	29
	c) Mounting	30
	d) UV output	32
	e) Crystal degradation	32
	4.7 UV transport optics	35
	4.8 Controls	36
5	Experiments	37
	5.1 Isotope production and sample preparation	37
	5.2 Measurement programs	40
	5.3 Signal and background count rates	41
	a) Background count rates	41
	b) Signal ratio	41
	c) Total signal count rates - crucible comparison	42
	5.4 Isotope shift and hyperfine structure measurements	42

a)	Even-mass isotopes	42
b)	Odd-mass isotopes	45
6	Data evaluation	47
6.1	Fits of the spectra	47
6.2	Frequency axis	48
6.3	Identification of hyperfine components	49
a)	General	49
b)	$^{209}\text{Po}$	50
c)	$^{207}\text{Po}$	54
d)	$^{205}\text{Po}$	60
7	Results	61
7.1	Measured isotope shifts and HFS factors	61
a)	Total experimental errors	61
b)	Results	63
7.2	Mean square charge radii	64
a)	Global features	64
b)	Odd-even staggering	68
7.3	Hyperfine structure and nuclear moments	69
8	Discussion	71
8.1	Mean square charge radii	71
a)	Global features	71
b)	Deformation	74
c)	Odd-even staggering	75
d)	Comparison with the neighboring elements	76
8.2	Nuclear moments	78
9	Concluding remarks	79
	Appendix: Second harmonic generation	81
	References	87

## 1 Introduction

Optical spectroscopy, in particular its modern variant - laser spectroscopy [De 73] has proved to be one of the most useful experimental methods for systematic studies of the nuclear ground state structure. It provides information on size and shape of the charge distribution, i.e. the variation of nuclear charge radii in isotopic chains which can be extracted from the isotope shifts observed in optical transitions, and electromagnetic moments, obtained from the hyperfine splitting of the electronic energy levels. Thus it provides a basis for tests of nuclear structure models. Relevant information on these and related quantities is also accessible to various other methods of nuclear spectroscopy, sometimes more directly and with less problems concerning the interpretation [BFG 89]. The great advantage of laser spectroscopy, however, is its high sensitivity which makes it especially useful whenever radioactive species are concerned, i.e. when only very small sample sizes are available due to production or radioactive safety limits. In fact, laser spectroscopy is the only experimental method for systematic studies of nuclear charge radii of radioactive nuclides.

Until now larger regions of the chart of the nuclides have been investigated by laser spectroscopy [Re 89, Ot 89], yet there are still gaps remaining in regions where conventional nuclear spectroscopy has revealed interesting and peculiar features of nuclear structure. One such gap is located in the vicinity of the proton shell closure at  $Z = 82$ . This region has become of particular interest in the recent years as unexpected strong quadrupole deformations and shape instabilities along the isotope chain have been discovered there for neutron-deficient isotopes of mercury [BHK 76, UBD 86], gold [WBB 87] and platinum [DSB 86]. All these elements lie, however, below the shell closure whereas no data were available concerning the elements directly above it (bismuth, polonium and astatine). The present experiment involving the studies of a series of polonium isotopes was first of all motivated to fill in the existing gap and possibly look for similar phenomena as these observed below  $Z = 82$ , if a sufficiently low neutron number could be reached. Neutron-rich isotopes were comparably less interesting as it is already known that the octupole deformation in the vicinity of  $N = 134$ , evident in the Ra-Th region [CTT 85, CTT 87, WAK 87, AKN 88, Kä 88], in  $^{218}\text{Po}$  is very insignificant [NOR 84].

The information on the ground state nuclear structure of polonium, available so far in the literature, has been very scarce. Magnetic dipole moments of the odd-mass isotopes  $^{201,203,205,207}\text{Po}$  have been measured by the method of nuclear magnetic resonance on oriented nuclei (NMR/ON) [Ra 89, HWF 83], with an accu-

racy of 5 - 10%. From the hyperfine structure measurements of the atomic ground state in  $^{205}\text{Po}$  and  $^{207}\text{Po}$  their electric quadrupole moments have been estimated [OAL 61]. No experimental information is available concerning either the absolute values or the changes of the mean square charge radii. Thus the information provided by our measurements can be considered unique in this respect.

The most suitable method for the planned investigations was found the laser induced fluorescence on an atomic beam [RS 82]. This method provides both high sensitivity and high resolution, and moreover a possibility to adjust one of these parameters against the other according to the requirements. This can be done by varying the degree of collimation of the atomic beam and is a very important specific feature of this method. Moreover, the atomic beam method can be used also for isotopes with lifetimes of the order of a few minutes, in contrast to other highly sensitive methods (e.g. laser spectroscopy on stored ions in an ion trap) which require long lifetimes due to the time required to bring the sample into the interaction zone. The method chosen enabled us to study an isotope chain, including the isotopes with lifetimes down to 11.5 min (altogether 9 isotopes:  $^{200}\text{Po}$ ,  $^{202}\text{Po}$ ,  $^{204-210}\text{Po}$ ).

Our measurements are the first to determine the relative changes of the mean square charge radii  $\delta\langle r^2 \rangle$ . Since all Po nuclides are radioactive, methods like electron scattering and measurements of isotope shifts in muonic atoms were not applied so far to this element, as they require samples of considerable size (of the order of milligramms to gramms, compared to nanogramms or even picogramms sufficient for our laser spectroscopic investigations). Hence, there are no experimental data available which could be used for calibration of our isotope shift measurements (as is the usual procedure, cf. [AFG 86]). The only other possibility of calibration is by using some theoretical estimate of the electronic calibration factor, based e.g. on Hartree-Fock calculations. Unfortunately, such estimates are not available until now but adequate calculations are in progress [Fr 90]. Therefore at the moment we give only a preliminary estimate as far as the absolute  $\delta\langle r^2 \rangle$  values are concerned. Nevertheless, since our data are accurate in relative terms, an interesting comparison with neighboring elements (e.g. Pb, Hg) can be performed on the basis of *relative* variations of the mean square charge radii.

## 2 Experimental method and setup

The method chosen for the studies of isotope shifts and hyperfine structure in a series of polonium isotopes was laser induced fluorescence on an atomic beam.

### 2.1 Choice of the atomic transition

For the choice of the transition to be investigated by optical spectroscopy on an atomic beam four criteria had to be taken into account:

- a) transition strength,
- b) population of the lower level,
- c) possibility of detection of the upper level population,
- d) transition frequency.

The choice can be based on an electronic energy level scheme of the element considered. Generally, the most favorable are, of course, E1 transitions from the ground state; the upper level should be a readily decaying one so that the induced fluorescence can be detected.

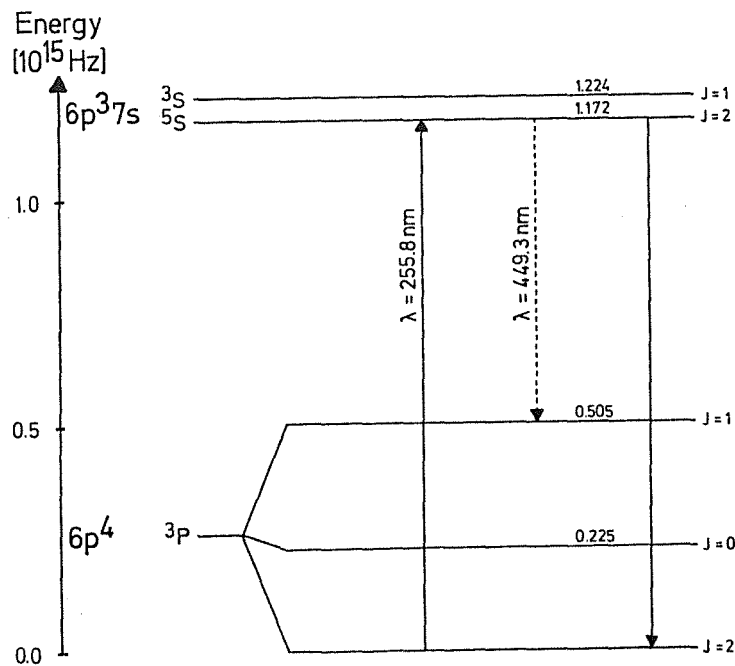


Fig.2.1 Electronic energy level diagram for the Po atom; only the ground term  $^3P$  of the configuration  $6p^4$  and the lowest lying excited terms  $^5S$  and  $^3S$  of the configuration  $6p^3 7s$  are shown.

From the energy level diagram of the Po atom (Fig.2.1) it can be seen that actually only the ground state  $^3P_2$  of the configuration  $6p^4$  can be considered as a starting level of a transition to be studied - the relative Boltzmann population of the first excited level of the ground multiplet  $^3P$  (i.e.  $^3P_0$ ) is only  $\sim 10^{-5}$ , which is rather discouraging from the point of view of the attainable signal strength. Under these circumstances the best possible choice was the transition  $6p^4\ ^3P_2 \rightarrow 6p^37s\ ^5S_2$ , the latter state being the lowest lying state of opposite parity. Nevertheless, the transition wavelength lies in the UV region at  $\lambda = 255.8$  nm. The only way to obtain this wavelength in the cw mode of operation is frequency doubling of light with wavelength  $\lambda = 511.6$  nm. Because of the relatively low efficiency of frequency doubling crystals available for this wavelength range (of the order of 10 - 100  $\mu W/W^2$ ) and relatively low output fundamental power expected (which is normally the case in the wavelength range  $\sim 500$  nm), the straightforward scheme of frequency doubling outside the laser resonator was not expected to provide sufficient UV power for the experiment (rough estimate was 10 - 50  $\mu W$ ), and therefore the intracavity frequency doubling scheme has been chosen. The laser system prepared for this purpose is described in Chapter 4.

As for the detection of the transition chosen, there are two possible ways of the upper level to decay: either to the level  $^3P_1$  at the wavelength  $\lambda = 449.3$  nm or back to the ground state. Of these two the latter one was chosen (see Section 3.3) and used in this work.

## 2.2 Spectral resolution vs sensitivity

In all the spectroscopic methods with reduced Doppler broadening high resolution is achieved at the expense of sensitivity, as only these atoms or ions are effectively used, which happen to have selected velocity components in the direction of the exciting laser beam. The atomic beam method has the advantage of allowing to attain a compromise between the requirements of high resolution and high sensitivity according to the particular case in question. This is done by varying the degree of collimation of the beam. This question is dealt with in more detail in Chapter 3 (Section 3.1).

## 2.3 Experimental setup

The experimental setup used for the laser spectroscopic investigations on polonium atoms consists of:

- a) laser system for generation of light with the required wavelength  $\lambda = 255.8$  nm for excitation of the chosen atomic transition (see Chapter 4);

- b) atomic beam apparatus (see Chapter 3);
- c) data acquisition system:
  - fluorescence detection system (built-in as an integral part of the atomic beam apparatus - see Chapter 3, Section 3.3),
  - computer (measurement programs - see Chapter 5, Section 5.2).

A schematics of the setup is presented in Fig.2.2.

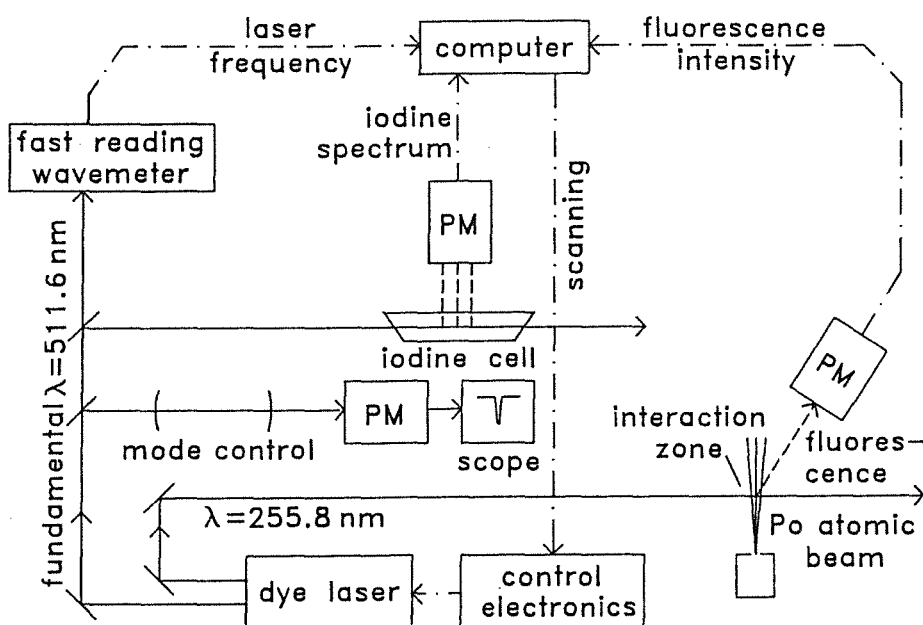


Fig.2.2 Experimental setup - schematics.

### 3 The atomic beam apparatus

The atomic beam apparatus (Fig. 3.1) consists mainly of two vacuum chambers: a lower oven chamber and an upper detection chamber; these are connected by the slit which collimates the atomic beam. The collimated atomic beam is crossed at a right angle by the exciting laser beam and the following fluorescence is detected perpendicular to both. In the following sections the method of the beam collimation, the heating conditions for generation of a polonium atomic beam and the built-in fluorescence detection system are described.

The whole apparatus has been built inside a glove-box to reduce the danger of contamination while handling  $\alpha$ -radioactive samples.

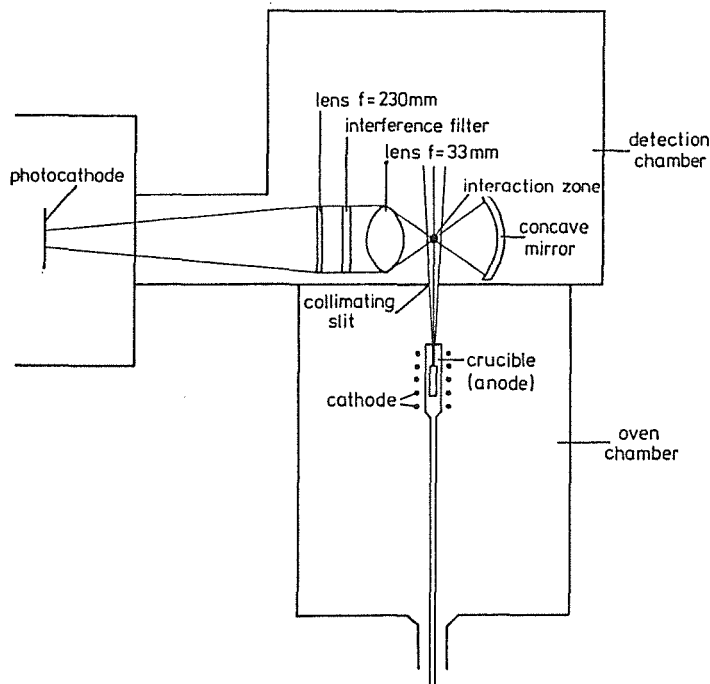


Fig. 3.1 The atomic beam apparatus - schematics.

### 3.1 Generation of the Po atomic beam

The oven is heated by electron bombardment. Details of the electric circuit used for this purpose are described elsewhere [Pi 89].

Initially a special oven construction was used [LJ 59] in order to prevent sample vaporization mainly in molecular form, which was expected otherwise [AO 61]. The particular feature was that the oven was heated only in its upper part. A molybdenum crucible was used, as suggested in [LJ 59]. This scheme was successfully used for the Po isotopes deposited on a Ni- or Ag-foil (for sample forms - see Section 4.1). It could not, however, be maintained for the other sample form, i.e. lead targets. In this case heating in the lower part of the crucible was to be preferred, as polonium atoms were implanted in the bulk of the target material. This scheme has been found to work well for both sample forms used; no precise investigations allowing a quantitative comparison of the two heating schemes with respect to the molecular content have been carried out; a rough comparison, though, revealed no essential differences in their performance. As an alternative to a molybdenum crucible a graphite one has been tried; it was found to perform slightly better (number of counts/ng - see Section 5.3) and henceforth was used for all further experiments. The crucible outlet was a round hole of 1 mm diameter and 10 mm length.

For the generation of a Po atomic beam normally electrical heating powers of 70 - 120 W (routinely  $U = 1.0 - 1.2$  kV,  $I = 40 - 110$  mA) were used. No essential differences were found between the performances of the two kinds of targets (i.e. Ag-foil and Pb targets, see Section 5.1) as far as the heating powers required for generating an atomic beam were concerned. The oven temperatures were not measured directly; these were estimated to range between 500°C and 1000°C.

### 3.2 Collimation of the atomic beam

The atomic beam collimation can be attained by varying the width of the collimating slit (from 8 mm down to 0) as well as the distance of the oven from the slit. In the uppermost position the distance between the slit and the crucible cap, the hole in which provides an outlet for the beam, amounts to 70 mm, for three further positions these distances are 89 mm, 108 mm and 137 mm, respectively. This combination enables obtaining any degree of collimation from 7.3° full angle downwards; the Doppler broadening is thus reduced to at most 6.5% of its full value of 1400 MHz (calculated for 750°C on UV, not laser frequency level), which is in many cases sufficient to resolve the spectrum. With this collimation ~2% of the total number of atoms reach the interaction zone and thus are used, the rest of them is discarded.

The obtained signal strength depends on the number of atoms passing through the interaction zone; therefore a high resolution is achieved at the expense of the signal strength and vice versa. For small samples, what is normally the case for radioactive materials, one must always search for a compromise between these two parameters. In the present experiment usually collimation degrees of 2.5° - 4.1° (slit widths of 2 - 4 mm) were used, which correspond to the following fractions of the total number of atoms passing through the interaction zone: 0.7% - 1.1%.

### 3.3 Detection system

After being excited, the atoms emit fluorescence photons in all possible directions. The fluorescence light should be collected over a possibly large solid angle to assure high sensitivity; therefore the collector optics of the detection system has to be placed as close to the interaction zone as possible. In the apparatus used it has been placed inside the detection chamber.

The detection system is built up as follows. For collecting the fluorescence light a condenser lens with a focal length  $f = 33$  mm and diameter  $\varnothing = 50$  mm is used. On the opposite side of the interaction zone a concave mirror with a focal length  $f = 25$  mm and diameter  $\varnothing = 63$  mm, which covers approximately the same solid

angle  $\Omega = 0.098 \cdot 4\pi$  as the lens, reflects the light towards it. A second lens with focal length  $f = 230$  mm and diameter  $\varnothing = 50$  mm is used to direct the collected fluorescence light onto the photocathode of the photomultiplier. Between the two lenses, where the light is nearly collimated, various filters can be placed to select the detection wavelength. The photon counting electronics used is described in detail elsewhere [Pi 89].

Initially two transitions have been considered for detection: back to the ground state with  $\lambda = 255.8$  nm or to the  $^3P_1$  state (see energy level diagram, Fig. 2.1, Chapter 2) with  $\lambda = 449.3$  nm. The former one is approximately twice as strong as the latter, its disadvantage being, however, that it has the same wavelength as the one exciting. For both wavelengths interference filters were available (Oriel, standard items):

- a)  $\lambda_{\text{centr}} = 253.7$  nm (for a Hg line), FWHM = 36 nm, transmission  $T \approx 35\%$  at the maximum, blocking  $\sim 10^{-5}$ , transmission in the vicinity of 510 nm (twice the central wavelength)  $10^{-4}$  (Oriel, 254 FS40-50);
- b)  $\lambda_{\text{centr}} = 450$  nm, FWHM = 8.5 nm, transmission  $T \approx 50\%$  at the maximum, blocking  $\sim 10^{-5}$  (Oriel, 450 FS10-50).

These data are taken from the transmission curves for these particular items, transmission far from the central wavelength - from the Oriel catalog.

The photomultiplier used was of the type EMI 9635Q, serial No 37096, selected for highest sensitivity in the UV of all the available ones [Pi 89]. The first option looked more promising from the point of view of the sensitivity and since no serious problems with the stray light background were encountered and the sensitivity proved to be sufficient (signal and background count rates - see Chapter 5, Section 5.3), this one has been used throughout. The other detection option at  $\lambda = 449.3$  nm has not been checked.

The signal count rates obtained with this system are discussed in Chapter 5.3.

## 4 Laser system

For intracavity frequency doubling a cw ring dye laser Coherent model CR 699-21 was used. The laser resonator has been modified for that purpose:

- a) the astigmatism compensation rhomb has been removed in order to allow insertion of the frequency doubling crystal into the auxiliary waist;
- b) a new astigmatism compensator has been inserted (see Section 4.1);

- c) the direction of the light propagation in the cavity has been reversed by inverting the permanent magnet of the optical diode.

Fig. 4.1 presents the CR 699-21 resonator adapted for intracavity frequency doubling.

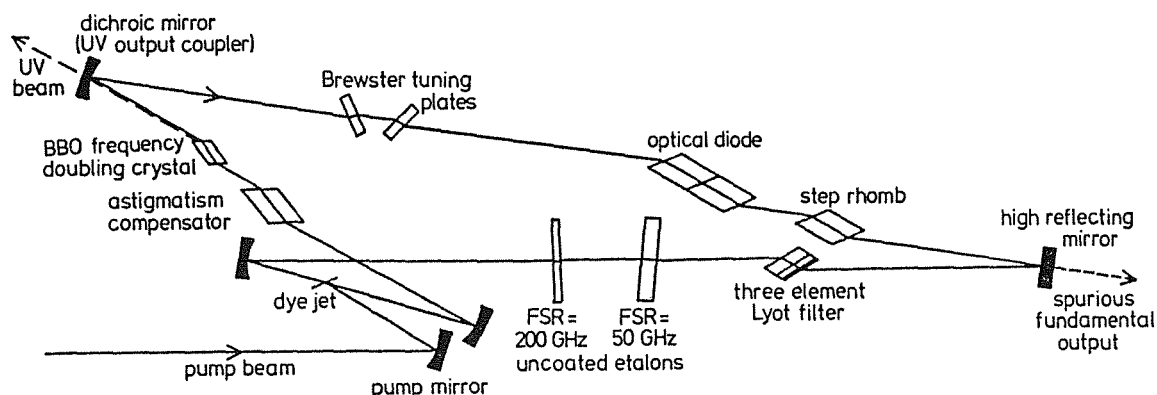


Fig. 4.1 Ring laser resonator Coherent model CR 699-21, modified for intracavity frequency doubling; the modified single mode selection scheme is described in Section 4.4.

The overall geometrical configuration of the resonator remained essentially unchanged with respect to the standard system. The question of the optical stability of the resonator cavity configuration as well as the astigmatism compensation is dealt with in more detail in Section 4.1.

For frequency doubling high intracavity power is required which can be achieved by minimizing the internal losses of the laser resonator; this involved several further alterations (all described in Section 4.4):

- a) the standard output coupler has been replaced by a high-reflecting mirror; the spurious fundamental output beam (a few mW) is fed to the reference cavity for frequency stabilization;
- b) the tuning plate originally mounted close to the output coupling mirror such that the laser beam passes twice through it at about  $2^\circ$  off Brewster's angle, has been replaced by two plates of 2 mm thickness, inserted at Brewster's angle in the upper long arm of the resonator (see Fig. 4.1); thus the introduced reflection loss is minimized. For tuning the two plates are rotated in opposite directions to avoid any misalignment;
- c) the frequency selection scheme has been changed: the standard ICA, used for that purpose has been replaced by less lossy elements, see Section 4.4a.

In order to extract the generated UV light from the resonator, the standard upper fold mirror has been replaced by a mirror with a special dichroic coating (Fig. 4.2) serving as UV output coupler; the transmission of this coating for the fundamental wavelength  $\lambda = 511.6 \text{ nm}$  is 0.3 - 0.4%, for the second harmonic it is more than 80%.

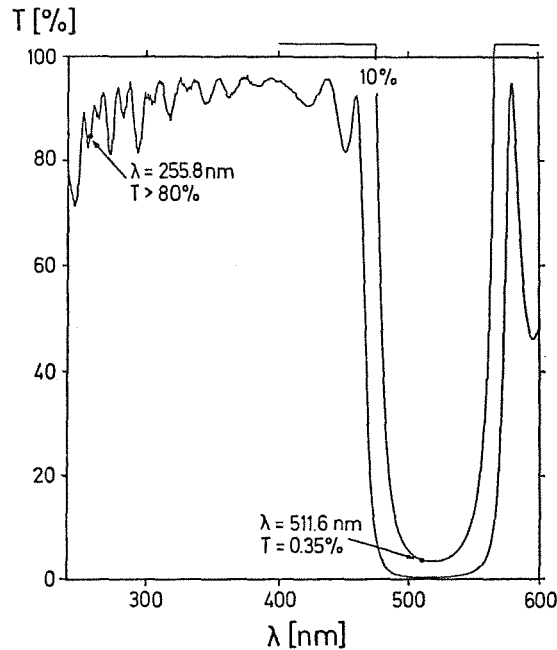


Fig. 4.2 Special dichroic coating for the UV output coupler.

#### 4.1 Laser resonator configuration

The scheme of the CR 699-21 resonator is presented in Fig. 4.3. The geometrical configuration of the resonator remained unchanged. The "tweeter" (piezo-driven mirror, M2 in Fig. 4.3) for the blue-green spectral range has a smaller radius of curvature (75 mm) than that one for Rhodamine 6G. The aim of this change is to obtain tighter waists for lower threshold, as the pump power available for the blue or green is usually low.

Calculations of the optical stability of the resonator configuration have been performed in different degrees of refinement. At first the astigmatism of the resonator was neglected. The results are shown in Fig. 4.4. The values of  $a$  and  $d$  were varied over a wide range while  $b$  was fixed:  $b = 1260 \text{ mm}$ . It has been found that  $b$  is a rather uncritical parameter - no essential differences from the presented results occur if  $b$  is varied by  $\pm 20 \text{ mm}$  off the value quoted.

For the recommended mirror distances M1-M2:  $d = 116 \text{ mm}$  and M1-M3:  $a = 222 \text{ mm}$  the width of the stability range is  $\pm 2.5 \text{ mm}$  for the  $d$  distance and  $\pm 9 \text{ mm}$

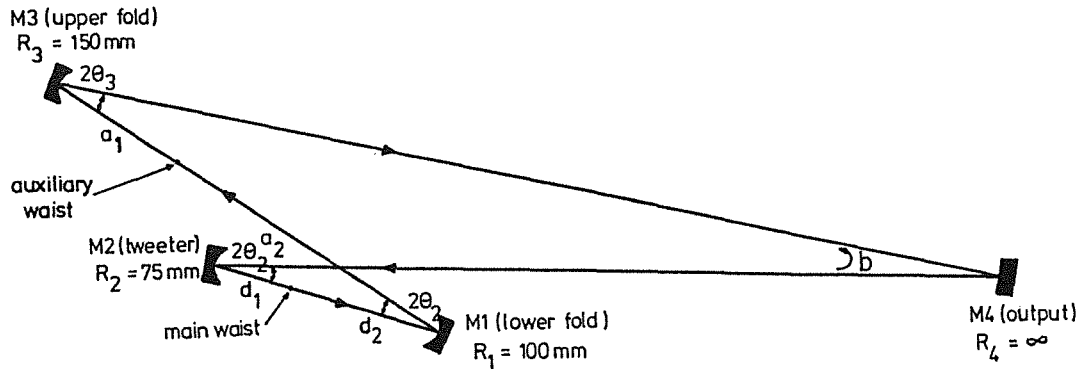


Fig. 4.3 Scheme of the CR 699-21 resonator.

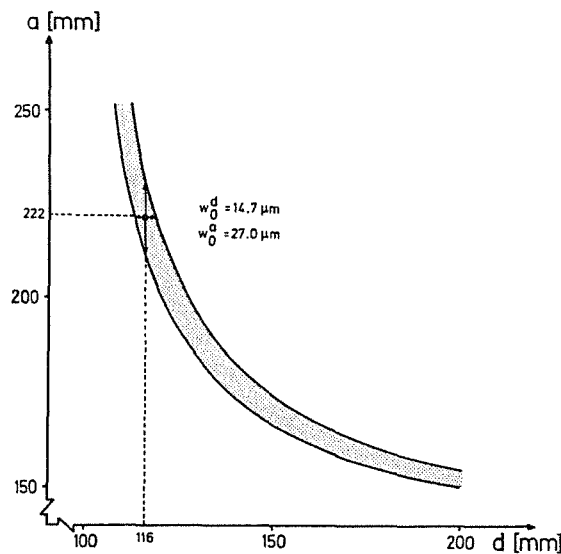


Fig. 4.4 Stability range for the CR 699-21 resonator with the radius of the mirror M2:  $R_2 = 75\text{ mm}$ ;  $d$  denotes the distance M1-M2,  $a$  denotes the distance M1-M3 (see Fig. 4.3). The recommended cavity configuration ( $d = 116\text{ mm}$ ,  $a = 222\text{ mm}$ ) is marked;  $b = 1260\text{ mm}$ , see text.

for the  $a$  distance. Waist sizes in the center of the stability range are as follows:  $w_0^d = 14.7\ \mu\text{m}$  for the main waist (the one in the dye jet - see Fig. 4.3) and  $w_0^a = 27.0\ \mu\text{m}$  for the auxiliary waist.

The actual question of the resonator stability is, however, more complex and refined calculations are required. Because of non-zero angles of incidence at the three curved mirrors astigmatism occurs; the effective focal lengths of the mirrors for the ray bundles perpendicular to the ring plane -  $f_{\perp}$  (sagittal plane) and in the

ring plane -  $f_{\perp}$  (tangential plane) are different. They are given by the formulas [KID 72]:

$$f_{\perp} = f / \cos\Theta > f = R/2, \quad (4.1a)$$

$$f_{\parallel} = f \cdot \cos\Theta < f = R/2. \quad (4.1b)$$

These lead to different stability ranges for the two planes. For the interesting region  $d \sim 116$  mm and  $a \sim 222$  mm the angles of incidence are as follows (see Fig. 4.3): at the mirror M1:  $\Theta_1 = 8.7^\circ$ , at the mirror M2:  $\Theta_2 = 3.5^\circ$ , at the mirror M3:  $\Theta_3 = 9.4^\circ$ . The stability ranges calculated for the two planes are shown in Fig. 4.5. The overlap of the two stability ranges is rather poor and some improvements are obviously necessary.

These two stability ranges can be, however, brought to overlap by means of a correcting Brewster-angle plate placed in a focused beam, i.e. either between M1 and M2 or between M1 and M3 [KID 72]. The plate changes the propagation properties and the waist development of the Gaussian beam in the following way. While the geometrical path  $l_{geom}^{glass}$  inside a Brewster plate of thickness  $t$  and refractive index  $n$  is

$$l_{geom}^{glass} = t\sqrt{n^2 + 1}/n, \quad (4.2)$$

the actual effective lengths  $l_{\perp}^{glass}$  and  $l_{\parallel}^{glass}$  relevant for the waist size and wavefront curvature development in the sagittal and the tangential planes are different [KID 72]:

$$l_{\perp}^{glass} = t\sqrt{n^2 + 1}/n^2 < l_{geom}^{glass}, \quad (4.3a)$$

$$l_{\parallel}^{glass} = t\sqrt{n^2 + 1}/n^4 < l_{\perp}^{glass} < l_{geom}^{glass}. \quad (4.3b)$$

These two different effective lengths  $l_{\perp}^{glass}$  and  $l_{\parallel}^{glass}$  have to be used in the calculation for the stability diagram for the part of the beam path inside the glass plate (outside the glass the common geometrical length is to be used). As an example, for  $n = 1.5$ :  $l_{\perp}^{glass} = 0.67 \cdot l_{geom}^{glass}$  and  $l_{\parallel}^{glass} = 0.30 \cdot l_{geom}^{glass}$ . Thus for a given geometrical configuration and a given Brewster plate thickness  $t$ , we obtain two stability diagrams for the  $\perp$  and  $\parallel$  planes. The changes are such that for a proper choice of  $t$  the two stability areas can be made to overlap locally; the correction can be made either in the  $a$ - or in the  $d$ -arm, combinations are also possible.

Around the recommended operating point O (see Fig. 4.5)  $d = 116$  mm,  $a = 222$  mm, the compensation can be achieved by means of a plate with thickness  $t_a \approx 27$  mm placed in the  $a$ -arm of the resonator, or a plate with thickness  $t_d \approx 11$  mm placed in the  $d$ -arm; the values apply to a material with  $n \approx 1.5$ , the dependence on  $n$  is weak.

It is, however, also possible to operate the laser with other mirror distances, i.e. in other areas of the whole stability range requiring different  $t$  values to obtain local

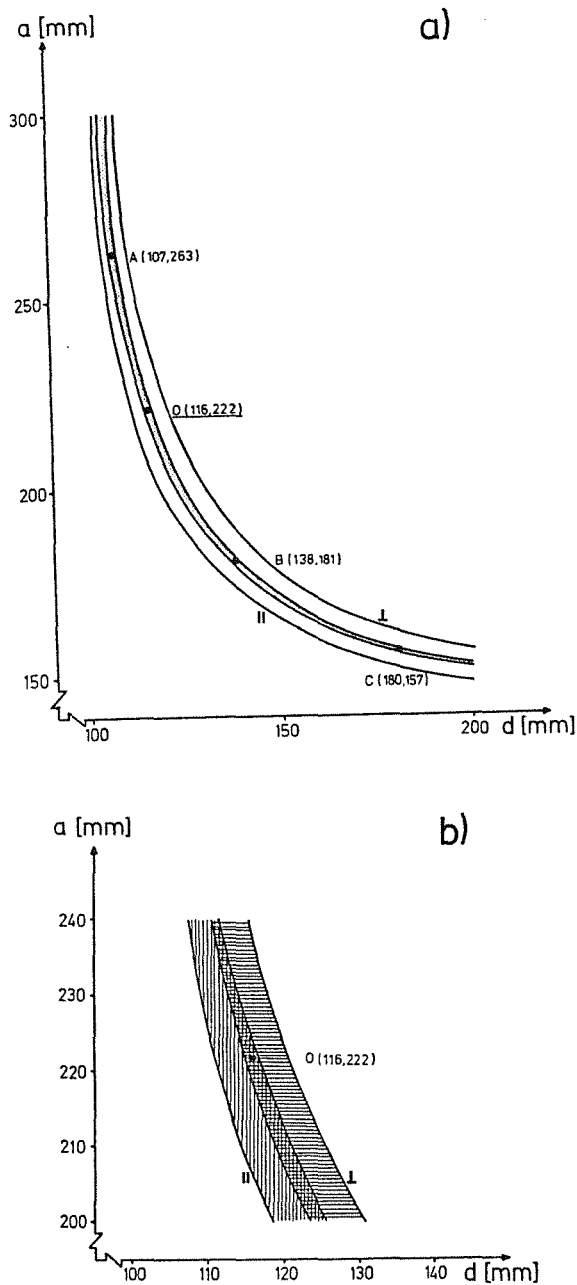


Fig. 4.5 Stability diagrams for the sagittal ( $\perp$ ) plane and tangential ( $\parallel$ ) plane; angles of incidence at the curved cavity mirrors as given in the text.

a) survey;

b) in the vicinity of the recommended cavity configuration.

overlap. For example, in point A (see Fig. 4.5) the thickness  $t_a \approx 38$  mm or  $t_d \approx 5$  mm is required, for point B:  $t_a \approx 16$  mm or  $t_d \approx 16$  mm, for point C:  $t_a \approx 12$  mm or  $t_d \approx 41$  mm.

The final solution to the problem (i.e. proper thickness  $t$ ) is, however, not that straightforward, since introduction of a Brewster plate in either of the considered

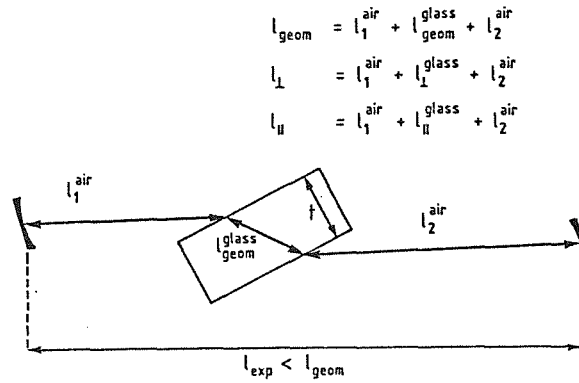


Fig. 4.6 Geometrical length and effective lengths for sagittal ( $\perp$ ) and tangential ( $\parallel$ ) planes upon insertion of a Brewster plate into one of the resonator's arm  $a$  or  $d$ ; for the respective other arm  $l_{\perp} = l_{\parallel} = l_{\text{geom}}$  as the whole path is in air.

resonator arms has a decrease of the angles of incidence as a consequence, which leads to an overcompensation. The proper plate thickness for astigmatism compensation therefore has to be found by iteration.

The final astigmatism compensation of the CR 699-21 resonator as used here is realized with the use of a Brewster-angle plate of the thickness  $t_o \approx 18.5$  mm placed in the  $a$ -arm; this is more convenient as there is relatively much space in comparison to the  $d$ -arm. The angles of incidence changed upon insertion of a plate of this thickness are (Fig. 4.3):  $\Theta_1 \approx 7.3^\circ$  (instead of  $8.7^\circ$ ),  $\Theta_2 \approx 3.5^\circ$  (unchanged),  $\Theta_3 \approx 8.0^\circ$  (instead of  $9.4^\circ$ ). The calculation of the stability ranges with these parameters is displayed in Fig. 4.7.

The compensation doesn't have to be perfect, it is sufficient if large parts of the sagittal and tangential stability ranges overlap in the vicinity of the resonator configuration used. In the present case the compensation is realized partially by the BBO crystal itself whose length is 5 mm ( $n = 1.67$ ) and the remaining part by an astigmatism compensating fused silica plate of thickness 12.7 mm = 1/2" ( $n = 1.46$ ), leading to an almost optimum compensation.

In practice the approximately correct mirror distances corresponding to the center of the resonator stability range can be found by determining the positions of the images of the fluorescence spot. In the middle of the stability range for the  $d$ - $a$  combinations in the vicinity of the recommended cavity configuration ( $d \approx 116$  mm,  $a \approx 222$  mm) the distance of the mirror M2 from the main waist in the jet ( $d_1$ , of

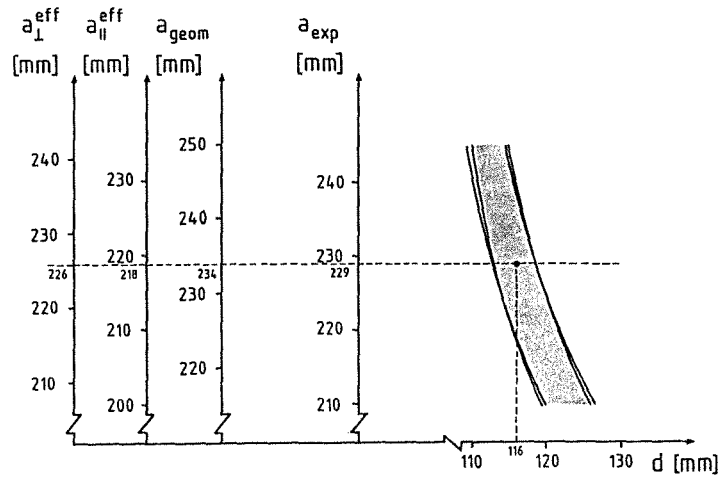


Fig. 4.7 Final stability ranges for sagittal ( $\perp$ ) and tangential ( $\parallel$ ) planes (angles of incidence at the cavity mirrors - see text) with astigmatism compensation as described in the text; good local overlap is achieved close to point O (see Fig. 4.5). The effective distances  $a$ , relevant for the stability, are different for the two planes:  $a_{\perp}^{eff} = 226$  mm,  $a_{\parallel}^{eff} = 218$  mm. The geometrical path is the same for both:  $a_{geom} = 234$  mm, the corresponding experimental mirror distance M1-M3 (see Fig. 4.6) amounts to  $a_{exp} = 229$  mm.

Fig. 4.3) is rather constant and amounts to 38.8 mm. Then the spot reflected from M2 (Fig. 4.3) has its focus at a distance  $\sim 113$  cm off M2 (if further reflected by the flat mirror M4 in the resonator, it is  $\sim 13$  cm in front of M3). The spot reflected from M1, if the mirror is set at a proper distance from the jet  $d_2 = 79.7$  mm, is focused at a distance of 134 mm. This distance doesn't change much all across the stability range in  $d$ -direction at a constant  $a$  (i.e. is not strongly dependent on  $d_2$ ), so it is not particularly suited for checking the correctness of the position of M1. It is, however, more important to keep the proper relation between the values of  $d$  and  $a$  than to maintain the distance of the mirror M1 from the jet. If this is the case, the spot reflected from M3 is focused at a distance  $\sim 117$  cm from this mirror (after further reflection by M4 in resonator the focus is  $\sim 9$  cm in front of M2). The above distances of the fluorescence spot images are almost constant in the vicinity of the recommended  $d$  and  $a$  values and almost independent on the distance at which the mirror M4 is placed (i.e.  $b$  value); thus the alignment is not very critical. The above procedure allows to set the mirrors at approximately the correct distances; in order to optimize the laser performance, usually additional fine adjustment is required.

## 4.2 Dyes

The fundamental wavelength  $\lambda = 511.6$  nm can be generated by means of Coumarin dyes. These are, however, usually not very efficient and most often have to be optically pumped by violet or ultraviolet light, preferably by a krypton ion laser. As no krypton pump source was directly available, an  $\text{Ar}^+$  laser had to be used. Two efficient Coumarin dyes have, however, been found both of which can be pumped with the blue lines of an  $\text{Ar}^+$  laser: Coumarin 510 and Coumarin 498. The latter proved to be the better of the two (a detailed comparison of their performance follows) and so this one was finally used.

Coumarin 510 is easily soluble in benzyl alcohol: to dissolve 1 g of the dye only 10 ml of this solvent is required. The solutions used in the laser contained 30% benzyl alcohol and 70% ethylene glycol. To dissolve 1 g of Coumarin 498 at least 300 ml of benzyl alcohol is needed. Therefore solutions consisting of 50% benzyl alcohol and 50% ethylene glycol were used.

Figs 4.8 and 4.9 show the absorption curves for Coumarin 510 and Coumarin 498, respectively; these were measured with a Perkin-Elmer Lambda 9 Spectrometer. A comparison is presented also in Table 4.1, where the values are scaled down to the thickness  $d = 0.14$  mm, which is the estimated thickness of the dye jet at the spot used.

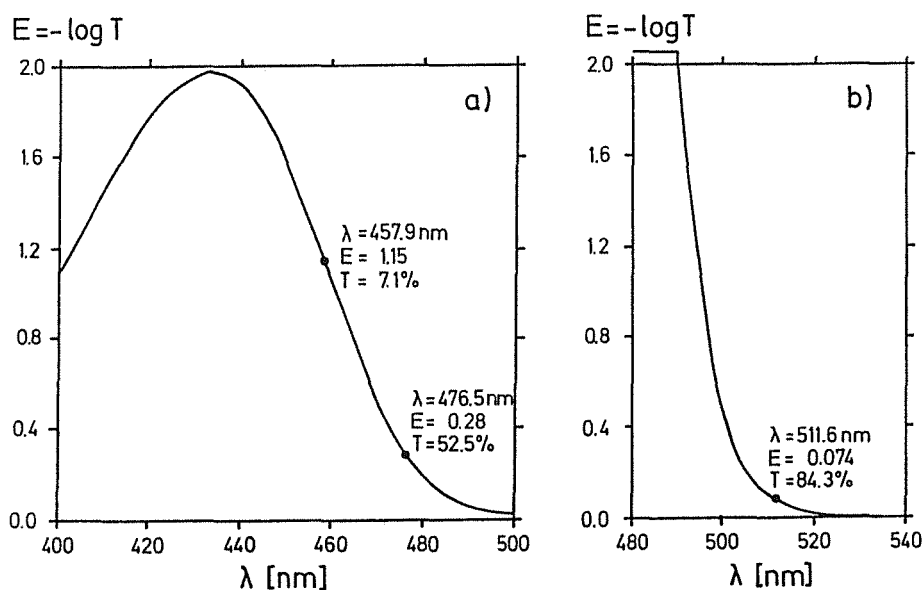


Fig. 4.8 Transmission  $T = 10^{-E}$  for Coumarin 510; dye concentration 0.80 g/l (optimized for best lasing efficiency at  $\lambda = 511.6$  nm in the ring laser); sample thickness: a) 0.2 mm, b) 10 mm; for important details concerning the purity of the solvents - see below.

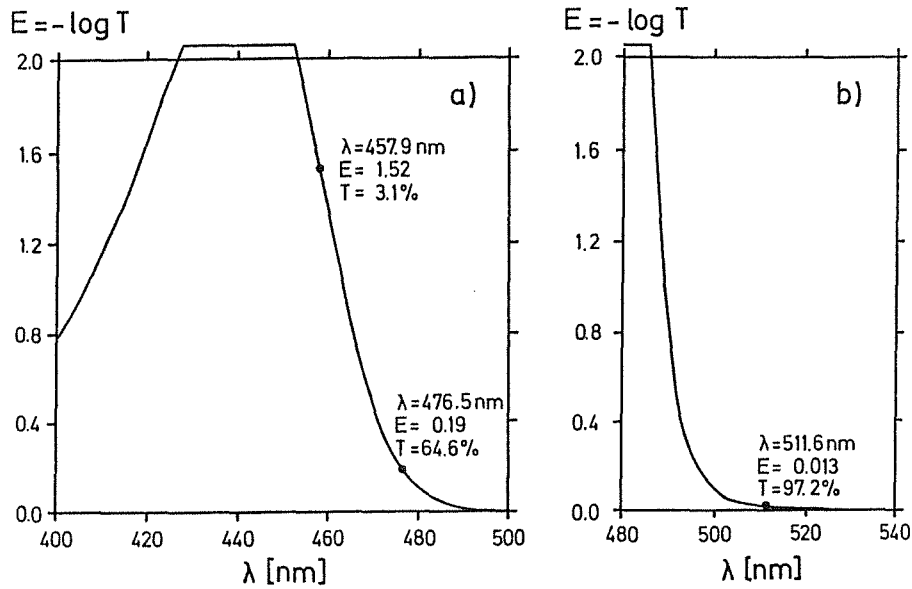


Fig. 4.9 Transmission T for Coumarin 498; dye concentration 1.00 g/l (optimized for best lasing efficiency at  $\lambda=511.6$  nm in the ring laser); sample thickness: a) 0.2 mm, b) 10 mm.

Table 4.1 Dye jet absorption of Coumarin 510 and Coumarin 498 for concentrations of 0.8 and 1 g/l, respectively; values scaled from other thicknesses (see Figs 4.8 and 4.9) to the thickness  $d=0.14$  mm, being the dye jet thickness used. Respective concentrations are those for best lasing efficiency at  $\lambda=511.6$  nm in the CR 699.

$\lambda$ [nm]	absorption in % for $d=0.14$ mm	
	Coumarin 510 (conc. 0.8 g/l)	Coumarin 498 (conc. 1.0 g/l)
457.9	84.3	91.4
476.5	36.3	26.4
511.6	0.24	0.04

For optical pumping initially two pump wavelengths were considered:  $\lambda=457.9$  nm and  $\lambda=476.5$  nm; the pump power available at the latter is typically almost twice as high as at the former. The pump wavelength  $\lambda=457.9$  nm, however, was found more favorable than  $\lambda=476.5$  nm despite its lower power, since the latter requires rather high dye concentrations, which is clear from Table 4.1: in the case of Coumarin 510 the concentration required for 85 - 90% absorption of  $\lambda=476.5$  nm

were 3.5 - 4.1 g/l (the corresponding reabsorption at the operating wavelength  $\lambda = 511.6$  nm being then 1.0 - 1.2%), in the case of Coumarin 498 the corresponding concentration were 6.2 - 7.5 g/l (and the reabsorption at  $\lambda = 511.6$  nm: 0.25 - 0.30%).

For Coumarin 510 it has been found that the concentration of  $\sim 1.6$  g/l optimized for  $\lambda = 476.5$  nm pumping was the result of a compromise between the absorption of the pump wavelength (which should be high) and the reabsorption of the generated wavelength  $\lambda = 511.6$  nm (which should be as low as possible). Thus the resulting absorbed pump power at  $\lambda = 476.5$  nm (1.86 W;  $\sim 60\%$  of 3.1 W) was somewhat higher than at  $\lambda = 457.9$  nm (1.45 W;  $\sim 85\%$  of 1.7 W), but no remarkable increase of the laser power generated at  $\lambda = 511.6$  nm was observed.

For Coumarin 498 the reabsorption at  $\lambda = 511.6$  nm was not expected to cause problems even at the required concentration of 7 g/l; such high concentrations, however, could not be realized because of the poor solubility of this dye. Therefore the pump wavelength  $\lambda = 476.5$  nm was not tried. Under these circumstances the pump wavelength  $\lambda = 476.5$  nm was definitely abandoned for Coumarin 498.

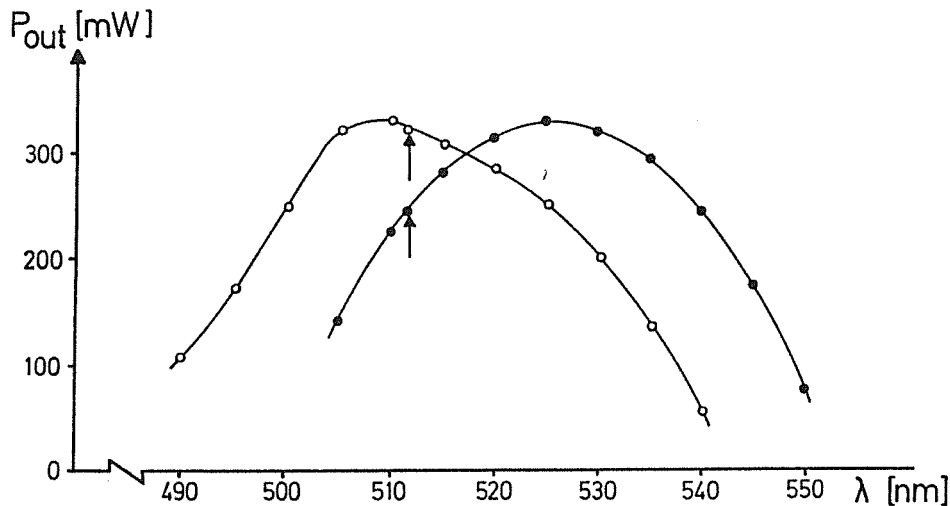


Fig. 4.10 Tuning curves for Coumarin 510 (●) and Coumarin 498 (◯), obtained with a standard output coupling mirror G 3862-003 (Spectra Physics); pump wavelength  $\lambda = 457.9$  nm, absorbed pump powers: 1.35 W for Coumarin 510, 1.4 W for Coumarin 498; dye concentrations optimized for an operating wavelength of  $\lambda = 511.6$  nm in a Spectra Physics model 375 linear laser : 0.73 g/l for Coumarin 510, 0.64 g/l for Coumarin 498 (obviously different spots on the jet were used, which happened to have different thicknesses). The arrows indicate our operating wavelength  $\lambda = 511.6$  nm.

Both dyes have been examined under laser operating conditions in a linear laser (Spectra Physics, model 375) with a one-element Lyot filter for wavelength selection (broad-band operation). In this way tuning curves were obtained and peak efficiencies were measured (Fig. 4.10); the absorbed pump powers were slightly different in both cases (1.35 W for Coumarin 510 and 1.4 W for Coumarin 498).

Measured peak efficiencies are for both dyes approximately the same, namely  $\sim 24\%$ ; the important difference is that of the position of  $\lambda = 511.6$  nm with respect to the peaking wavelength. For Coumarin 510 the peaking wavelength lies around 525 nm and at  $\lambda = 511.6$  nm one can obtain only  $\sim 70\%$  of the maximum power, while for Coumarin 498 the peaking wavelength is  $\sim 508$  nm and the power obtainable at  $\lambda = 511.6$  nm is  $\sim 95\%$  of the maximum value.

Coumarin dyes tend to degrade when in use. For both Coumarin 510 and Coumarin 498 a considerable decrease of the lasing efficiency was observed after a few weeks of operation, resulting partially from the increase of the reabsorption at the operating wavelength  $\lambda = 511.6$  nm (Fig. 4.11). The reabsorption alone, however, does not fully account for the observed decrease of the efficiency, so it must be assumed that some additional degradation takes place. A visible sign of the degradation was the change of the color of the solution from yellow-green to brownish. The possible rea-

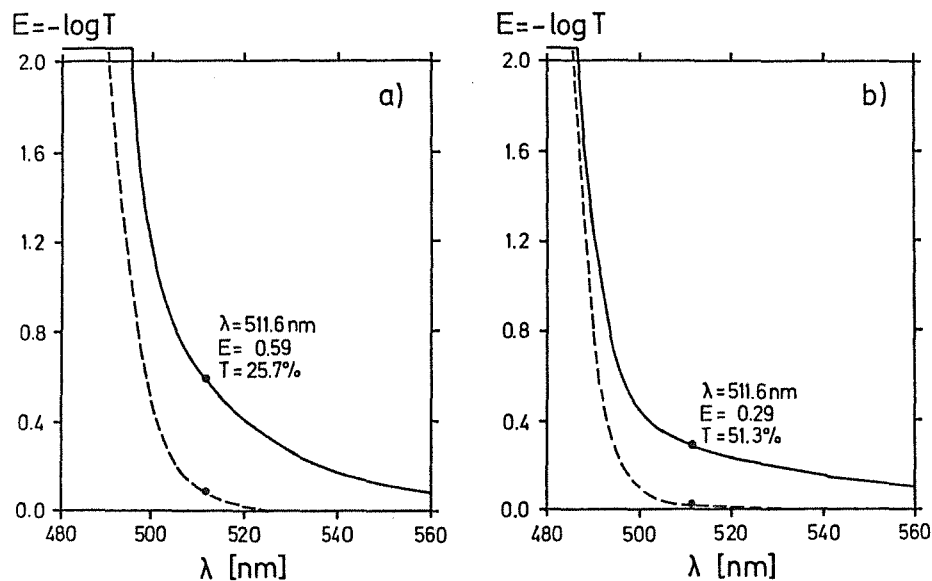


Fig. 4.11 Transmission curves for degraded dye solutions: a) Coumarin 510, b) Coumarin 498 (the corresponding transmission curves for fresh solutions are dotted - see Figs. 4.8b and 4.9b). Sample thickness was 10 mm. For a jet of thickness 0.14 mm transmissions of a)  $T = 98.1\%$  and b)  $T = 99.1\%$  result.

son of the degradation is some sort of chemical decomposition which might be caused or catalyzed by: a) irradiation, b) air, c) materials used in the dye circulator unit (teflon and stainless steel, regarded as chemically inert, though). The irradiance lifetime of the dye solutions has not been examined in more detail; a rough estimate is  $\sim 100$  W·h.

Another phenomenon, observed for Coumarin 510, was a particularly strong dependence of the absorption in the lasing range on the purity of the used solvents (solvatochromism). A considerable difference in the reabsorption was observed between the solutions containing ethylene glycol of different qualities. An increase of the amount of impurities (most likely water) caused a 5-fold decrease of the absorption in the wing of the absorption curve (see Fig. 4.12), without changing anything in the absorption at the pump wavelengths. No visible sign of degradation (i.e. no considerable change of the color of the solutions) is then observed. A comparison of the absorption in the lasing wavelength range for a solution with reduced water content (ethylene glycol of extra pure quality, Merck No 949) and the same solution after adding a drop of water is presented in Fig. 4.12. Thus low purity quality is recommended; too high purity solvent might be conditioned by adding a small amount of water. About 0.5% of water content seems to be sufficient, whereas 0.1% might be too low. No such effect has been observed for Coumarin 498.

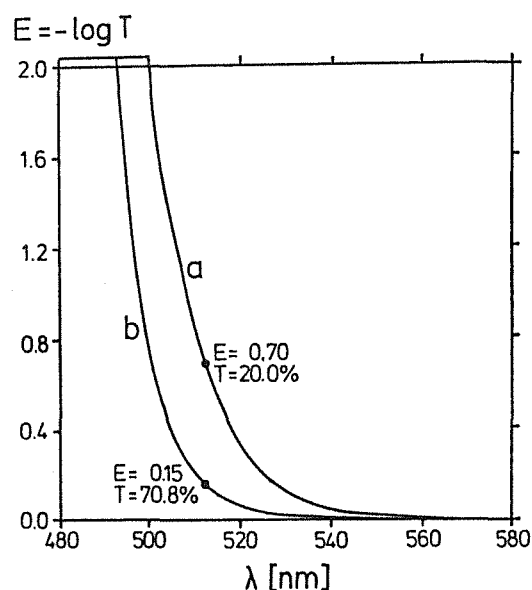


Fig. 4.12 Transmission curves for Coumarin 510; sample thickness 10 mm.  
a) a solution made of ethylene glycol of extra pure quality,  
b) the same solution after adding a drop of water which improves the transmission.

### 4.3 Pump waist

An Ar<sup>+</sup> laser (Coherent model Supergraphite 3000K with an Innova 100-20 discharge tube, 20 W nominal power) is used for optical pumping of the ring dye laser. For Coumarin dyes (both Coumarin 510 and Coumarin 498, see Section 4.2) blue pump lines must be used: either  $\lambda = 476.5$  nm - the pump power available with a new Ar<sup>+</sup> tube (output coupler for the blue option: Part No. 0160-003-00): 3.6 W doughnut mode or 2.5 W TEM<sub>00</sub>, or  $\lambda = 457.9$  nm - pump power: 2.2 W doughnut mode or 1.3 W TEM<sub>00</sub>. The latter pump wavelength has been found to be more favorable (see Section 4.2) and henceforth is used exclusively.

The pump laser cavity has a flat back mirror and an output coupler with 15 m radius of curvature at a distance of 1.8 m. The pump beam incident on the dye laser's pump mirror therefore has a size parameter  $w = 0.9$  mm. It is focused onto the dye jet by a pump mirror with a radius of curvature  $R_p = 100$  mm. Thus the pump waist size is  $w^p_0 \approx 8$   $\mu\text{m}$  which is smaller than the dye laser waist in the jet ( $w^d_0 = 14.7$   $\mu\text{m}$ , see Section 4.1), so the entire pump waist cross-section is used.

It has been found that the transverse mode structure of the pump beam has no noticeable influence on the dye laser performance, therefore for the sake of high power the stronger doughnut-mode pump beam has been used throughout.

### 4.4 Single-mode selection, frequency stabilization and scanning

To obtain high fundamental power, which is necessary for frequency doubling, a new frequency selection scheme has been applied. Both frequency stabilization and scanning are performed by means of the standard CR 699-21 scanning and control electronics with some modifications.

#### a) Single-mode selection

The standard ICA ("intra-cavity assembly"), normally used for single-mode selection in the CR 699-21, in our case was found to cause an internal power drop to about 30 - 40% of its value in the broad-band operation. Because of our high power requirement this lossy unit couldn't be used and had to be replaced by some other frequency selective elements. An alternative frequency selection scheme [Kr 80] consists in using mode competition and low-loss uncoated etalons.

In the broad-band operation a considerable number of resonator modes can be lasing; because of mode competition, only one of them can lase in the ring cavity at a time, but any slight change of the intracavity conditions can give the preference to another one giving rise to mode hops. This occurs frequently and at random. The ICA assures single-mode operation by suppressing all the resonator modes except

the selected one - the loss introduced for the two neighboring modes is almost 1%. However, much lower loss than that is actually required to achieve relatively stable single-mode operation [Kr 80]. It has to be stressed, however, that the dye jet stability and in particular the absence of air bubbles are very important to avoid too frequent mode hops. The dispersion of uncoated etalons is not sufficient to suppress all the modes but a selected one, normally several of them can still lase in turn. All turbulences in the dye flow as well as passing of an air bubble through the active zone result in momentary power drops which restart the mode competition mechanism and thus can cause mode hops. It has been found that a standard Coherent nozzle assures a sufficiently laminar dye flow [Kn 87, DKM 89].

In the present single-mode selection scheme two uncoated etalons have been used: one with an FSR=50 GHz (thickness  $t=2$  mm) and the other one with an FSR=200 GHz (thickness  $t=0.5$  mm). The rough frequency selection is performed as usual, i.e. by a three-element Lyot filter. The 50 GHz etalon is mounted on a galvo-scanner (for further details see below) and tilted manually to the angle required for the chosen frequency. The 200 GHz etalon is tilted manually to match its maximum transmission with that of the 50 GHz one. The transmission of all the three dispersive elements used is presented in Fig. 4.13.

By means of induced interruptions of the internal laser beam [Kn 87, DKM 89] the statistics of the mode hopping behavior was studied; the occurring frequencies were

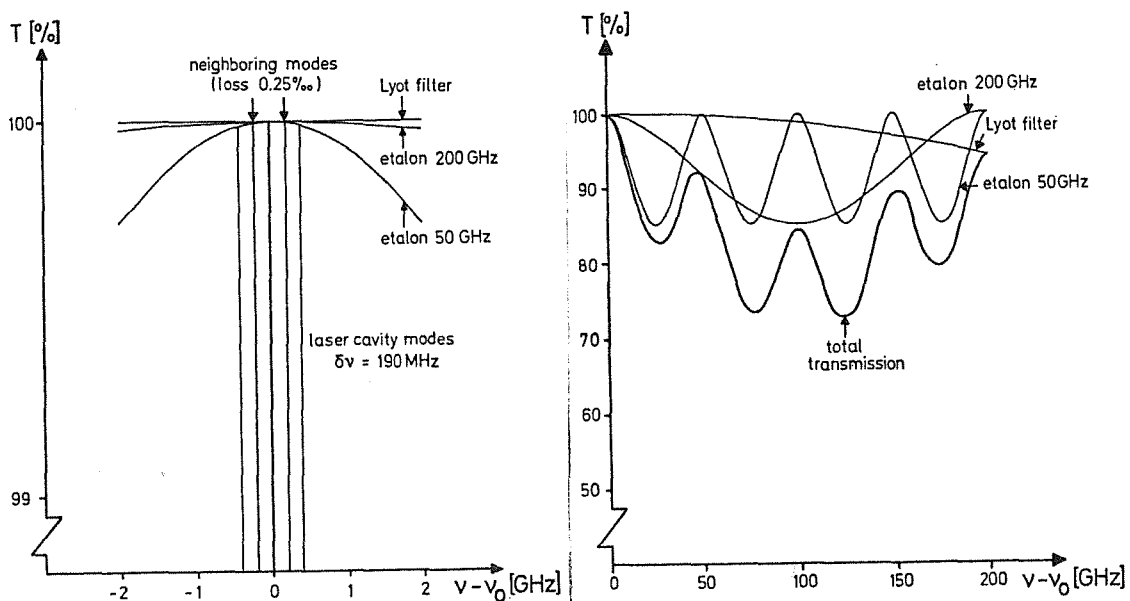


Fig. 4.13 Transmission of the dispersive elements in the new single-mode selection scheme, including a three-element Lyot filter and two uncoated etalons.

checked by a wavemeter (see Section 4.8). With the 50 GHz etalon alone, normally only 4 - 5 neighboring resonator modes were found to occur; however slight misalignment of the laser (resulting for instance from the thermal drift of the Lyot filter mount) resulted also in mode hops of 50 GHz (i.e. one FSR of the etalon). Insertion of the 200 GHz etalon was sufficient to suppress these 50 GHz mode hops and to confine the laser frequencies to a few neighboring cavity modes.

b) Frequency stabilization

The laser frequency in the CR 699-21 system is stabilized on the slope of the transmission peak of a reference cavity (Fig. 4.14) with an FSR = 1 GHz (LOCK mode of operation). This is done by changing the laser resonator optical length by means of feedback signals fed to two intracavity elements:

- tuning plates (DC and slow corrections of the frequency drift),
- piezo-driven resonator mirror (AC correction of "fast" frequency excursions).

The two tuning plates of thickness  $t=2$  mm are mounted in the long upper arm of the laser (Fig. 4.1). They are rotated by two galvo-scanners (type G108 by General Scanning, actual sensitivity for both: 145 mA/degree, if applied to the coils connected in series). The two scanners are connected in series to assure the same current flow through both and thus the same tilt angle for both plates. With no current flowing the plates are set to Brewster's angle. For frequency corrections or scanning they are tilted in opposite directions thus maintaining the laser alignment during scans. The angular sensitivity required for our spectral range ( $\sim 510$  nm) is  $0.1^\circ/\text{GHz}$  or (15 mA/GHz).

A new piezo-driven mirror, with a larger diameter than the standard one (10 mm instead of 3 mm), has been constructed; technical details concerning the piezo-transducer are described in [DKM 89]. Its sensitivity amounts to  $6 \mu\text{m}/\text{kV}$ , which corresponds to  $4 \text{ GHz}/\text{kV}$  in terms of laser frequency changes. As the voltage supplied by the PZT driving circuit is limited to  $+250 \text{ V} \pm 200 \text{ V}$ , the resulting correction range amounts to  $\pm 0.8 \text{ GHz}$ . The new piezo-driver requires the opposite polarity of the feedback voltage as compared to the standard unit used in the CR 699-21 model, therefore an inverter in the PZT driving circuit board 1A1 was added.

The majority of the occurring mode hops is to neighboring modes, so in the LOCK mode of operation they cannot be seen usually as their frequency remains within the catching range of the selected transmission slope of the reference cavity and is automatically pulled back to the original frequency. Since mode hops as far as 4 mode spacings (i.e.  $\pm 750 \text{ MHz}$ ) occasionally can occur as well (see text above), the resulting frequency can sometimes fall within the catching range of a neighboring

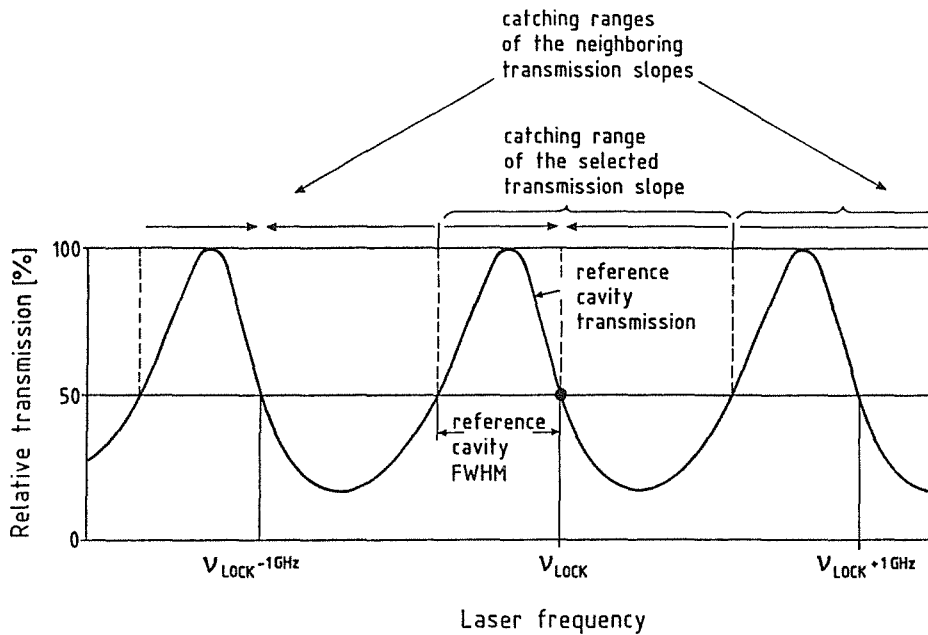


Fig. 4.14 Stabilization of the laser frequency to the slope of the reference cavity transmission peak.

transmission peak of the reference cavity. Then a frequency jump of  $\pm 1$  GHz (i.e. one FSR of the reference cavity) is observed. Therefore during measurements the laser frequency has to be under permanent wavemeter control, and if a 1 GHz frequency jump should occur, the frequency must be returned to its due value. This is achieved by interrupting the internal laser beam and testing the resulting frequency. The procedure is repeated under computer control until the resulting lasing resonator mode is again within the catching range of the selected reference cavity slope and the laser locks to it.

c) Frequency scanning

Frequency scanning is realized by stabilization to a variable frequency reference. For this purpose as usually the reference cavity's frequency is scanned over the required frequency range by tilting a tuning plate inside it; the plate is mounted on a galvo-scanner type G302 (actual sensitivity  $\sim 480$  mA/degree) and its initial tilt angle is close to Brewster's angle. The plate thickness amounts to 0.5 mm; for a  $\pm 15$  GHz scan a tilt angle  $\pm 0.5^\circ$  is required. The tuning plates' and the etalons' galvo-scanners are supplied with adequate feed-forward driving currents.

The tilt angle of the tuning plates required for a  $\pm 15$  GHz scan range at  $\lambda \approx 510$  nm is  $\pm 1.5^\circ$  off Brewster's angle. The total reflection loss (4 surfaces) introduced in this way amounts to 0.1% at most, which results in a power drop of less than 5%.

The 50 GHz etalon is driven by a special driving circuit ("thin etalon" circuit 1A5 in the 699-21 electronics), i.e. tilted in such a way that the tilt angle follows a square root function; as a reference the orthogonal position (so-called "flash") is used. Using this driving circuit requires a galvo sensitivity of  $\sim 440$  mA/degree, as in the original system. To obtain the same sensitivity for the G108 scanner used (actual sensitivity 137 mA/degree with its two coils connected in series), its coils have been connected in parallel instead; a further  $3.7 \Omega$  resistor was added in parallel to the coils resulting in the required angular sensitivity.

The 200 GHz etalon - after manual centering - is driven so as to keep the match of its maximum transmission with that of the 50 GHz one during scans; it is also mounted on a G108 scanner. To assure time synchronism this scanner has to be supplied with a feed-forward current from the same internal scan generator as the rest of the elements. It has been connected in series with the reference cavity galvo scanner; the driving current through its coils can be adjusted by setting a  $20 \Omega$  potentiometer connected in parallel. Thus the 200 GHz etalon is tilted linearly; this is sufficient for scans up to 30 GHz if the initial tilt angle is about  $1^\circ$  (corresponding to 20% of the FSR) or larger - since then the deviations from the adequate square root function are small enough. The value  $\Delta I/\Delta v$  has to be, however, adjusted for a selected initial tilt angle to optimize the performance. It has to be noted that even when the tilt angle of the 200 GHz etalon is not changed while scanning, frequency scans up to 30 GHz can still be performed, however a power drop by 40 - 50% at the lower and the upper limit of the scan occurs; with the linearized feed-forward the corresponding power drop is reduced to only 5 - 10%.

For the measurements the "external" option for frequency tuning is used to assure synchronism with the data acquisition process. The frequency is scanned stepwise under the supervision of a computer by supplying the control unit with appropriate DC voltages via a DAC. The actual frequencies are measured and checked in parallel by a fast reading wavemeter [St 84, Sc 90].

#### 4.5 Intracavity losses

In order to determine the dependence of the intracavity power of the CR 699-21 resonator on the internal losses, a variable output coupling scheme was used. It is based on a thin plane-parallel plate inside the resonator; coupling variations were realized by rotating the plate off Brewster's angle by a known angle. The curves representing the internal and external powers as a function of the coupling for Coumarin 498 are plotted in Fig. 4.15. The optimum coupling has been found to be  $\sim 2.7\%$  with the output power amounting to  $\sim 23\%$  of the absorbed power; this value is consistent with the results presented in Fig. 4.10.

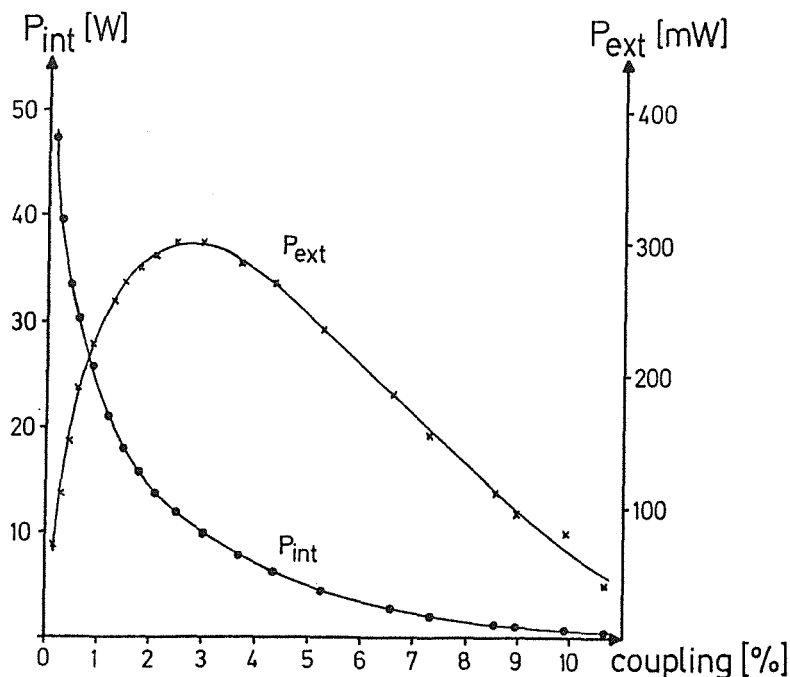


Fig. 4.15 Internal and external power as a function of the coupling at  $\lambda = 511.6$  nm for Coumarin 498 in the modified CR 699-21 ring laser. The pump wavelength was  $\lambda = 457.9$  nm. The dye concentration was optimized for  $\lambda = 511.6$  nm (1.0 g/l). The resulting absorbed pump power was 1.35 W.

As all intracavity elements have been inserted one after the other, their insertion losses were roughly estimated to be:

- Lyot filter: 0.4 - 0.5%,
- Brewster tuning plates: less than 0.1%,
- etalon 50 GHz (in flash): less than 0.1%,
- etalon 200 GHz (in flash): less than 0.1%.

The loss introduced by the dichroic mirror is  $\sim 0.35\%$  (Fig. 4.2). Thus the total intracavity loss without the crystal amounts to  $\sim 1\%$ .

On the other hand, the insertion loss of the ICA has been found to amount to  $\sim 2.5\%$  (power drop with the ICA: see Section 4.4), which is rather high. Assuming the lowest loss of the crystal, amounting to 0.5% (see Section 4.6), the total intracavity loss with the ICA were  $\sim 3.5\%$ , compared to the total loss of  $\sim 1.5\%$  with the new frequency selection system described in Section 4.4. The corresponding intracavity powers are 8 W and 18 W, respectively; this means about a factor of 5 gain in the obtainable UV power by removing the ICA from the laser.

#### 4.6 Intracavity frequency doubling in a BBO crystal

##### a) Theoretical considerations

In the present work the frequency doubling of  $\lambda = 511.6$  nm is performed inside the Coherent CR 699-21 resonator in the auxiliary waist by means of a 5 mm long BBO crystal.

BBO is a uniaxial optically negative crystal of crystallographic space group R3c [EDV 87]. Its refractive indices at wavelengths  $\lambda = 511.6$  nm (fundamental ordinary beam) and  $\lambda = 255.8$  nm (second harmonic extraordinary beam) required for calculating the phase-matching angle can be obtained with the use of the Sellmeier equations given in [Ka 86]. These indices are as follows:

$$n_o(\lambda = 511.6 \text{ nm}) = 1.676 ,$$

$$n_o(\lambda = 255.8 \text{ nm}) = 1.770 ,$$

$$n_e(\lambda = 255.8 \text{ nm}) = 1.620 ,$$

which on substitution into the formula (A.1, Appendix) give the value of the phase-matching angle with respect to the optic axis (crystallographic  $c$ -axis)

$$\Theta_m = 50.5^\circ .$$

The effective nonlinear optical constant for type I ( $oo \rightarrow e$ ) phase matching in R3c crystals is given by the approximate formula [CWJ 85]:

$$d_{eff} = d_{11} \cos 3\Phi \cos \Theta + d_{13} \sin \Theta , \quad (4.4)$$

where  $\Phi$  is the angle with respect to the crystallographic  $a$ -axis (for type I phase matching  $\Theta_m$  lies in the  $ac$ -plane, i.e.  $\Phi = 0$ ). The nonlinear optical constants  $d_{11}$  and  $d_{13}$ , as given in [CWJ 85], are as follows:

$$d_{11} = (1.94 \pm 0.22) \cdot 10^{-12} \text{ m/V} ,$$

$$d_{13} = (1.36 \pm 0.83) \cdot 10^{-13} \text{ m/V} ,$$

which give

$$d_{eff} = 1.34 \cdot 10^{-12} \text{ m/V}$$

for the present case. This is a large value compared to other nonlinear crystals that can be used for SHG in the spectral range  $\sim 255$  nm (urea [HBD 78], lithium formate monohydrate LFM [DTS 73], potassium pentaborate KB5 [DCH 75, De 76]).

The second harmonic power is expressed by formula (A.3, Appendix). In order to estimate the UV power attainable in this particular case further factors have to be considered which enter into (A.3). Of these first of all are of interest the focusing parameter  $\xi$  and the double refraction parameter  $B$  (formulas (A.5) and (A.7), respectively). The parameters given are the crystal length:  $l = 5$  mm and an

auxiliary waist size in the CR 699-21 resonator:  $w_0 = 27 \mu\text{m}$  (see Section 4.1) which lead to:

$$\xi = 0.20 ,$$

being a so-called weak focusing case (thus the use of the weak focusing approximation is justified). BBO is a highly birefringent crystal - its walk-off angle (formula (Appendix 2)) in the case considered amounts to

$$\rho = 4.86^\circ = 0.0848 \text{ rad}$$

which gives a double refraction parameter value of

$$B = 15.5 .$$

From Fig. A.1 it can be seen, that for optimum focusing (i.e.  $\xi = 1.39$ )  $h_m(B = 15.5)$  were 0.06. The actual deviation from optimum focusing causes a decrease of the efficiency. In order to optimize the focusing conditions, either the auxiliary waist had to be reduced to a size of  $\sim 10 \mu\text{m}$  (and this would require a completely different resonator) or a crystal with a length of  $\sim 30 \text{ mm}$  had to be used.

Finally the function  $h$  in (A.3) takes the value  $h \approx 0.025$  giving a theoretical conversion coefficient of

$$C \approx 35 \mu\text{W}/\text{W}^2 ,$$

which applies to the SH power generated inside the crystal. (Under optimum focusing conditions, i.e. for e.g. a waist size of  $w_0 \approx 10 \mu\text{m}$ , the corresponding value were  $C \approx 90 \mu\text{W}/\text{W}^2$ ). For an internal power of 10 - 30 W (see Section 4.5) a generated UV power of 3.5 - 31.5 mW is expected which appears sufficient for the experiments. Therefore no further attempts to optimize the focusing conditions were made.

Another important property of the generated UV is the beam shape on leaving the crystal, as it determines the beam propagation properties. The so-called aspect ratio  $A$  (formula (A.10)), being the ratio of the UV beam waist sizes in the horizontal and vertical directions, amounts to

$$A = 11.1 ,$$

which means that the UV beam on leaving the crystal is considerably elongated in the horizontal direction. As the divergence of the UV beam is thus different in the horizontal and the vertical directions, cylindrical optics is required for the beam collimation.

In order to estimate the stability of the considered frequency doubling process against temperature changes, angle misalignment and frequency changes, corresponding FWHM power bandwidths  $\Delta T$ ,  $\Delta \Theta$  and  $\Delta \nu$  (see Appendix) were de-

terminated. Calculations based on a simple plane wave approximation as used in [EDV 87] and with the data from [EDV 87] give:

$$\Delta\Theta = 0.32 \text{ mrad} = 1.1' ,$$

$$\Delta T \approx 6^\circ\text{C} ;$$

the angular dispersion in the vicinity of  $\lambda = 511.6 \text{ nm}$  amounts to  $1.31 \cdot 10^{-4} \text{ deg/GHz}$  [GWU 87], which leads to a fundamental laser frequency FWHM of

$$\Delta\nu \approx 140 \text{ GHz} .$$

These theoretically expected values are compared to the actually measured ones, see below in this section (4.6d).

#### b) Practical use

The essential feature in any frequency doubling process is the doubling efficiency of the crystal. In intracavity frequency doubling, however, the low losses for the fundamental wavelength are still more important, as these determine the fundamental power obtainable. Therefore crystals for intracavity use are preferably Brewster cut, and so were all the four BBO crystals used in this work.

All the four crystals were found to have very similar frequency doubling efficiencies, as measured in an external  $\text{Ar}^+$  laser beam with  $\lambda = 514.5 \text{ nm}$ . The beam was focused by a lens with a focal length of 60 mm, so the waist size was  $10 \mu\text{m}$ . For all the crystal lengths used (between 5 mm and 7 mm) this waist size was very close to the optimum value ( $10.0 \mu\text{m}$  and  $11.8 \mu\text{m}$ , respectively). The values found were in agreement with the values expected in the optimum focusing case, and rather constant through the whole crystal volume.

In contrast to the doubling efficiency, BBO crystals are of wide spread quality as far as their insertion losses are concerned, and this is normally the feature which determines their usefulness for intracavity use. In this work only two of the four crystals have been successfully used for intracavity generation of UV light. For the better of them a single pass total loss amounted to 0.5%, as measured in a linear laser resonator by determining the reflection loss of a plane-parallel quartz glass plate rotated off the Brewster's angle until the same power drop was obtained as with the crystal inserted. This loss caused the internal power of the ring laser to drop to  $\sim 70\%$  of the original value, obtained with a "dummy" (a piece of quartz glass plane-parallel plate of similar thickness). Initially this value proved to be approximately constant through a large part of the crystal volume; this changed later on, see below in this section. For the other of the two useful crystals the single path total loss was 1.3% and the corresponding internal power drop to  $\sim 50\%$ . Because this crystal degraded after several weeks (possibly by mishandling), it could not be used

any more until it was repolished. The two poor crystals at best showed single path total losses of 2.5 - 2.6% which caused the internal power drop to  $\sim 20\%$  with a corresponding square UV power drop.

c) Mounting

To minimize losses, the crystal was inserted into the resonator at Brewster's angle. The crystal's orientation has to meet three conditions simultaneously (Figs 4.16 and 4.17) :

- 1) The primary light field inside the crystal must be an o-beam, i. e. the electric vector has to be perpendicular to the crystal's optic axis. Since the laser is polarized in the ring plane, this condition is met by rotating the crystal's clamp manually inside its holder (see Fig. 4.17) until the reflection off its entrance face (mainly spurious s-light) lies in the ring plane. This procedure assumes that the crystal is properly cut. The rotation angle, however, is not very critical, since small deviations from perfect o-polarization reduce the doubling efficiency only slightly. This adjustment is performed first.
- 2) The crystal thereafter is tilted to align Brewster's angle properly. For this purpose the crystal is rotated around the horizontal axis of a gimbal mount until the p-component of the reflected light is minimized. This angular align-

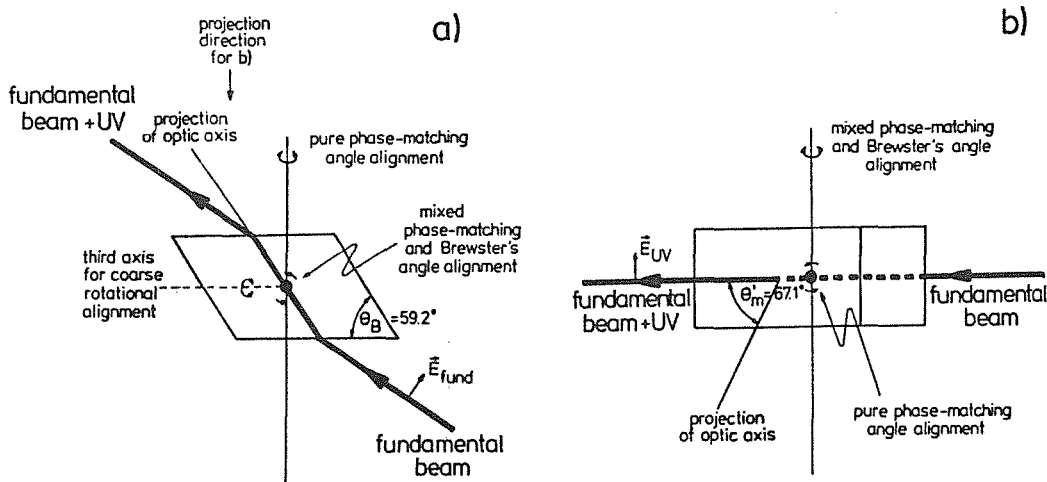


Fig. 4.16 Rotational alignments of the crystal; a) side view (projection onto the laser ring plane), b) plan view. The electric vector of the incoming fundamental wave is in the laser ring plane, the outgoing UV light is polarized perpendicularly to it. The crystal optic axis is in a plane containing the internal beam and perpendicular to the  $\vec{E}$  vector, i. e. in a plane perpendicular to the ring plane.  $\Theta_m = 50.5^\circ$ ;  $\Theta_B = 59.2^\circ$ ;  $\Theta'_m = 67.1^\circ$  is a projection of  $\Theta_m$  onto the plane parallel to the crystal's faces.

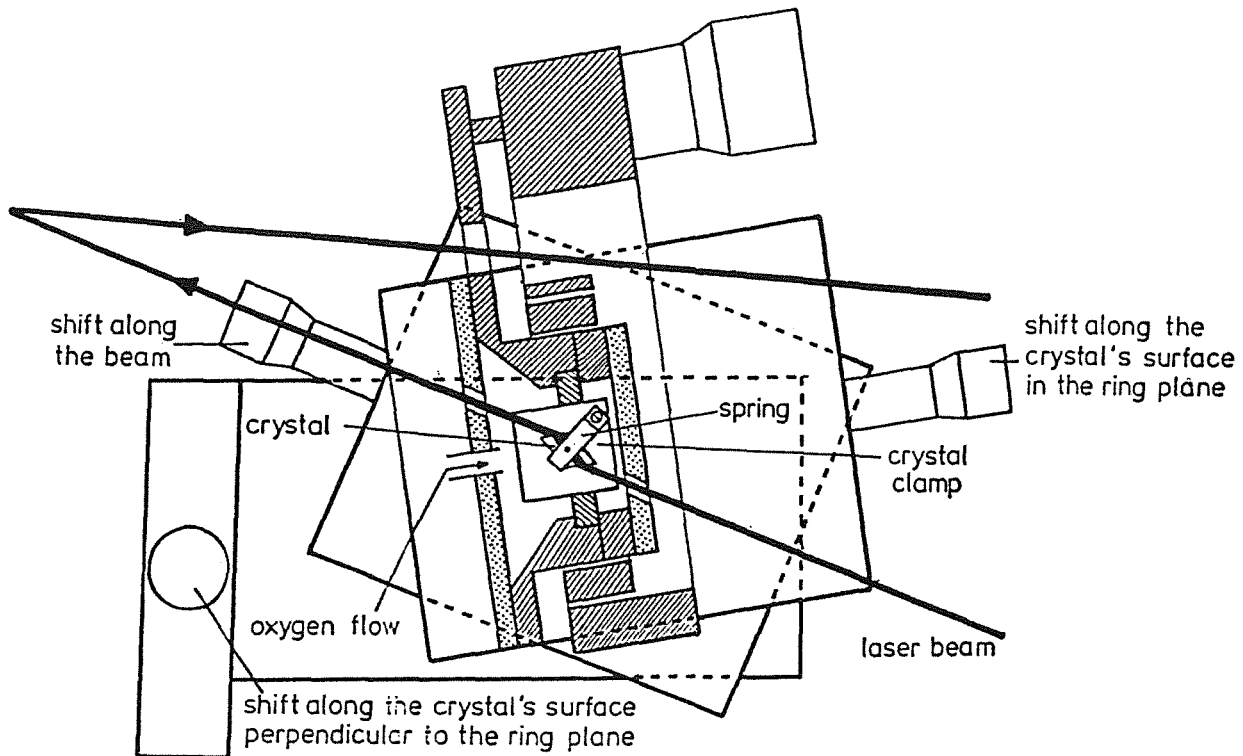


Fig. 4.17 Crystal holder

ment again is not very critical, since the reflection losses for small deviations from Brewster's angle are negligible; as an example, for  $\pm 1^\circ$  it amounts to only 0.01 %.

- 3) Finally the crystal is rotated around the other axis of the gimbal mount to align the phase matching angle. If this axis is perpendicular to the crystal's polished faces, this rotation maintains the angle of incidence. For the tolerance for this phase matching angle, see Section 4.6d.

Alignments 2) and 3) have to be iterated since 3) is not perfectly decoupled from 2) unless the crystal is perfectly mounted inside its clamp. Rotation 2), however, has a strong influence on the phase matching angle, whereas 3) interferes with 2) only slightly.

The crystal holder has in addition three translational degrees of freedom: two within the plane of the crystal's faces to choose a low-loss beam path inside the crystal and the third one along the laser beam inside the crystal to optimize the waist position inside the crystal such that maximum second harmonic power is obtained.

To keep the dust off the crystal's surfaces it is purged with a dry gas (flow 0.5 l/min) when in use; following rumors that the crystal degrades unless it is purged with

oxygen, we use this gas. The necessity of using oxygen has, however, not been proved and there are contradictory opinions concerning this question; it is also said that under the operating conditions like ours nitrogen or air can be used as well. Also a housing hermetically closed with Brewster's windows was found to perform satisfactorily [Bo 88] over extended periods.

d) UV output

The generated UV light is s-polarized and therefore it is partially reflected from the crystal's exit surface; the reflection loss for  $n_e(\lambda = 255.8 \text{ nm}) = 1.62$  amounts to  $\sim 20\%$ . Further losses are caused by the UV dichroic output coupler (15 - 20%, see Fig. 4.2) and the beam transport optics ( $\sim 15\%$ , see Section 4.7). The maximum UV power at  $\lambda = 255.8 \text{ nm}$  as measured directly in front of the atomic beam apparatus, i.e. after passing through the beam transport optics, was  $\sim 15 \text{ mW}$ ; the actually generated power inside the crystal was almost twice higher (see Section 4.7). The corresponding internal laser power was 25 - 30 W. The above values apply to a pump power of 2.2 W at  $\lambda = 457.9 \text{ nm}$  and to a path through the crystal where the insertion loss was lowest. Routinely values of 5 - 10 mW in front of the atomic beam apparatus were obtained, depending on the age of the dye solution, the pump power delivered by the  $\text{Ar}^+$  laser and the performance of the crystal at the spot being used.

For power monitoring the beam leaving the atomic beam apparatus has been used. Its intensity, attenuated by a factor of 50 by a 2 mm thick color glass filter UG11 (Schott), has been measured with a photodiode type PIN-10 (United Detector Technology). The photodiode was roughly calibrated by comparison with the values measured in front of the atomic beam apparatus with a pyroelectric power meter type Rk 5100 (Laser Precision Corp.), which was always used for absolute power measurements.

The observed angular and frequency bandwidths were  $\Delta\Theta_m \sim 9'$  and  $\Delta\nu_{fund} \sim 1100 \text{ GHz}$ , respectively, both about a factor of 8 higher than calculated (see Section 4.6a); the reason for this discrepancy probably is that we have not a plane wave as assumed for the calculations, but a sharply focused waist.

e) Crystal degradation

After a few months of normal use an unexpected and so far unexplained phenomenon in the BBO crystal's performance has been observed. When generating UV, an abrupt avalanche-like drop of the fundamental power (and a corresponding drop of the UV power) was observed after a certain waiting time, which ranged from a few seconds to a few minutes depending on the crystal spot used; the fundamental power dropped to 30 - 70% of the initial value. The avalanche time constant was

found to be 5 - 6 s. Another feature of the phenomenon was a subsequent recovery if the UV generation was continued. The internal power usually returned to 70 - 90%, and in some cases even to 100% of the original value. This relaxation required usually 10 - 30 min, in some cases longer. The observed phenomenon is most likely caused by an increase of the crystal's loss for the fundamental wavelength; the increase, however, doesn't exceed 2 - 3%. A record of this behavior is presented in Fig. 4.18.

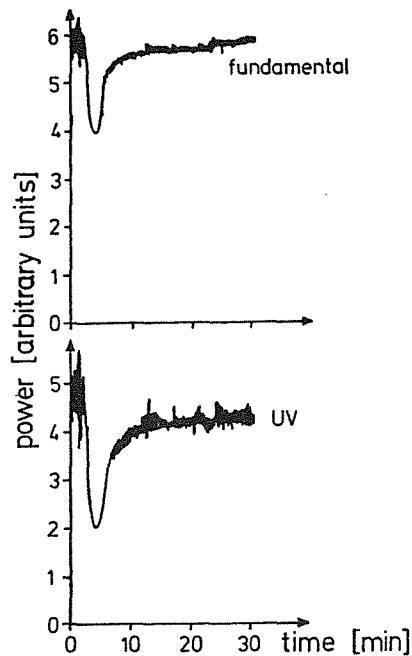


Fig. 4.18 Record of an unexplained phenomenon observed in the BBO crystal; the following characteristic features can be seen: after some delay time (in this case 3 min) an abrupt decrease of the internal power (mainly caused by an increase of the loss for the fundamental in the crystal) and partial restoration thereafter.

The ratio  $P(2\omega)/P^2(\omega)$  is rather constant during the process, which means that if any increase of the loss for the UV is involved, it must be small. The UV loss of a few % cannot be excluded, as the normal UV power fluctuations are of this order.

It has been found that the power changes require the presence of the UV light; this is demonstrated in Fig. 4.19 for the avalanche power drop. The internal laser beam was interrupted during the avalanche process which stopped the degradation. It continued thereafter at the same intensity as immediately before the interruption.

Fig. 4.20 shows the fundamental power as the crystal was shifted perpendicular to the beam direction; these records reflect the loss profiles for the fundamental wave-

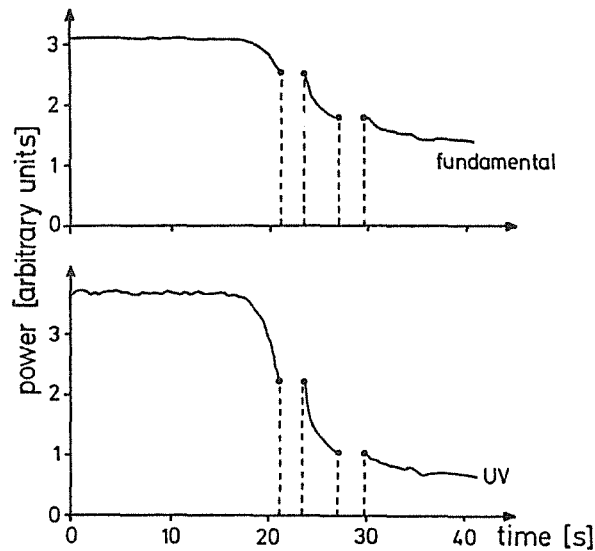


Fig. 4.19 Time resolved record of the abrupt internal power drop (increase of the loss) - demonstrating that the loss is frozen during the interrupt of the internal laser beam.

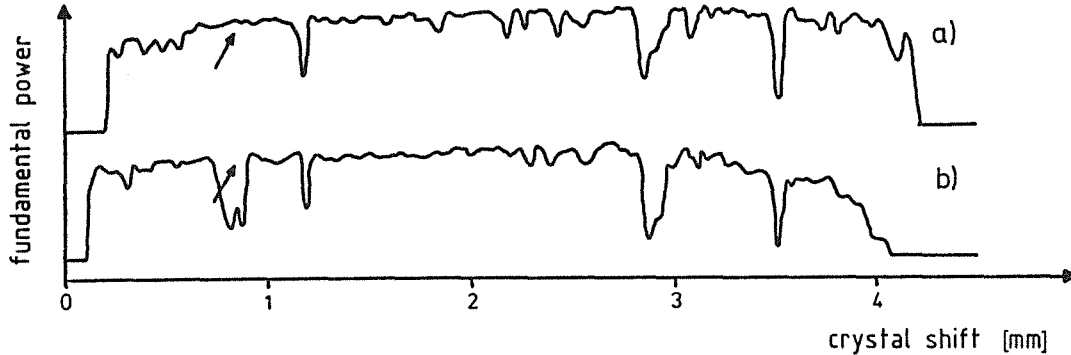


Fig. 4.20 Comparison of the power profiles for the fundamental wavelength without UV generation: a) before and b) after observing a power drop on one spot under UV generation (without waiting for restoration). The degraded spot is marked by arrows.

length across the crystal. They were taken before and after observation of a power drop (without allowing it to restore); the local degradation is marked by an arrow. The other low-power spots might be a result of the same effect having occurred in the past without being noticed - see below in this section.

This avalanche phenomenon has only been observed with UV generation. There are also spots found on the crystal where it doesn't occur, at least within many hours of operation; all acceptable spots used before the first observation of the

avalanche drop phenomenon had been of this kind. It seems as if the crystal had some grain structure with different absorptive properties. Until now the nature and reasons of the crystal's behavior are unexplained.

One might speculate that some sort of absorption (e.g. color centers) is created; its creation is somehow hindered in the beginning but after some waiting time an avalanche is triggered. It is unclear, though, how the beam bleaches its path through the crystal thereafter. It might as well be that the absorbing medium is created on the crystal's surface or only in small areas along the beam path inside the crystal.

Another description of the appearance of the phenomenon might be that all that has changed is that the waiting time for the avalanche power drop has somehow increased. Previously the spots with poor performance were immediately discarded as "bad" and no healing was awaited for. The low power spots found in both traces of Fig. 4.20 might be such remnants of power drops without restoration. However, our impression is that now much less spots are of the kind without power drop whereas the majority is of the avalanche type.

No attempts have been made so far to heal the defects or to influence the crystal's performance by tempering.

#### 4.7 UV transport optics

The UV beam in the interaction zone should have a relatively small cross-section, not exceeding this of the atomic beam. The optimum UV beam shape would be elongated in horizontal direction, i.e. in the direction in which the fluorescence is detected, as the corresponding dimension of the atomic beam is about 3 mm. Because of the diaphragms installed in both the entrance and exit arms of the atomic beam apparatus [Pi 88], a nearly round shape is, however, preferred. The distance between the UV output coupler and the interaction zone is 8 m.

The UV beam leaves the CR 699-21 resonator having different divergences in the horizontal and the vertical directions. This is due to the different UV waist sizes in these directions:  $w_0^{vert} \approx 30 \mu\text{m}$  and  $w_0^{horiz} \approx 210 \mu\text{m}$ . Therefore use of at least one cylindrical lens was necessary in order to obtain an approximately collimated round UV beam. A cylindrical lens with a focal length  $f_c = 310 \text{ mm}$  was placed at a distance of about 25 cm away from the waist in the crystal with its axis horizontal in order to reduce the beam divergence in the vertical direction; thus it becomes very similar to the divergence in the horizontal direction. For further beam collimation spherical optics was used. A good UV beam size and shape in the interaction zone, as well as minimum beam divergence in its vicinity, were obtained with the

use of one spherical lens with the focal length  $f_s = 1000$  mm, placed  $\sim 90$  cm from the waist in the crystal. The UV beam in the interaction zone was approximately round, of  $\sim 1.5$  mm diameter, its size at the entrance and exit windows of the atomic beam apparatus being less than 3 mm. In this way the beam cleared all the diaphragms installed inside the entrance and exit arms of the apparatus and thus unnecessary light scattering was avoided.

The beam steering and forming system consists of the above described two lenses and four folding mirrors coated for  $\lambda \approx 300$  nm for normal incidence; here they were used at incidence angles of  $40^\circ - 50^\circ$ . For these angles their transmission at  $\lambda = 255.8$  nm amounts to  $\leq 0.1\%$  (measured with a Perkin-Elmer Lambda 9 Spectrometer, see Fig. 4.21). The total loss introduced by the UV transport system was found to be  $\sim 15\%$ . Since the losses for the UV inside the laser resonator amounted to 30 - 35% (see Section 4.5), altogether 55 - 60% of the generated UV power was actually used for the experiment.

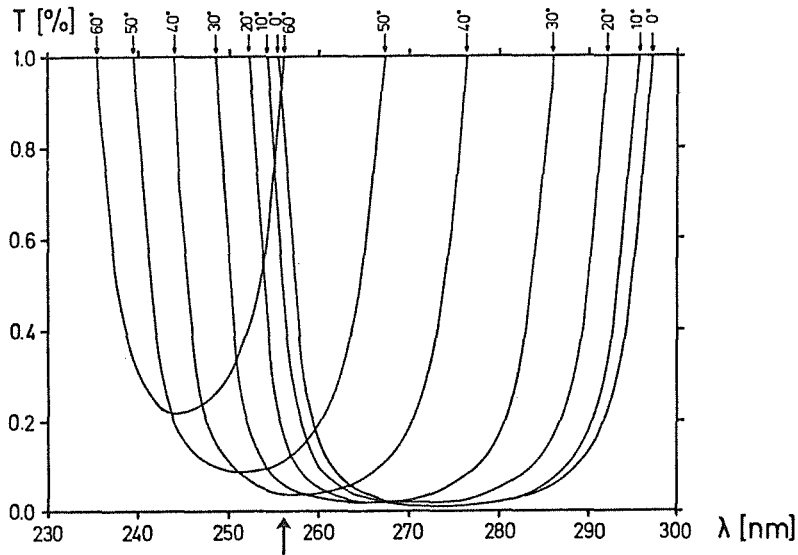


Fig. 4.21 Transmission curves for the mirrors used as folding mirrors in the UV transport system, for various angles of incidence.

#### 4.8 Controls

In order to assure the coincidence of this laser frequency with that of the atomic transition studied, the frequency is controlled in several ways. For this purpose the fundamental beam transmitted through the dichroic upper-fold mirror was used. The mirror's transmission is  $\sim 0.35\%$  for the fundamental wavelength (Fig. 4.2), and

the beam intensity normally amounted to 50 - 100 mW, which is more than enough for this purpose.

Single-mode operation was controlled by two confocal scanning FP interferometers with FSRs 2 GHz and 10 GHz. This combination also allowed to detect the frequency jumps of  $\pm 1$  GHz off the selected frequency.

In order to find the required absolute frequency for the chosen atomic transition in polonium, a fluorescence spectrum of molecular iodine was recorded and compared with the standard spectrum [GL 78]. The once identified spectrum was then used as a control and displayed on the scope while tuning the laser.

For the measurement of frequency changes a wavemeter was used, whose principle of operation is described in [St 84]. After improvements of its performance, its accuracy has been determined to be as follows [Sc 90]:

- for single readings:  $\pm 15$  MHz,
- for frequency values taken from a fit line, as used in fits of the spectra (see Section 6.2):  $\pm (2 - 4)$  MHz.

## 5 Experiments

### 5.1 Isotope production and sample preparation

The series of polonium isotopes studied ( $^{200}\text{Po}$ ,  $^{202}\text{Po}$  and  $^{204}$  to  $^{210}\text{Po}$ ) comprises the isotopes with neutron numbers ranging from 116 to 126 (magic N) and lifetimes from 11.5 min ( $^{200}\text{Po}$ ) to 102 years ( $^{209}\text{Po}$ ). According to these two parameters the methods of isotope production and sample preparation varied. Generally the series of isotopes given above can be divided into three groups, as far as the sources are concerned:

- a) purchased isotopes ( $T_{1/2} > 100$  days),
- b) isotopes obtained from Bi targets,
- c) isotopes obtained from Pb targets.

All the isotope lifetimes and sources are listed in Table 5.1.

All the isotopes with lifetimes of the order of days or hours were produced either in the Karlsruhe Isochronous Cyclotron - KIZ (deuteron and  $\alpha$ -irradiation) or in the Karlsruhe Compact Cyclotron - KAZ (proton irradiation). For the production of the isotopes  $^{202}$  to  $^{207}\text{Po}$  a standard construction of the target holder for the irradiation with a water-cooled target was used. The reaction cross-section at the energy available with this construction ranged from 0.5 barn ( $^{202}\text{Po}$ ) to 1.1 barn ( $^{205}\text{Po}$ ); the

Table 5.1 Po isotope investigated - lifetimes and sources.

isotope	T <sub>1/2</sub>	source
210	138 d	10 ng in HCl solution (Amersham-Buchler)
209	102 a	50 ng in HNO <sub>3</sub> solution (ORNL, USA)
208	2.9 a	20 ng in HCl solution (Amersham-Buchler)
207	5.8 h	<sup>209</sup> Bi(p,3n)
206	8.8 d	<sup>209</sup> Bi(d,5n)
205	1.7 h	<sup>206</sup> Pb(α,5n)
204	3.5 h	<sup>206</sup> Pb(α,6n)
202	0.7 h	<sup>204</sup> Pb(α,6n)
200	0.2 h	<sup>204</sup> Pb(α,8n)

amounts obtainable for an irradiation of T<sub>1/2</sub> duration with a current of 1 μA were at least 1 ng (<sup>202</sup>Po).

The case of <sup>200</sup>Po, on the other hand, presented some problems as far as the obtainable amount of material was concerned, as the reaction cross-section for the (α,8n) reaction is generally very small. At the full KIZ energy of 103.5 MeV, the cross-section of the reaction <sup>204</sup>Pb the (α,8n) amounts to ~0.3 barn, which is close to optimum. If a target holder with water cooling is used, a part of the energy is lost in the water layer with a minimum thickness of 1.1 mm (the loss is 10.15 MeV) and a copper foil, serving as a window, with a thickness of 0.1 mm (loss 4.75 MeV). As a result the maximum available irradiation energy is only 88.6 MeV for this target holder; the reaction cross-section then is only 0.035 barn. This was not found acceptable since then only a few pg of <sup>200</sup>Po were produced.

Therefore for the production of this isotope a modified construction of the target holder without water cooling was developed so that the full cyclotron energy is used. For that purpose a so-called clamp target holder was adapted. A Pb foil with a thickness of 200 μm and a diameter of 5 mm is clamped between two copper plates (see Fig.5.1); the plates have holes of 4 mm diameter which determine the actual target surface exposed to the irradiation; the distance between the plates, determined by the spacers, is 100 μm so that the Pb target is compressed to that thickness at the edge. The target irradiation current measurement is performed in a standard way, i.e. the copper plates are connected with an appropriate contact point on the clamp target holder, provided for this purpose. To center the α-beam on the target and thus assure that the current measured is that of the Pb target foil and not that of the copper clamp (which is otherwise undistinguishable), a graphite

diaphragm with a diameter of 4 mm is mounted in front of the copper clamp; it is electrically insulated from the clamp by boron nitride spacers and its current is measured independently. It has been found that the target and the diaphragm currents are approximately equal if the  $\alpha$ -beam is centered with respect to the target.

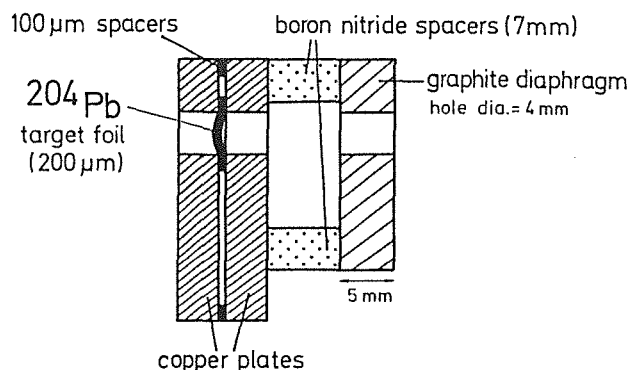


Fig. 5.1 Target holder without direct target water cooling, used for the  $^{200}\text{Po}$  production.

In the new construction the entire  $\alpha$  energy loss dissipated in the Pb target foil is conducted radially to the clamped circumference of the target. It is not a very efficient cooling, and the Pb target foil temperature can reach rather high values under irradiation so that the target eventually melts. Calculations of target temperatures have been performed; a simplified model of uniform irradiation of the target was applied. It was found that the temperature difference between the center of the target where the temperature is peaking and its edges (which are assumed to be held at room temperature) amounts to 12 K/W. Since the  $\alpha$  energy loss in a Pb target foil of 200  $\mu\text{m}$  thickness amounts to  $\sim 7$  MeV, the above value of the temperature difference can be expressed as  $\sim 400$  K/ $\mu\text{A}$ .

The simplified model assumed for the calculations allows only the order of magnitude to be estimated, so a series of experiments followed (using natural lead targets instead of  $^{204}\text{Pb}$ ) to determine the actual highest  $\alpha$ -current which could be applied. The  $\alpha$  currents which caused melting of the target in its center was found to lie between 2.0  $\mu\text{A}$  and 2.5  $\mu\text{A}$ , so for the actual  $^{200}\text{Po}$  production a current of 2  $\mu\text{A}$  was used.

The amount actually available for the experiment was 13 pg, being approximately 1/4 of the amount produced, as the time between the end of the irradiation and the beginning of the measurement was about  $2 \cdot T_{1/2}$ .

Sample preparation and sample form varied also from one isotope group to another.

In the case of the long-lived purchased isotopes polonium could be spontaneously deposited from the acid solution (see Table 5.1) onto a Ni-foil immersed in it as Po is chemically more inert than Ni. This is the most favorable sample form for an atomic beam experiment, as the material is gathered on the surface and therefore evaporizes most readily.

A similar sample form was obtained for the two isotopes produced from Bi, provided bismuth oxide targets were used instead of metallic bismuth; the only difference as compared to the long-lived isotopes samples described above was the use of Ag- instead of Ni-foils. Bismuth oxide is easily soluble in HCl; irradiated  $\text{Bi}_2\text{O}_3$  target were dissolved in 3n-HCl [FH 90], the solution was heated to 60°C and the Ag-foil immersed into it. After 60 min most of polonium was deposited onto the foil. Bismuth, on the contrary, is not deposited in this process as it is less inert than Ag.

For the third group of isotopes the lead targets were directly used. As Po evaporates more readily than Pb, no serious problems were expected in evaporating it from the bulk of the target; moreover a crucible heated preferably in its lower part [FH 90] was used so that the evaporated lead was partially recondensed in its upper part. Experiments proved that this scheme works satisfactorily - no problems were encountered unless an extreme heating power was applied.

## 5.2 Measurement programs

Control and tuning of the laser frequency and corresponding data acquisition are performed by means of a PDP-11 computer.

The laser frequency is scanned stepwise by supplying the CR 699-21 control unit with adequate voltages from a DAC fed from the computer; the frequency step width is variable. The frequency range to be scanned over can be selected by choosing a proper scan width and a center frequency. Several frequency intervals of equal width can be selected by entering a corresponding number of center points (up to 10); thus the frequency can be scanned around the expected positions of the resonances while leaving out the uninteresting intervals in between. In a standard version of the program overlapping ranges are not repeated; in a modified version repetitions are allowed, i.e. a selected interval can be scanned over more than once in one spectrum if the corresponding center point is specified several times; then count rates for the repeated frequency points can be summed up if required. This version is used whenever some of the resonances to be measured are expected to be much weaker than others (e.g. weak spectral components of an odd-mass isotope vs a strong spectral line of an even-mass isotope, taken as reference). All the above parameters concerning the frequency stepping can be varied within the range

allowed by the total scan range set in the CR 699-21 control unit; the smallest frequency increment is equal to the total scan range/4096 (4096 being the number of the DAC's steps).

For every step the laser frequency is measured by a wavemeter (see Section 4.8) and fluorescence count rates are measured during a selected integration time; for the measurements on polonium an integration time of 250 ms has been used throughout. For reference also other relevant signals can be recorded simultaneously; in our case the iodine fluorescence spectrum (see Section 4.8) and the UV power have been recorded in parallel.

### 5.3 Signal and background count rates

#### a) Background count rates

The background counts result from several effects. Their contributions to the observed count rates vary widely:

- photomultiplier dark current:  $\sim 60$  Hz at a temperature of  $-5^{\circ}\text{C}$ ;
- scattering of the exciting UV light and fluorescence of the optics (mostly in the blue-violet range):
  - $\sim 70$  Hz per mW of incident UV light; this applies to a situation with filtering through the interference filter with  $\lambda = 256$  nm so that all fluorescence light outside the filter passband is blocked (see Section 3.3),
  - $\sim 1200$  Hz per mW of UV without interference filter, as used for the measurement of  $^{200}\text{Po}$ ;
- oven glow light: 20 - 30 Hz with the interference filter  $\lambda = 256$  nm, 80 - 100 Hz without interference filter;
- $\gamma$ -radiation and the fluorescence caused by it: depending on the isotope's  $\gamma$  energy spectrum, lifetime and the sample size - up to several kHz with the interference filter  $\lambda = 256$  nm and 50 - 60 kHz in the case of  $^{200}\text{Po}$  without interference filter.

For all short-lived isotopes ( $T_{1/2} < 1$  d) the background count rate was mainly due to the  $\gamma$ -radiation, the other contributions being irrelevant in this context.

#### b) Signal noise

The noise is caused by the fluctuations of the total count rate; it influences the attainable quality of the fit of the spectra and thus the accuracy with which the center frequencies of the components can be determined (see Section 6.1). The relative

signal and background count rates varied considerably; roughly two categories could be distinguished:

- polonium signal  $>$  background signal  
the best cases -  $^{208}\text{Po}$ ,  $^{209}\text{Po}$  (component c, see Fig.5.5a),  $^{210}\text{Po}$ : peak signal count rates up to 40,000 Hz, background count rate 160 - 400 Hz; into this category also fall almost even-mass isotopes (including  $^{202}\text{Po}$ , only  $^{200}\text{Po}$  is to be excluded) and well-resolved, relatively strong components of odd-mass isotopes; the influence of the noise on the uncertainty of the center frequencies is negligible in comparison to other sources of errors (see Chapter 7, Section 7.1);
- polonium signal  $<$  background signal  
the worst case is  $^{200}\text{Po}$ : signal count rate  $\sim 6,000$  Hz, background count rate  $\sim 60,000$  Hz; in this category also weak components of odd-mass isotopes are to be included; the noise influences the accuracy of center frequency determination to a degree comparable to other sources of the errors, but not more.

c) Total signal counts - crucible comparison

The performance of a graphite and a molybdenum crucible was compared for  $^{206}\text{Po}$  evaporated from a Pb-target. For future reference (e.g. to control the sensitivity of the detection system) total signal counts were determined. For a graphite crucible  $\sim 2 \cdot 10^7$  counts/ng were obtained, for a molybdenum crucible the corresponding value was  $\sim 10\%$  lower. The above values apply to a UV power used for excitation of  $\sim 1.5$  mW.

#### 5.4 Isotope shift and hyperfine structure measurements

Measurements were performed for 9 Po isotopes:  $^{200}\text{Po}$ ,  $^{202}\text{Po}$  and the series  $^{204}$  to  $^{210}\text{Po}$ . The laser frequency was scanned stepwise around the expected positions of the resonances. Fig. 5.2 is a compilation of the spectra obtained.

a) Even-mass isotopes

All the even-mass polonium isotopes have nuclear spin  $I=0$  and thus no hyperfine structure. With only one spectral component, even-mass isotopes were the easiest to be studied. The most obvious reason is that the isotope shift is then determined as soon as the relative position of this only component has been measured, but the case is also most favorable from the point of view of the signal strength.

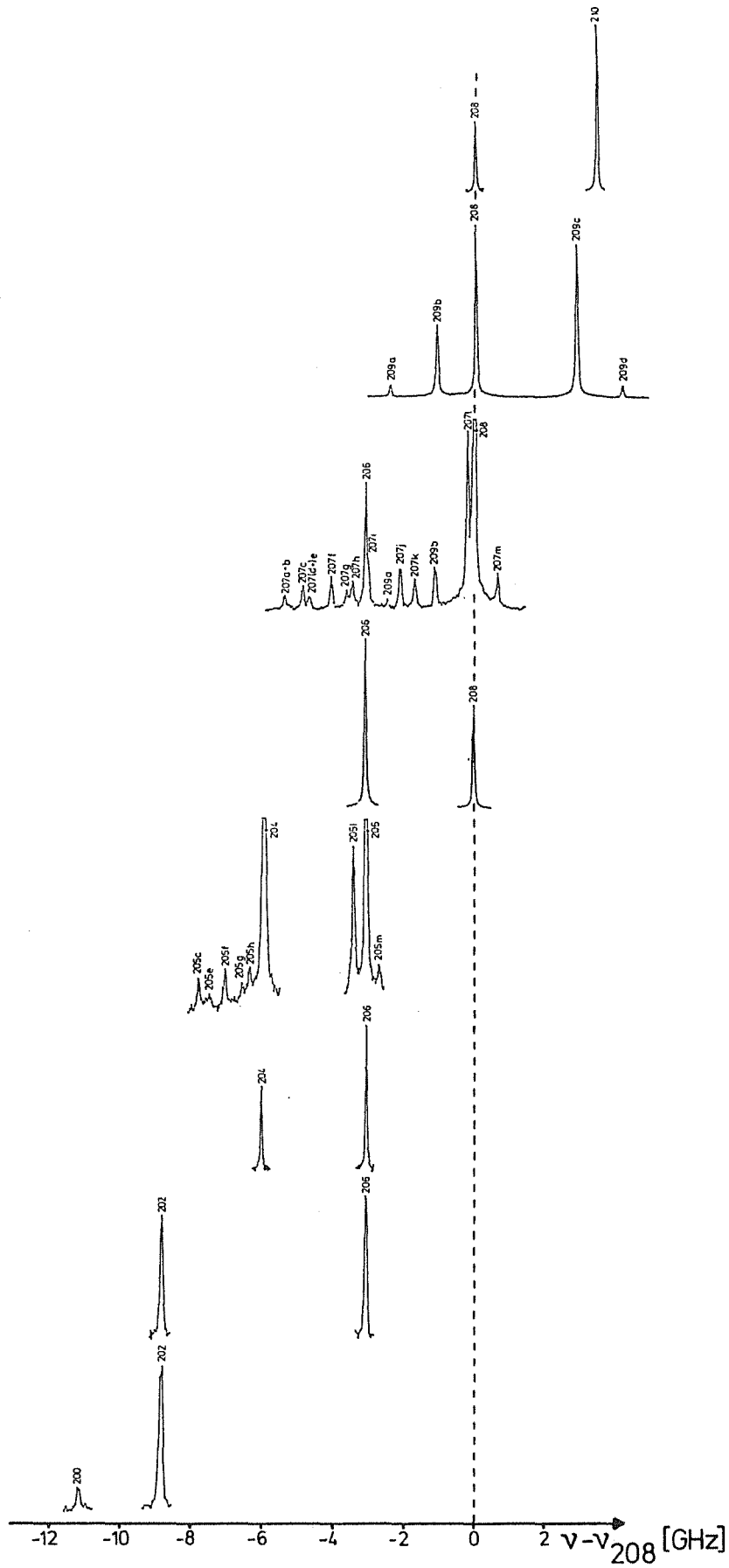


Fig. 5.2 Spectra of all polonium isotopes investigated in this work.

Because the ground state is not splitted, all the atoms passing through the interaction zone, which are in the ground state, can be excited at almost the same frequency (within some small interval, depending on the lifetime of the upper level and velocity distribution of the atoms in the light beam direction). Moreover, those of the atoms which decay to the ground state are again all in the proper state for further excitation. The duration of the atoms' passage through the interaction zone

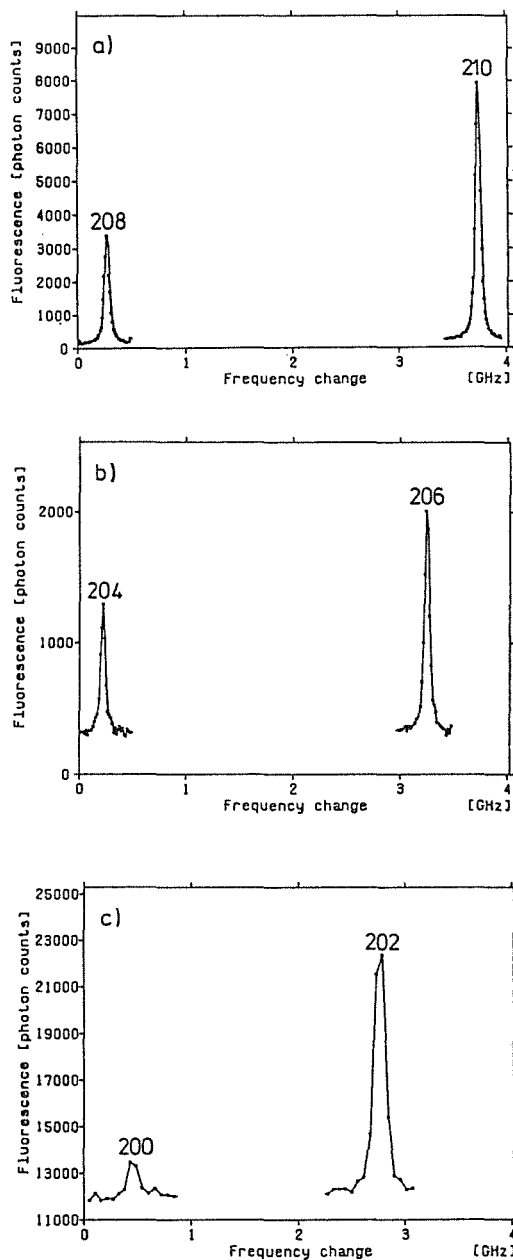


Fig. 5.3 Examples of the spectra of even-mass Po isotopes:  
a)  $^{208}$  and  $^{210}\text{Po}$ , sample size:  $^{208}\text{Po}$ : 550 pg,  $^{210}\text{Po}$ :  $\sim 1.4$  ng (one of 50 scans);  
b)  $^{204}$  and  $^{206}\text{Po}$ , sample size:  $^{204}\text{Po}$ : 150 pg,  $^{206}\text{Po}$ :  $\sim 300$  pg (one of 30 scans);  
c)  $^{200}$  and  $^{202}\text{Po}$ , sample size:  $^{200}\text{Po}$ : 13 pg,  $^{202}\text{Po}$ :  $\sim 70$  pg (one of 30 scans).

is  $\sim 3 \mu\text{s}$  for temperatures of  $500^\circ\text{C}$  -  $1000^\circ\text{C}$  and the estimated lifetime of the upper level is  $\sim 30 \text{ ns}$ ; this means that if fine structure pumping (i.e. a decay to other states of the ground configuration) could be neglected, 100-fold excitation of every atom were allowed. As a consequence the signals obtained were strong and - if sufficient exciting light power is applied - limited only by the dead time of the photon counting system. The sensitivity can be still increased at the expense of the resolution (i.e. by using a lower degree of collimation of the atomic beam) as the latter needn't be particularly high in this case.

For polonium even-mass isotopes sample sizes of  $\sim 100 \text{ pg}$  were found very convenient for the measurements but even samples of  $10 - 15 \text{ pg}$  could be studied. A few examples of the spectra are shown in Fig. 5.3. The first two of them allow a comparison of the signal sizes obtainable with various sample sizes, as in both cases the same atomic beam collimation of  $2.5^\circ$  full angle and similar UV powers for the excitation were used. In the last case, i.e.  $^{200}\text{Po}$ , a direct comparison to the previous two is not possible because of different experimental conditions applied. In this case the maximum collimating slit width for the atomic beam was used (the resulting collimation degree was  $7.3^\circ$  full angle) and, moreover, the interference filter was removed from the fluorescence detection system to increase the count rate by a factor of 4 (100% instead of 35% transmission at  $\lambda = 255.8 \text{ nm}$  and, additionally, 100% instead of 0% transmission at  $\lambda = 449.3 \text{ nm}$ , the latter transition being approximately half as strong as the former).

#### b) Odd-mass isotopes

Odd-mass isotopes present a more difficult case to be studied than the even-mass ones. The signal strength is greatly reduced because of the hyperfine splitting of the ground state. The total population of the ground state is spread, the populations of the hyperfine levels being proportional to  $2 \cdot F_{\text{lower}} + 1$ , and only a certain fraction of the total number of atoms passing through the interaction zone can give rise to a particular spectral component. After excitation part of the atoms decay to a "false" level and cannot be excited again (so-called hyperfine structure pumping).

As a consequence of the reduced signal strength larger sample sizes have to be used than in the case of even-mass isotopes; these depend on the splitting of the ground state. Typical sample sizes required were of the order of  $500 \text{ pg}$ , however, for convenience (i.e. better signal to noise ratio and possible measurement of several spectral components at a time) normally sample sizes of  $1 - 2 \text{ ng}$  were used if that could be afforded. Usually a rough survey spectrum was taken at first in order to identify the spectral components and later on several selected ones were remeasured with higher accuracy. An example of a survey spectrum and corresponding

hyperfine structure level scheme is presented in Fig. 5.4; Fig. 5.5 shows the final, more precise spectra.

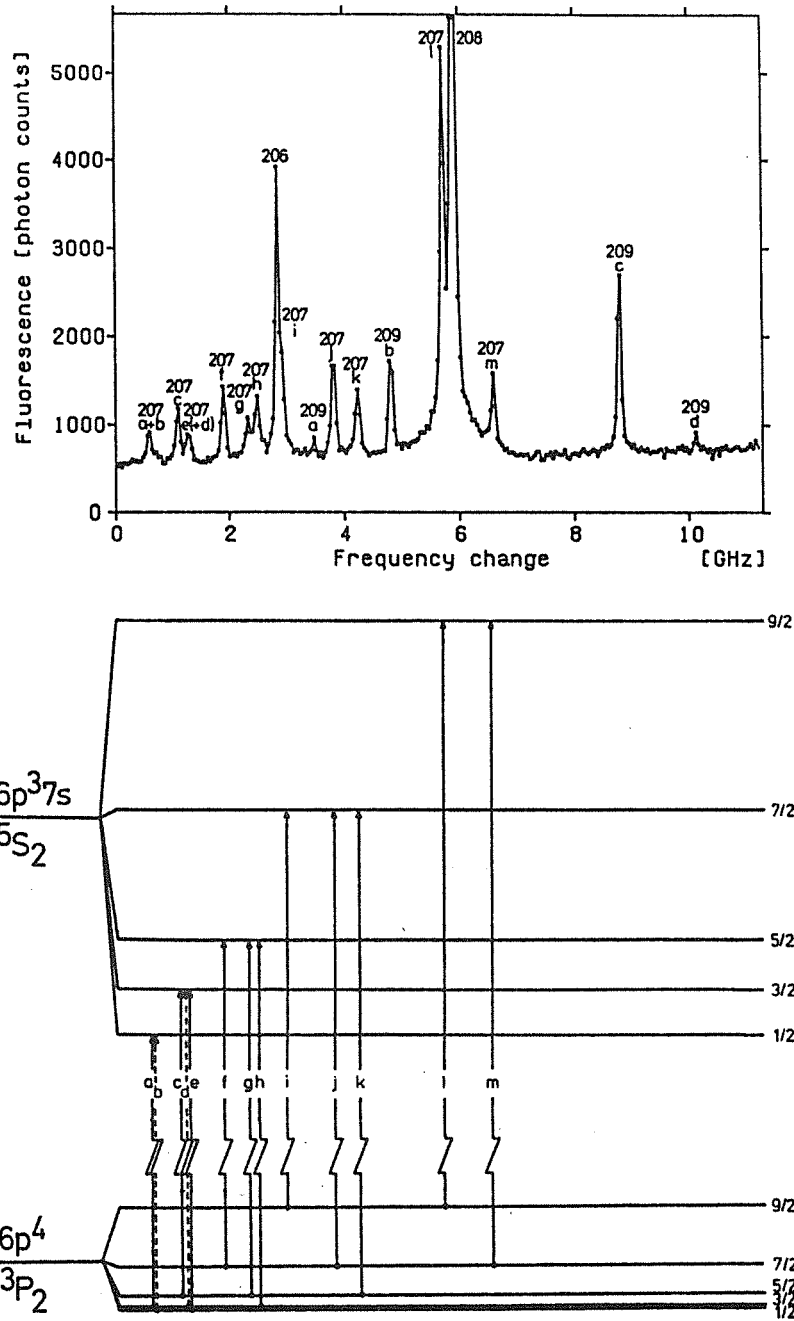


Fig. 5.4 Survey spectrum of  $^{207}\text{Po}$ ; spectral components of two even-mass isotopes ( $^{206}\text{Po}$  and  $^{208}\text{Po}$ ) and another odd-mass isotope ( $^{209}\text{Po}$ ) are also visible. On the HFS level scheme for  $^{207}\text{Po}$  (to-scale, as far as the splittings are concerned) all the transitions are shown. The question of identification of the components is dealt with in Chapter 6 (Section 6.3).

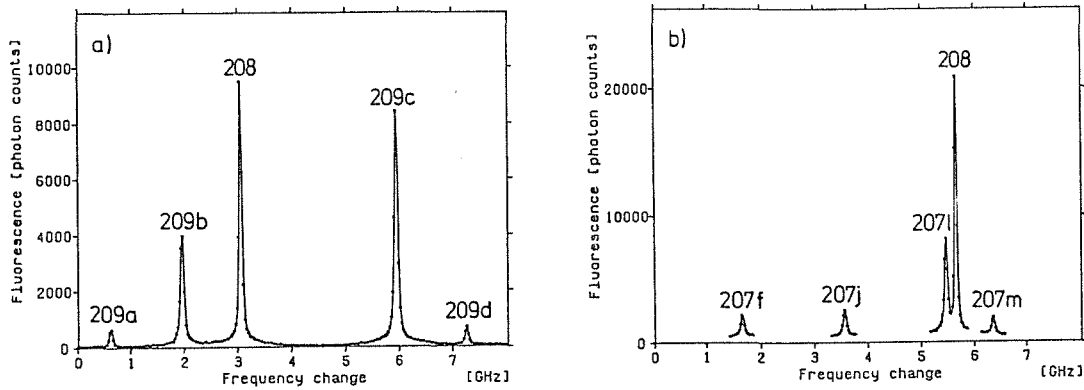


Fig. 5.5 Spectra with an improved resolution for odd-mass isotopes: a)  $^{209}\text{Po}$ , b)  $^{207}\text{Po}$ .

## 6 Data evaluation

### 6.1 Fits of the spectra

The line shape in the measured spectra comprises essentially two contributions: a) a natural line shape - Lorentzian and b) Doppler broadening - Gaussian; thus the overall line shape is expected to be a Voigt profile. Fitting procedures involving a Voigt profile in a general case are, however, rather unhandy and not necessary in our case (see below).

One of the most important points when fitting a theoretical symmetric curve to an experimental one is that the latter be also symmetric. It has been found that the observed lines in the spectra of polonium fulfilled this requirement. A number of them was fitted to both a Lorentzian and a Gaussian profile. In spite of the fact that neither of the two assumed profiles seemed to be quite adequate, the center frequencies determined in both cases were in a very good agreement with each other, i.e. the differences were found considerably smaller than the errors resulting from the quality of the fit. As the shape of the profile fitted to the experimental lines proved to have only a negligible influence on the determined center frequency, which is in this case the only parameter of interest, all the spectra were least-squares fitted to Lorentzian profiles.

The fitting program treats the frequency axis  $\nu_i$  (abscissa) as error-free, i.e. as controlled variable; the counts (ordinates)  $y_i$  are given errors  $\delta y_i = \sqrt{y_i}$ , i.e. they are weighed as  $w_i = 1/\delta y_i$ ; such errors are underestimates of the real uncertainties. The error estimate of the center frequency  $\delta \nu_{center}$ , as resulting from the above given weights through the fit, in most cases was found to be below 1 MHz (in laser

frequency), only for weak hyperfine components and for  $^{200}\text{Po}$  it amounted to a few MHz (as an example - see Fig.6.1:  $^{200}\text{Po}$  and  $^{202}\text{Po}$ ); they can be considered as unrealistically low. More realistic estimates of the errors could have been obtained if the accuracy of the frequency axis  $\delta\nu_i$  (see Section 6.2) were included in the Lorentz fit procedure as well. The solution to the problem where both abscissa and ordinate are subject to error simultaneously is not straightforward. One could, however, proceed in the following way: "translate" the abscissa errors  $\delta\nu_i$  into equivalent ordinate errors  $\delta y_i$ , proportional to the local slope  $y_i'$  of the model curve:  $\delta\tilde{y}_i = y_i' \cdot \delta\nu_i$ ; in the curve fitting procedure total errors  $\Delta y_i$  are to be used, that are appropriate combinations of  $\delta y_i$  and  $\delta\tilde{y}_i$ .

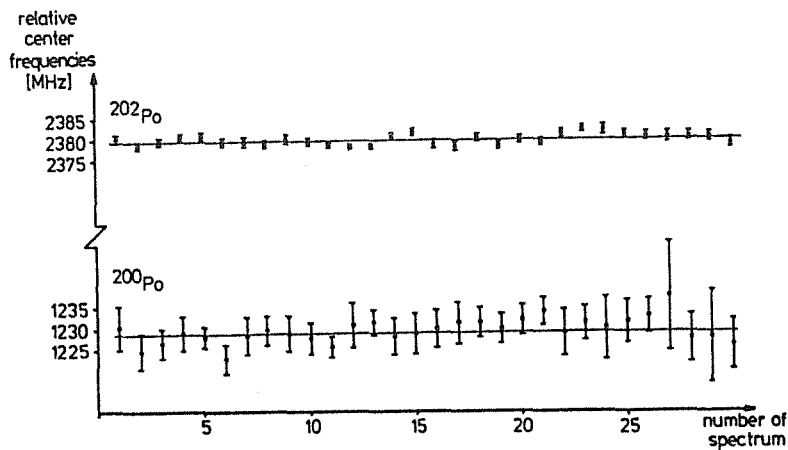


Fig.6.1 Center frequencies (on the laser frequency level) of the spectral lines of  $^{200}\text{Po}$  and  $^{202}\text{Po}$ , measured in 30 scans relative to an arbitrarily chosen reference frequency, corresponding to a multiple of the FSR of the longest interferometer in the wavemeter (see Section 6.2).

Instead of the rather unhandy procedure suggested above another alternative could be used. The example of  $^{207}\text{Po}$ , where some of the frequency differences are known to good accuracy [OAL 61] (and other measurements, see further), allowed an experimentally substantiated estimate of our frequency accuracy; it proved that purely statistical uncertainties are not adequate estimates of the actual errors (for details - see Section 6.3, p. 54, for the final comprehensive discussion of the error estimates - Chapter 7, Section 7.1, p. 61)

## 6.2 Frequency axis

For the measurements of the laser frequency changes a wavemeter is used [St 84, Sc 90]. Its accuracy and precision have been determined in another experiment by simultaneous measurements of the frequency changes by a beat frequency

method and by the wavemeter [Sc 90]. For calibration of the frequency axis the FSR of the longest interferometer in the wavemeter has been taken to be 1.49933(3) GHz [Kä 90].

Frequency changes measured by the wavemeter have a single reading worst case errors of  $\pm 15$  MHz. If the laser is scanned upwards stepwise by 10 MHz or less, it happens that a lower frequency is measured for a subsequent step whereas in reality the frequency increases; thus adjacent steps can be confused. For scans the accuracy of the frequency measurement can be, however, considerably increased if the frequency readings are smoothed over some interval. In order to obtain an improved frequency axis for the fits of the spectra, for each point a corresponding straight line is fitted by linear regression within a range of  $\pm 250$  MHz with this point as center; this allows obtaining the improved measurements and - in particular - reduced errors for the center frequency point. This procedure is performed for every frequency point, i.e. its measured value is replaced by that one obtained from an interval around it. The smoothed frequency scale obtained in this way is finally used. The accuracy for a single frequency point is then  $\pm (2 - 4)$  MHz, depending on the density of the measured points (i.e. number of points in the  $\pm 250$  MHz frequency interval).

### 6.3 Identification of hyperfine components

#### a) General

In the case of the even-mass polonium isotopes the isotope shifts are measured directly, as frequency differences between the spectral lines belonging to each of them. For the odd-mass isotopes the center of gravity of a hyperfine spectrum has to be determined. This can be done only if at least  $k + 1$  of the observed components ( $k$  is the number of the HFS parameters to be determined plus the center of gravity, see below) are identified. The odd-mass polonium isotopes measured in this work have the nuclear spin values:  $I = 1/2$  ( $^{209}\text{Po}$ ) and  $I = 5/2$  ( $^{205}\text{Po}$  and  $^{207}\text{Po}$ ). For the atomic transition studied (with  $J_{\text{lower}} = 2$  and  $J_{\text{upper}} = 2$ , see Chapter 2, Section 2.1) these angular momenta give rise to 4 and 13 spectral components, respectively.

In a general case the identification of components (i.e. a correct assignment of  $F_{\text{lower}}$ ,  $F_{\text{upper}}$  pairs to observed peaks) is a rather complex problem. In principle all possible combinations of assigning the observed spectral components to the possible hyperfine transitions have to be checked [cf. Kä 88]. The number of possible assignments is  $n! / (n - r)!$ , where  $n$  is the number of the possible transitions and  $r$  is the number of observed components. For all assignments the corresponding hyperfine splitting factors  $A$  and  $B$  for both the lower and the upper level of the transition as well as the center of gravity can be determined, e.g. by a least-squares

fit. Then some statistical test has to be performed, usually a  $\chi^2$ -test, to reject incorrect assignments, which is quite powerful if the fit has several degrees of freedom. The least squares test parameter  $M$  is the sum of squares of the weighted (weights:  $1/\Delta v_i^2$  where  $\Delta v_i$  are standard deviations) differences between the measured frequency values  $v_i^{meas}$  and the recalculated values  $v_i^{calc}$  obtained in the fit [Br 70]:

$$M = \sum_{i=1}^r \frac{\left( v_i^{meas} - v_i^{calc} \right)^2}{\Delta v_i^2} \quad (6.1)$$

This test parameter  $M$  has to be compared with a  $\chi^2$  value for  $(r-k)$  degrees of freedom, where  $k$  is the number of parameters determined in the fit (generally  $k=5$ :  $A_{lower}$ ,  $B_{lower}$ ,  $A_{upper}$ ,  $B_{upper}$ , and center of gravity). Usually many assignments result in large  $M$  values proving them obviously contradictory; these combinations can be rejected by a  $\chi^2$ -test on a very high significance level. In order to reject possibly remaining combinations, additional information is necessary. The assignment of the observed hyperfine components for the measured odd-mass Po isotopes was based partially on  $\chi^2$ -tests, as mentioned above, and partially on additional information available (see below).

b)  $^{209}\text{Po}$

The simplest case is  $^{209}\text{Po}$  with its 4 spectral components (see Fig.5.4). In this case the number of possible assignments ( $n=r=4$ ) is only  $4!=24$ , and all of them were checked. In a first step only the hyperfine frequencies  $v_i^{meas}$  were considered (the data used are listed in the second column of Table 6.1). Three parameters had to be

Table 6.1 Measured frequencies and intensity ratios (with respect to the strongest component  $x=c$ ) of the 4 components in the spectrum of  $^{209}\text{Po}$ . The error values given are standard deviations (instead of total errors), as used in the statistical tests only.

observed component $x$	relative frequency $v_{\text{laser}}$ [MHz]	relative intensity $x/c \equiv \bar{R}(s_R)$
$a$	1029.3(0.8)	0.087(22)
$b$	1696.1(0.6)	0.615(91)
$c$	3688.8(0.3)	1 *
$d$	4354.5(0.8)	0.070(22)

\* by definition

determined in the fit ( $k=3$ ):  $A_{lower}$ ,  $A_{upper}$ , and center of gravity ( $B_{lower}=B_{upper}=0$  because of  $I=1/2$ ). All the assignments and the corresponding  $M$  values are listed in Table 6.2. 16 assignments could be rejected at an extremely high significance level:  $M \sim 10^6 - 10^7$  for  $(r-k)=1$  degree of freedom, the probability  $\alpha$  of an error of the first kind is  $\alpha \sim 10^{-200\,000} - 10^{-2\,000\,000}$ . The remaining eight are in principle indistinguish-

Table 6.2 The 24 possible assignments of the 4 components in the spectrum of  $^{209}\text{Po}$ ;  $M$  is the least-squares test parameter concerning frequencies.

No	component				$M$
	$a$	$b$	$c$	$d$	
1	3/2 → 3/2	3/2 → 5/2	5/2 → 3/2	5/2 → 5/2	0.7
2	3/2 → 3/2	3/2 → 5/2	5/2 → 5/2	5/2 → 3/2	$1.0 \cdot 10^6$
3	3/2 → 3/2	5/2 → 3/2	3/2 → 5/2	5/2 → 5/2	0.7
4	3/2 → 3/2	5/2 → 3/2	5/2 → 5/2	3/2 → 5/2	$1.0 \cdot 10^6$
5	3/2 → 3/2	5/2 → 5/2	3/2 → 5/2	5/2 → 3/2	$1.6 \cdot 10^7$
6	3/2 → 3/2	5/2 → 5/2	5/2 → 3/2	3/2 → 5/2	$1.6 \cdot 10^7$
7	3/2 → 5/2	3/2 → 3/2	5/2 → 3/2	5/2 → 5/2	$1.0 \cdot 10^6$
8	3/2 → 5/2	3/2 → 3/2	5/2 → 5/2	5/2 → 3/2	0.7
9	3/2 → 5/2	5/2 → 3/2	3/2 → 3/2	5/2 → 5/2	$1.6 \cdot 10^7$
10	3/2 → 5/2	5/2 → 3/2	5/2 → 5/2	3/2 → 3/2	$1.6 \cdot 10^7$
11	3/2 → 5/2	5/2 → 5/2	3/2 → 3/2	5/2 → 3/2	0.7
12	3/2 → 5/2	5/2 → 5/2	5/2 → 3/2	3/2 → 3/2	$1.0 \cdot 10^6$
13	5/2 → 3/2	3/2 → 3/2	3/2 → 5/2	5/2 → 5/2	$1.0 \cdot 10^6$
14	5/2 → 3/2	3/2 → 3/2	5/2 → 5/2	3/2 → 5/2	0.7
15	5/2 → 3/2	3/2 → 5/2	3/2 → 3/2	5/2 → 5/2	$1.6 \cdot 10^7$
16	5/2 → 3/2	3/2 → 5/2	5/2 → 5/2	3/2 → 3/2	$1.6 \cdot 10^7$
17	5/2 → 3/2	5/2 → 5/2	3/2 → 3/2	3/2 → 5/2	0.7
18	5/2 → 3/2	5/2 → 5/2	3/2 → 5/2	3/2 → 3/2	$1.0 \cdot 10^6$
19	5/2 → 5/2	3/2 → 3/2	3/2 → 5/2	5/2 → 3/2	$1.6 \cdot 10^7$
20	5/2 → 5/2	3/2 → 3/2	5/2 → 3/2	3/2 → 5/2	$1.6 \cdot 10^7$
21	5/2 → 5/2	3/2 → 5/2	3/2 → 3/2	5/2 → 3/2	$1.0 \cdot 10^6$
22	5/2 → 5/2	3/2 → 5/2	5/2 → 3/2	3/2 → 3/2	0.7
23	5/2 → 5/2	5/2 → 3/2	3/2 → 3/2	3/2 → 5/2	$1.0 \cdot 10^6$
24	5/2 → 5/2	5/2 → 3/2	3/2 → 5/2	3/2 → 3/2	0.7

able on the frequency basis alone: they are equally well reproduced by the Casimir formula using appropriately adjusted A factors; this symmetry is reflected by equal  $M$  values for all 8 assignments. Since  $M$  is low for these 8 assignments, so far none of them is rejected since this involved an error risk of 40%.

To reject further remaining incorrect assignments, also the observed and expected relative intensities were taken into account. The relative intensities of the components in the low power limit are as follows [Ko 58] (the subscript "l" stands for the lower and "u" for the upper level):

$$\begin{aligned} F_l = 5/2 \rightarrow F_u = 5/2 &: 100, \\ F_l = 3/2 \rightarrow F_u = 3/2 &: 64, \\ F_l = 5/2 \rightarrow F_u = 3/2 &: 7, \\ F_l = 3/2 \rightarrow F_u = 5/2 &: 7. \end{aligned}$$

Since the UV light power is non-zero, deviations from these relative intensities are possible; we can assume that no hyperfine pumping was present because the dead time of the photon counting electronics was set to a value long compared to the crossing time through the interaction zone (which amounts to  $\sim 3 \mu\text{s}$ ). The relative intensities in an asymptotic high power limit (saturation) thus were proportional to  $2 \cdot F_l + 1$ . Then the ratios of the intensities were  $(2 \cdot 5/2 + 1) : (2 \cdot 3/2 + 1) = 6 : 4 = 100 : 66.7$ , and there were no difference between the components with the same  $F_l$  but different  $F_u$ . The observed intensity pattern in the spectra is, however, clearly more similar to the unsaturated case (see Fig.5.4a); certain deviations (of the order of 10 - 20%) result most likely from the time depending heating conditions and thus non-constant atomic flow. The error estimates obtained in the fit for single scans are rather small and inadequate in view of the observed intensity variations in other scans. To account for the influence of the varying atomic flux on the observed relative intensities of the components, their intensity ratios with respect to the strongest observed component  $c$  were determined for all 7 scans and mean values were taken. The resulting standard deviations  $s_{\bar{R}}$  for the mean values of the intensity ratios  $\bar{R}$  are considerably larger than the mentioned error estimates for single scans. There was one exception found: for the intensity ratio  $d/c$  the scattering of single values happened to be rather small. For the purpose of the tests, however, the error estimate was conservatively set equal to that of the component  $a$  which has a very similar observed intensity.  $\bar{R}$  and  $s_{\bar{R}}$  as finally taken are listed in the last column of Table 6.1. Then  $t$ -tests involving the intensity ratios have been performed for all the 8 remaining assignments which were not rejected on the frequency basis alone. The test quantity  $t$  was defined as follows:

$$t = \frac{|\bar{R} - R^{theor}|}{s_{\bar{R}}} \quad (6.2)$$

$R^{theor}$  is the corresponding intensity ratio expected for the assignment under test. The  $t$  values for the tested assignments are listed in Table 6.3.

Table 6.3 Values of  $\bar{R}$ ,  $R^{theor}$  and the test quantity  $t$  for the 8 assignments of the 4 components in the spectrum of  $^{209}\text{Po}$  which cannot be rejected on the frequency basis alone.

No	$a/c: \bar{R} = 0.087(22)$		$b/c: \bar{R} = 0.615(91)$		$d/c: \bar{R} = 0.070(22)$	
	$R^{theor}$	$t$	$R^{theor}$	$t$	$R^{theor}$	$t$
1	9.1	415	1	4.3	14.3	652
3	9.1	415	1	4.3	14.3	652
8	0.07	0.8	0.64	0.3	0.07	0.02
11	0.11	1.0	1.56	10.5	0.11	1.8
14	0.07	0.8	0.64	0.3	0.07	0.02
17	0.11	1.0	1.56	10.5	0.11	1.8
22	14.3	651	1	4.3	9.1	416
24	14.3	651	1	4.3	9.1	416

6 of the 8 assignments can be rejected: No 11 and 17 with  $\alpha \sim 10^{-4}$  and No 1, 3, 22 and 24 with  $\alpha$  extremely small. Again two assignments remain which cannot be rejected: No 8 and 14; they differ by an interchange of the components  $a$  and  $d$  which are expected to be of equal strength and thus indistinguishable. The corresponding  $A$  factors (on atomic frequency level) are:

No 8:  $A_l = -2127.2(6)$  MHz,  $A_u = -533.0(6)$  MHz,  $A_u/A_l = 0.2506(4) \approx 1/4$ .

No 14:  $A_l = 533.0(6)$  MHz,  $A_u = 2127.2(6)$  MHz,  $A_u/A_l = 3.991(6) \approx 4$

(the error values given here are estimated by the fit of the data as listed in the second column of Table 6.1, i.e. they include the standard deviations only). Since the upper level of the transition belongs to a configuration with an unpaired  $s$ -electron, in contrast to the lower level, it is most likely that the upper level has the larger  $A$  factor because of its contact contribution. Therefore the assignment 14 is favored at this stage. A final proof follows from the analysis of  $^{207}\text{Po}$ .

c)  $^{207}\text{Po}$

The spectrum of  $^{207}\text{Po}$  is more complicated: it consists of  $n = 13$  components,  $r = 11$  of them were observed. Thus the number of possible assignments is  $13! / 2! = 3.1 \cdot 10^9$ . For this large number the combinatorial procedure described above cannot be applied directly because of too long a computing time required.

The number of assignments is considerably reduced if additional existing information is used beforehand:

- two components:  $F_l = 3/2 \rightarrow F_u = 1/2$  and  $F_l = 1/2 \rightarrow F_u = 1/2$  are separated by only 38 MHz, as follows from the ABMR measurements in the ground state [OAL 61]; these cannot be expected to be resolved within the observed linewidth,
- one of the components has a relative intensity of 0.5 (where the strongest is normalized to 100) and thus is not expected to be observed; anyway, it lies also only 38 MHz away from the neighboring one.

It follows that not more than 11 components are expected to be observed; since 11 have been found on the spectrum, one can conclude that no further coincidences occur. Therefore the actual number of assignments is  $11! = 4 \cdot 10^7$ . Even with this reduced number a direct use of a combinatorial way to assign the components observed in the spectrum would be too time consuming. Instead we first made use of additional information already available:

- two possible ratios  $A_u/A_l$  are known from  $^{209}\text{Po}$ , at least with an accuracy of a few % accounting for the experimental error and a possible hyperfine anomaly [Bü 84],
- $A_l$  and  $B_l$  are known from the atomic beam magnetic resonance (ABMR) measurements [OAL 61].

The first step of our procedure was to find realistic errors for our frequency data. For this purpose frequency differences for all pairs of observed components were calculated as 8 of them are expected to correspond directly to ground state splittings. If all 13 components were observed, this number would increase to 11: each of the 4 possible energy differences  $F_l \rightarrow F_u = F_l + 1$  with  $F_l = 1/2, 3/2, 5/2, 7/2$ , occurs twice and each of the 3 energy differences  $F_l \rightarrow F_u = F_l + 2$  with  $F_l = 1/2, 3/2, 5/2$ , occurs once; the smallest energy difference ( $F_l = 1/2 \rightarrow F_l = 3/2$ ) cannot be resolved and the second lowest one ( $F_l = 3/2 \rightarrow F_l = 5/2$ ) involves in one of the cases the unobserved component with a relative intensity of only 0.5. Thus a total of  $(8 - 2) + (3 - 1) = 8$  known differences should be found in the spectra. We found that indeed 8 of the observed frequency differences were close to the expected ones (Table 6.4). The discrepancies, however (last column in Table 6.4), exceeded the errors as determined by the profile fit program (second column in Table 6.4, in parenthesis).

Thus we conclude that these uncertainties are underestimates of the actual errors, and the systematic frequency scale errors are the important ones. In order to be able to perform later on realistic  $\chi^2$ -tests with our data, we have scaled up the errors to  $\pm 4$  MHz throughout for all frequencies such that the discrepancies were made to vanish. For a comprehensive concluding discussion of the experimental errors see Chapter 7 (Section 7.1, p. 61).

Table 6.4 Frequency differences  $\Delta v^{meas}_{laser}$  between components in the spectrum of  $^{207}\text{Po}$ , corresponding to the ground state splittings; the expected values  $\Delta v^{ABMR}/2$  according to the ABMR measurements [OAL 61]. In column 4 the differences between the two measurements are given; in parenthesis (unrealistic) errors originating from the curve fitting program are given. Because the difference clearly is larger than these errors, the uncertainties were scaled up to  $\pm 4$  MHz throughout.

involved components	$\Delta v^{meas}_{laser}$ [MHz]	$\Delta v^{ABMR}/2$ [MHz]	$\Delta v^{meas}_{laser} - \Delta v^{ABMR}/2$ [MHz]
207g - 207h	76.1(2.0)	79.3	-3.2(2.0)
207c - 207e	95.4(1.8)	98.3	-2.9(1.8)
207f - 207g	209.6(1.9)	210.9	-1.3(1.9)
207j - 207k	213.1(1.1)	210.9	+2.2(1.1)
207f - 207h	285.7(1.3)	290.2	-5.5(1.3)
207l - 207m	440.3(1.6)	442.4	-2.1(1.6)
207i - 207j	442.8(1.5)	442.4	+0.4(1.5)
207i - 207k	655.9(1.6)	653.3	+2.6(1.6)

The further procedure was as follows. For both cases:  $A_u/A_l \approx 4$  and  $A_u/A_l \approx 1/4$  model spectra were calculated;  $B_l$  was taken from [OAL 61], and  $B_u$  was allowed to vary. Fig.6.2 shows the dependence of the arrangement of the components on the value of  $B_u/B_l$ .

These model spectra were compared to the actually observed ones. It can be seen that for  $|B_u| > 17 \cdot B_l$  the model spectra for both possible  $A_u/A_l$  ratios are definitely broader than the spectrum actually observed, whose total width amounts to  $\bar{w} = 6002.3(4.5)$  MHz (see Fig.5.3), determined as mean value from 4 scans. The error estimate quoted here is the standard deviation of the mean value  $s_{\bar{w}}$ , as used for statistical test purposes only.

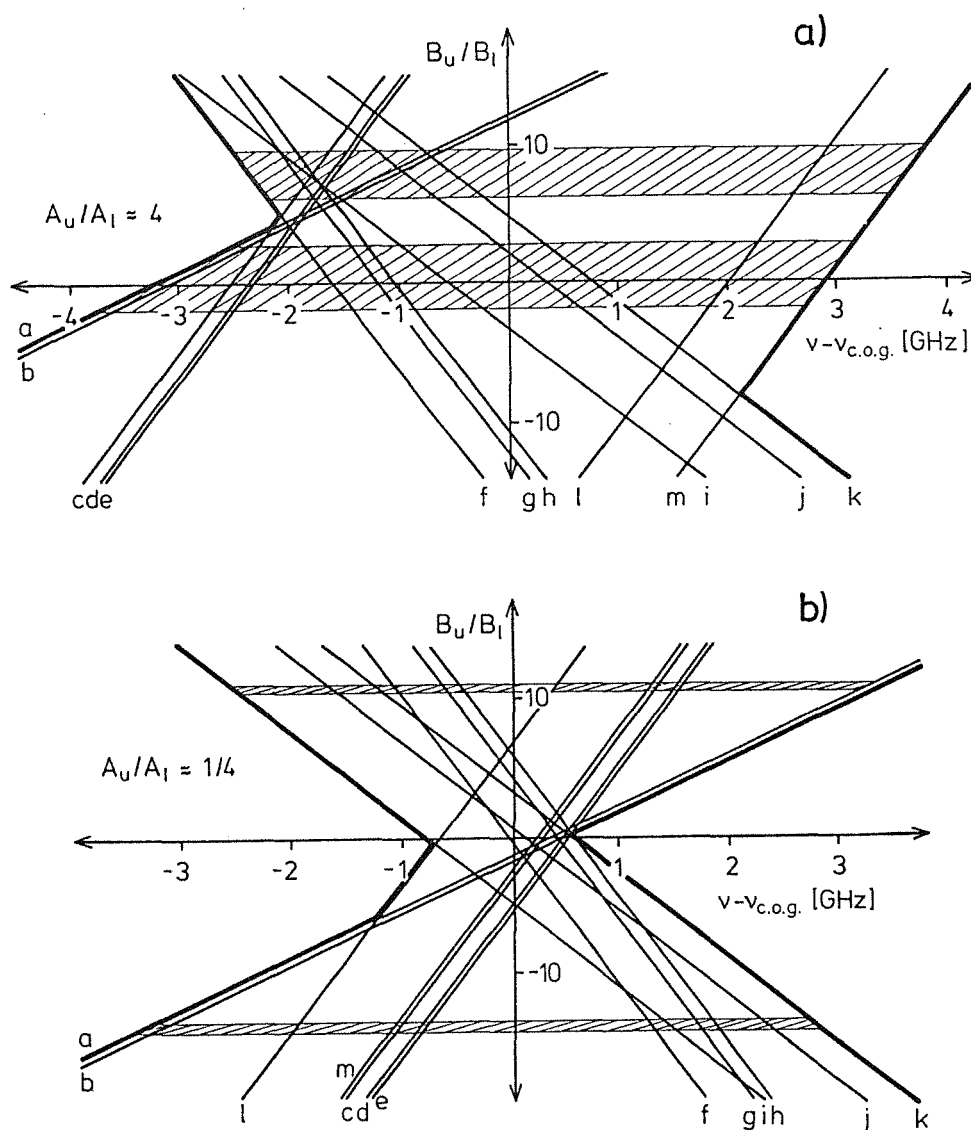


Fig. 6.2 Dependence of the possible arrangement of the components on  $B_u$  for both possible  $A_u/A_l$  ratios: a) 3.991 and b) 0.2506. Values of  $A_l$  and  $B_l$  are taken from [OAL 61]. The ranges of  $B_u/B_l$  corresponding to the 99.9% confidence interval for the total width of the measured spectrum.(see text) are marked.

The calculated spectrum width is found approximately equal to the observed one in two  $B_u$  ranges of values for each  $A_u/A_l$  ratio. The 99.9% confidence interval for the spectrum width was calculated to be:  $\bar{w} \pm t_{n-1=3; \alpha=0.001} \cdot s_{\bar{w}} = 6002 \pm 59$  MHz. The corresponding possible ranges for  $B_u$  were calculated. Because of the neglect of a possible hyperfine anomaly in the estimate of the possible ranges for  $B_u$  a 5% tolerance for the  $A_u/A_l$  ratio was allowed for. All  $B_u$  values leading to a spectrum width outside the 99.9% confidence interval were rejected. For the remaining  $B_u$  values the number of possible assignments is considerably reduced to a total of 15 arrange-

ments, 12 of them belong to  $A_u/A_l \approx 4$ ,  $6.65 < B_u/B_l < 9.61$  (Fig. 6.2a upper band). Each observed component was assigned to one hyperfine transition, whereby the sequence was maintained (see Figs 6.3 and 6.4).

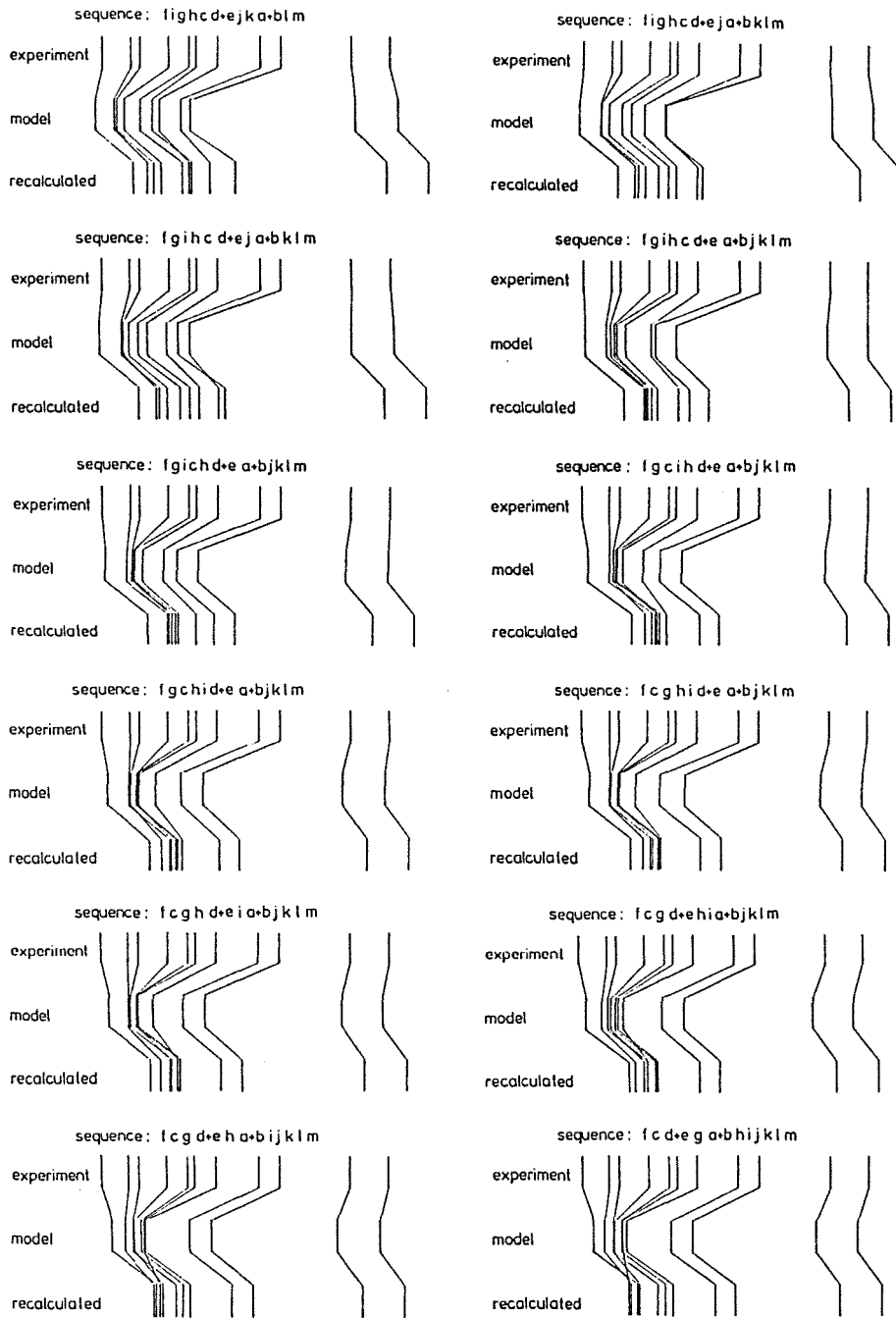
In the next step all of the 15 assignments were least-squares fitted with restrictions on  $A_l$ ,  $B_l$  and  $A_u/A_l$  so that actually the only remaining parameters to be fitted without any restrictions were  $B_u$  and the center of gravity.  $A_l$  and  $B_l$  were considered error-free as the errors given in [OAL 61] are negligible compared to our measurements.  $A_u/A_l$  again was varied within limits of  $\pm 5\%$  to allow for the neglect of a hyperfine anomaly; for each of the 15 assignments the  $A_u/A_l$  was searched, for which the test parameter  $M$  had the minimum value ( $M_{min}$ ). The assignments with their respective  $M_{min}$  values are listed in Table 6.5. For one of the assignments a reasonably low  $M_{min} = 4.3$  was found for  $A_u/A_l$  exceeding that one of  $^{209}\text{Po}$  by  $\sim 1.3\%$  (see below). For all the remaining 14 assignments the  $M_{min}$  values were very high - in the  $10^5 - 10^6$  range. Figs 6.3 and 6.4 also present the results of the least-squares fits of each of the 15 possible assignments compared to the observed pattern. It is obvious that the one for  $A_u/A_l \approx 4$ ,  $-1.70 < B_u/B_l < 2.88$  (Fig. 6.2a, lower band) is the correct one.

In more detail, the possible ranges for the parameter  $B_u$  (marked in Fig. 6.2) are as follows:

- 1)  $A_u/A_l \approx 4$ 
  - for the range  $6.65 < B_u/B_l < 9.61$  there are 12 assignments possible; all of them can be rejected by a  $\chi^2$ -test ( $M_{min} \sim 10^5$  for  $11 - 3 = 8$  degrees of freedom, i.e. almost vanishing  $\alpha$ ); all these assignments are obviously absurd, which is clear from Fig. 6.3;
  - for the range  $-1.70 < B_u/B_l < 2.88$  the assignment of the components is unique; the resulting  $M_{min}$  value of 4.3 doesn't allow rejection of this assignment unless we risked an error probability of  $\sim 35\%$ ;
- 2)  $A_u/A_l \approx 1/4$ 
  - for each of the ranges:  $10.95_l < B_u/B_l < 11.29$  and  $-13.95 < B_u/B_l < -13.61$  the assignments are unique; in both cases they can be safely rejected as absurd ( $M_{min} \sim 10^6$ ).

Thus we conclude that  $A_u/A_l \approx 4$ , and the only possible assignment is that one valid for the range  $-1.70 < B_u/B_l < 2.88$ . For this assignment 9 well resolved components (excluding the unresolved line containing the components  $a$  and  $b$  and the component  $i$  which coincides with the line of  $^{206}\text{Po}$ , see Fig. 5.3) were used to calculate the definite  $A_u$  and  $B_u$  values (see Table 7.3). The obtained ratios of the  $A$  and  $B$  factors are:

$$A_U/A_I = 4 \quad 6.65 < B_U/B_I < 9.61$$



$$A_U/A_I = 4 \quad -1.70 < B_U/B_I < 2.88$$

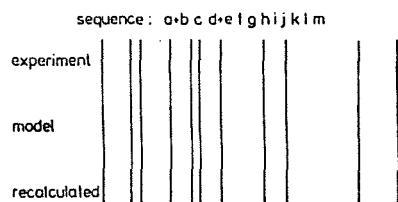


Fig.6.3 Possible assignments of the 11 components in the spectrum of  $^{207}\text{Po}$  for the ratio  $A_U/A_I \approx 4$ .

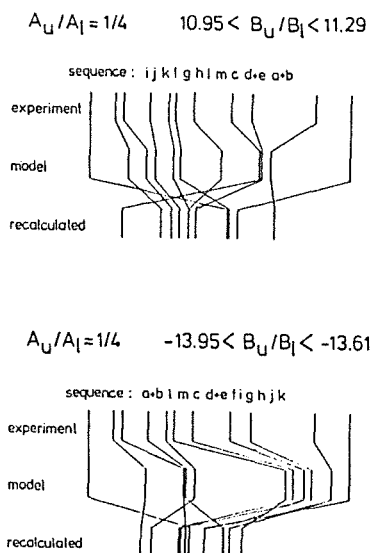


Fig.6.4 Possible assignments of the 11 components in the spectrum of  $^{207}\text{Po}$  for the ratio  $A_U/A_I \approx 1/4$ .

Table 6.5 The 15 possible assignments of the 11 components observed in the spectrum of  $^{207}\text{Po}$  and their respective values of the test quantity  $M_{min}$ .

No	sequence	$M_{min}$
1	<i>f i g h c d + e j k a + b l m</i>	$1.6 \cdot 10^6$
2	<i>f i g h c d + e j a + b k l m</i>	$1.7 \cdot 10^6$
3	<i>f g i h c d + e j a + b k l m</i>	$1.7 \cdot 10^6$
4	<i>f g i h c d + e a + b j k l m</i>	$1.3 \cdot 10^6$
5	<i>f g i c h d + e a + b j k l m</i>	$1.3 \cdot 10^6$
6	<i>f g c i h d + e a + b j k l m</i>	$1.2 \cdot 10^6$
7	<i>f g c h i d + e a + b j k l m</i>	$1.2 \cdot 10^6$
8	<i>f c g h i d + e a + b j k l m</i>	$1.0 \cdot 10^6$
9	<i>f c g h d + e i a + b j k l m</i>	$0.9 \cdot 10^6$
10	<i>f c g d + e h i a + b j k l m</i>	$0.9 \cdot 10^6$
11	<i>f c g d + e h a + b i j k l m</i>	$0.8 \cdot 10^6$
12	<i>f c d + e g h a + b i j k l m</i>	$0.8 \cdot 10^6$
13	<i>a + b c d + e f g h i j k l m</i>	4.3
14	<i>i j k f g h l m c d + e a + b</i>	$2.7 \cdot 10^4$
15	<i>a + b l m c d + e f i g h j k</i>	$0.6 \cdot 10^5$

$$A_u/A_l(^{207}\text{Po}) = 4.042(8)$$

$$B_u/B_l(^{207}\text{Po}) = 0.964(19);$$

The errors of the ratios given here result from those of the  $A$  and  $B$  values, given in Table 7.3; for comparison, the final result for  $^{209}\text{Po}$  is:

$$A_u/A_l(^{209}\text{Po}) = 3.991(28).$$

d)  $^{205}\text{Po}$

The case of  $^{205}\text{Po}$  is analogous to that of  $^{207}\text{Po}$  since  $I$  is the same. The  $A_l$  and  $B_l$  values, known to good accuracy, are as follows [OAL 61]:

$$A_l(^{205}\text{Po}) = 134.64(44) \text{ MHz} = 0.9648(32) \cdot A_l(^{207}\text{Po})$$

$$B_l(^{205}\text{Po}) = 229.2(4.8) \text{ MHz} = 0.602(13) \cdot B_l(^{207}\text{Po}).$$

Both ratios:  $A_u/A_l$  and  $B_u/B_l$  are expected, to within a few % (accounting for the experimental error and the neglect of a possible hyperfine anomaly), to be equal to those of  $^{207}\text{Po}$ . The sequence of the components proves to remain unchanged as compared to  $^{207}\text{Po}$  if model spectra for  $^{205}\text{Po}$  are calculated with independent variations of  $\pm 5\%$  for  $A_u/A_l$  and  $\pm 10\%$  for  $B_u/B_l$ . From those parameters a model spectrum was calculated (Fig. 6.5).

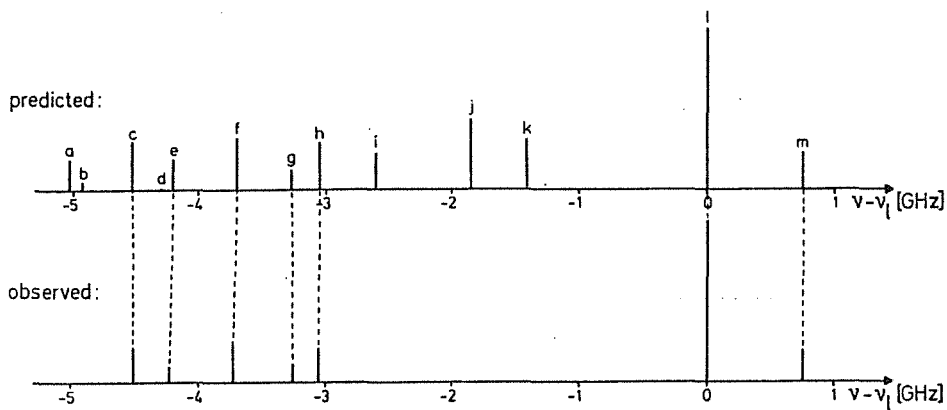


Fig.6.5 Observed fragments of the spectrum of  $^{205}\text{Po}$  compared to the expected pattern. For the original data, see Fig. 5.2.

We were able to observe only fragments of the spectrum of  $^{205}\text{Po}$  containing 7 resolved components out of 11 (Fig. 5.2). These could be assigned by matching its pattern to the model spectrum (see Fig.6.5). There were only two independent frequency differences between the components involving  $A_u$  and  $B_u$ :  $\nu(c-f)$  and  $\nu(f-l)$ , and these were used to determine the two upper state splitting parameters. The absolute values are given in Table 7.3, the ratios being:

$$A_u/A_l(^{205}\text{Po}) = 4.026(28)$$

$$B_u/B_l(^{205}\text{Po}) = 1.051(81).$$

## 7 Results

### 7.1 Measured isotope shifts and HFS factors

The isotope shifts in the chosen atomic transition  $6p^4\ ^3P_2 \rightarrow 6p^37s\ ^5S_2$  ( $\lambda = 255.8$  nm) for the studied series of polonium isotopes ( $^{200}\text{Po}$ ,  $^{202}\text{Po}$  and  $^{204-210}\text{Po}$ ) are presented in Table 7.2. As reference the position of the spectral line of  $^{208}\text{Po}$  was taken.

#### a) Total experimental errors

The total experimental errors for each component cannot be simply calculated from the scattering of the data; they depend not only on the quality of the Lorentz fit of the spectra and on the scattering of the center frequencies determined in this way. The limited accuracy of our frequency axis and possible additional uncertainties have to be taken into account.

In some cases it was possible, however, to "measure" the errors directly as discrepancies, by comparison with available accurate values of certain frequency differences (obtained by the ABMR method). The application of this method to case of  $^{207}\text{Po}$  has already been discussed in Chapter 6 (Section 6.3, p. 54): the definite realistic estimate of our experimental errors for  $^{207}\text{Po}$ , obtained in this way, was  $\pm 4$  MHz.

For  $^{205}\text{Po}$  one frequency difference in the ground state, known from the ABMR measurements, was remeasured; the discrepancy amounted to  $-2.4$  MHz (Table 7.1).

Another estimate of the total experimental errors is provided by checking the internal consistency of our data, i.e. of equal frequency differences (in the excited state) measured in various ways; this applies to both  $^{207}\text{Po}$  and  $^{209}\text{Po}$  (see Table 7.1).

A special case is  $^{205}\text{Po}$ , where the spacing 205l - 206 was measured twice and the two values proved to be inconsistent with each other (see also Table 7.1); this is in contrast to other cases, where the repeated measurements gave consistent results.

In order to have an additional check of the accuracy of frequency measurements with our wavemeter, HFS measurements in cobalt were performed [SKK 91], where also a comparison with ABMR data was possible; our values were found to deviate from the ABMR values by not more than  $\pm 6$  MHz on laser frequency level, the average discrepancy being  $\pm 3$  MHz.

Altogether we concluded that  $\pm 4$  MHz (on the laser frequency level) is a realistic and dependable estimate of the total experimental error for spacings between two Po resonances, and used it further for all the measured spacings, except for the rare cases where either of the components involved was poorly resolved and therefore was given an extra error. The above discussed error estimates of  $\pm 4$  MHz are treated as if they were of statistical nature, i.e. as if they corresponded to standard deviations.

Table7.1 Frequency differences between components in the spectra of odd-mass polonium isotopes, used to obtain realistic estimates of the experimental errors; whenever possible, comparison with ABMR data was made (column 4), otherwise the internal consistency of our data (column 5) is checked (see text). A special case is  $^{205}\text{Po}$ , where we have determined the frequency difference 205l - 206 twice and found the two values to differ from each other by much more than a standard deviation.

involved components	$\Delta_{\nu}^{meas}$ [MHz]	$\Delta_{\nu}^{ABMR} / 2$ [MHz]	$\frac{\Delta_{\nu}^{meas} - \Delta_{\nu}^{ABMR}}{2}$ [MHz]	discrepancy in $\Delta_{\nu}^{meas}$ [MHz]
209a - 209b 209c - 209d	666.7(1.0) 665.5(1.0)			1.2(1.4)
209a - 209c 209b - 209d	2659.6(0.9) 2658.1(1.4)			1.5(1.7)
207g - 207h 207c - 207e	76.1(2.0) 95.4(1.8)	79.302(0.007) 98.342(0.012)	-3.2(2.0) -2.9(1.8)	
207f - 207g 207j - 207k	209.6(1.9) 213.1(1.1)	210.916(0.005) 210.916(0.005)	-1.3(1.9) +2.2(1.1)	3.5(2.2)
207f - 207h 207l - 207m 207i - 207j	285.7(1.3) 440.3(1.6) 442.8(1.5)	290.218(0.012) 442.425(0.010) 442.425(0.010)	-5.5(1.3) -2.1(1.6) +0.4(1.5)	2.5(2.2)
207i - 207k 207f - 207j 207g - 207k	655.9(1.6) 953.0(1.1) 956.7(1.9)	653.341(0.012)	+2.6(1.6)	3.7(2.2)
207i - 207l 207j - 207m	1396.7(1.5) 1394.2(1.6)			2.5(2.2)
205l - 205m 205l - 206 205l - 206	377.9(1.4) 179.7(0.5) 177.0(0.6)	380.3 (1.9)	-2.4(2.4)	2.7(0.8)

In the case of even-mass isotopes the isotope shifts were measured directly as spacings between the single spectral components, and thus the respective errors amount to  $2 \cdot (\pm 4 \text{ MHz}) = \pm 8 \text{ MHz}$  on the atomic frequency level. In the case of the odd-mass isotopes the center of gravity of the spectral components was first determined together with the  $A$  and  $B$  factors of the excited state; for  $^{207}\text{Po}$  and  $^{209}\text{Po}$  these were determined from a redundant set of linear equations, where the positions of the components and not the spacings between them were required by the fitting program used; the errors of either of the component positions were assumed to amount to  $\pm 2.8 \text{ MHz}$  (on laser frequency level) so that the errors of frequency differences were  $\pm 4 \text{ MHz}$ . The resulting error of the center of gravity proved to be smaller than the errors of the positions of each component separately (see column 3 of Table 7.2, in parenthesis) since we have more equations than unknowns; this applies to  $^{209}\text{Po}$  and  $^{207}\text{Po}$ .

b) Results

The even-mass isotopes  $^{210}\text{Po}$  and  $^{206}\text{Po}$  were measured against the reference isotope  $^{208}\text{Po}$  directly since both isotopes were simultaneously present in the sample (thus the errors assigned to the corresponding isotope shifts amount to 8 MHz). The three even-mass isotopes:  $^{200}, ^{202}, ^{204}\text{Po}$  were measured indirectly, in two or three steps:  $^{200} - ^{202} - ^{206} - ^{208}\text{Po}$ ,  $^{204} - ^{206} - ^{208}\text{Po}$ , the resulting errors were calculated by square summing.

Table 7.2 Isotope shifts for Po in the transition  $6p^4^3P_2 \rightarrow 6p^37s^5S_2$  ( $\lambda = 255.8 \text{ nm}$ ).

mass number	nuclear spin	isotope shift $\nu^A - \nu^{208}$ [MHz]
210	0	+ 3464( 8)
209	1/2	+ 1295( 7)
208	0	0
207	5/2	- 2306( 6)
206	0	- 3064( 8)
205	5/2	- 5457(16)
204	0	- 6077(12)
202	0	- 8852(12)
200	0	- 11154(20)

For the measured odd-mass isotopes the center of gravity and the hyperfine splitting  $A$  and  $B$  factors have been determined. For  $^{205}\text{Po}$  and  $^{207}\text{Po}$  the hyperfine splittings of the ground state are known from atomic beam magnetic resonance (ABMR) measurements [OAL 61] and thus with higher accuracy than our optical measurements allow. Therefore we first checked the consistency of our data, comparing the frequency changes corresponding to the ground state splittings with the results from [OAL 61]. In the case of  $^{207}\text{Po}$  first the survey spectrum (Fig. 5.3) was fitted with constraints on  $A_l$  and  $B_l$  to obtain  $A_u, B_u$  and the center of gravity (see Section 6.3) and then the same parameters were determined from the more precise spectrum, containing only selected components (Fig. 5.4b). Both sets of parameters proved to be in good agreement with each other. In the case of  $^{205}\text{Po}$   $A_u, B_u$  and the center of gravity were determined only from the frequency differences between the selected components ( $c, f,$  and  $l$ , see Fig.6.3) because no survey spectrum could be taken with reasonable accuracy since only too small sample sizes were available. The HFS factors determined from our measurements and the available data of other authors are listed in Table 7.3.

Table 7.3 HFS constants for odd-mass Po isotopes.

level	$6p^4^3P_2$		$6p^37s^5S_2$		reference
mass number	$A$ [MHz]	$B$ [MHz]	$A$ [MHz]	$B$ [MHz]	
205	134.64 (44)	229.2 (4.8)	542(2)	241(13)	this work [OAL 61]
207	139.551(2)	380.548(16)	564(1)	367( 7)	this work [OAL 61]
209	533(3) 300	—	2127(3) 2020	—	this work [Ch 66]

## 7.2 Mean square charge radii

### a) Global features

Isotope shifts in atomic spectra result from the influence of a nucleus on the electronic energy levels, varying from one level to another. Thus various energy changes of the levels result in corresponding energy changes in atomic transitions. The total shift is a superposition of two effects:

- a) mass shift (MS) - a change of the mass of the nucleus upon addition of neutrons leads to such an energy change of an electronic level that the angular momentum of an electron in this level remains constant (as required by quantum mechanics);
- b) field shift (FS) - the energy of a level is dependent on the charge distribution in the nucleus (and thus on the size and shape of the nucleus);

$$IS^{AA'} = MS^{AA'} + FS^{AA'} , \quad (7.1)$$

where  $A$  and  $A'$  are the mass numbers of the two isotopes involved. The mass shift in turn consists of two contributions:

- normal mass shift (NMS), resulting from the interaction of the individual electrons with the nucleus:

$$NMS^{AA'} \sim \sum_i p_i^2 , \quad (7.2a)$$

- specific mass shift (SMS), accounting for motional correlation effects between the electrons:

$$SMS^{AA'} \sim \sum_{i>j} p_i \cdot p_j ; \quad (7.2b)$$

$p_i$  and  $p_j$  denote the momenta of the electrons in an atom with an infinitely heavy nucleus. The same relations apply, of course, to the shifts in atomic transitions which are directly measurable.

Through most of the periodic table the NMS and the SMS have opposite signs, i.e. the electron momenta tend to cancel each other because of correlations between them.

The NMS is the dominating effect in the spectra of light elements; for heavy elements (like Po) it is normally negligible compared to the field shift. It can be easily calculated from the formula:

$$\delta v^{AA'} = m \frac{A - A'}{A \cdot A'} v^A . \quad (7.3)$$

In the transition studied the NMS amounts to  $\sim 30$  MHz for  $\Delta N = 2$ . As the total isotope shifts for  $\Delta N = 2$  are of the order of 3000 MHz (see Table 7.1), the NMS contribution is only 1%.

The SMS cannot be determined as straightforward as the NMS because the correlation between the electrons cannot be evaluated directly (many-body problem).

For certain types of transitions (e.g. s-p, s<sup>2</sup>-sp) theoretical estimates are possible [HS 74, AHS 87]. Provided that both field and mass shifts in a muonic, electronic X-ray or another optical transition have been determined, an alternative method of evaluation of the SMS (and simultaneously also the FS) in a particular transition is the so-called King plot [Ki 84, Chapter 6].

In our case unfortunately no reliable estimate of the SMS can be made since theoretical calculations in the case of a p<sup>4</sup> - p<sup>3</sup>s transition are not available. There are also no other Po isotope shift data for more than one isotope pair available besides ours. The only available data are those of Charles [Ch 66], who studied isotope shifts for the isotope pair <sup>208-209</sup>Po in a number of transitions by classical optical spectroscopy. The data are not very accurate and, concerning only one isotope pair, are of no use as far as a possible calibration of our data is concerned (no King plot can be constructed). It can be assumed, however, that the SMS is small, since in most cases in heavy elements where it can be estimated, the SMS does not exceed 10·NMS (usually being of the order of 1·NMS). Therefore, following the usual procedure, we ignored it in the further analysis and assumed that the total observed isotope shifts are the field shifts; the contribution of the mass effect is accounted for by increasing the errors to 10·NMS.

The field shift is dependent on the change in the mean square radius of the nuclear charge distribution from one isotope to another. It can be expressed as follows:

$$FS^{AA'} = F \cdot \lambda \quad , \quad (7.4)$$

where  $F$  is an electronic factor and  $\lambda$  a nuclear factor. The electronic factor is proportional to the difference of the total electron density at the nucleus between the upper and the lower level of a transition,  $\Delta|\Psi(0)|^2$ . For alkali-like s-p transitions  $\Delta|\Psi(0)|^2$  can be estimated either from ab initio calculations or from the experimental data, using the semi-empirical Goudsmit-Fermi-Segré formula or the formula relating  $|\Psi(0)|^2$  for an s-electron to the hyperfine structure. Unfortunately, for other types of transitions neither of the methods is reliable and then the only alternative method of obtaining the electronic factor is from a King plot.

The nuclear factor  $\lambda$  can be expressed as:

$$\lambda = \delta \langle r^2 \rangle^{AA'} + \frac{C_2}{C_1} \delta \langle r^4 \rangle^{AA'} + \frac{C_3}{C_1} \delta \langle r^6 \rangle + \dots = K \delta \langle r^2 \rangle \quad . \quad (7.5)$$

The coefficients  $C_i$  are known as Seltzer's coefficients; they can either be obtained from the isotope shifts in X-ray spectra or calculated theoretically [Se 69, BBP 87]. The ratios  $\delta \langle r^n \rangle / \delta \langle r^2 \rangle$  can be evaluated e.g. within the framework of the spherical droplet model (SDM) [MS 69, MS 83] and thus the factor  $K$  can be

calculated. Values of  $K$  are only slightly less than 1 which means that the main contribution to the field shift comes from the change in  $\langle r^2 \rangle$  (e.g. for Pb,  $Z=82$ ;  $K=0.93$  [TAB 83]; for Po the same value of  $K$  is obtained).

In contrast to the factor  $K$  in (7.5), the electronic factor  $F$  for the considered transition in Po cannot be estimated so far because of the lack of data. Therefore, until the Hartree-Fock calculations (which are in progress [Fr 90]) are not yet available, we decided to make a preliminary scaling, based on the spherical droplet model [MS 69, MS 83]; this model is known to describe well the experimental  $\delta\langle r^2 \rangle$  below the neutron shell closure at  $N=126$ , e.g. in Pb [AFG 86]. In the present case it has been assumed that

$$\langle r^2 \rangle^{206} - \langle r^2 \rangle^{208} : = \delta\langle r^2 \rangle^{206,208} \equiv \delta\langle r^2 \rangle_{SDM}^{206,208} = -0.104 \text{ fm}^2 .$$

Using this scaling, further  $\delta\langle r^2 \rangle$  were calculated; the values are compiled in Table 7.4.

**Table 7.4** Changes of the mean square charge radii in Po; the values are obtained using the following scaling:

$$\delta\langle r^2 \rangle^{206,208} \equiv \delta\langle r^2 \rangle_{SDM}^{206,208} = -0.104 \text{ fm}^2 \text{ [MS 83]}.$$

mass number	$\delta\langle r^2 \rangle^{A,208} \text{ [fm}^2\text{]}$
210	0.118(3)
209	0.044(4)
208	0
207	-0.078(5)
206	-0.104(1) *
205	-0.185(6)
204	-0.206(2)
202	-0.300(3)
200	-0.379(7)

\* by definition

Error values consist of two contributions: experimental errors concerning the isotope shifts (Table 7.1) and the errors resulting from the neglect of the mass shifts (assumed to be 10·NMS, i.e. 150 MHz for the difference of mass numbers  $\Delta A=1$ ).

b) Odd-even staggering

An interesting feature of the field shifts is the so-called odd-even staggering. For normal odd-even staggering the  $\langle r^2 \rangle$  of an odd-N nucleus is smaller than the mean value of  $\langle r^2 \rangle$  of its both even-N neighbors. This effect can be characterized by a staggering parameter  $\gamma$ :

$$\gamma = 2 \frac{\langle r^2 \rangle^A - \langle r^2 \rangle^{A-1}}{\langle r^2 \rangle^{A+1} - \langle r^2 \rangle^{A-1}}, \quad (7.6a)$$

which describes the effect in relative terms, or  $\Delta$  [ABH 86].:

$$\Delta = \langle r^2 \rangle^A - \frac{1}{2} (\langle r^2 \rangle^{A-1} + \langle r^2 \rangle^{A+1}); \quad (7.6b)$$

in the absence of staggering,  $\gamma = 1$  and  $\Delta = 0 \text{ fm}^2$ . The staggering parameter  $\gamma$  can be calculated also from the isotope shifts provided the total mass shift can be reasonably estimated; if this is not the case, the neglect of the mass shift has to be accounted for by an adequately chosen uncertainty.

The odd-even staggering parameters  $\gamma$  and  $\Delta$  for the measured odd-mass polonium isotopes, calculated using the isotope shift values from Table 7.2 and the scaling for  $\delta \langle r^2 \rangle$  as described in Section 7.2, are listed in Table 7.5. In contrast to the errors of  $\delta \langle r^2 \rangle$  values listed in Table 7.4, which allow for both possible signs of the neglected mass shift and are therefore not independent, the errors of  $\gamma$  and  $\Delta$ , as listed in Table 7.5, account for either possible sign of the mass shift separately and are independent. The error values listed correspond to the "worst case" for  $\gamma$  (i.e. maximum and minimum possible  $\gamma$ ), while in the case of  $\Delta$  the contributions from the mass shift cancel totally to good approximation (as can be seen from formula (7.6b), mass shift being almost independent of the neutron number) and thus only the experimental errors concerning the isotope shift contribute.

Table 7.5 Values of the odd-even staggering parameters  $\gamma$  and  $\Delta$  for the measured odd-mass polonium isotopes.

mass number	$\gamma$	$\Delta$ [fm <sup>2</sup> ]
209	0.75(3)	-0.0148(4)
207	0.49(7)	-0.0263(4)
205	0.41(9)	-0.0301(4)

Beside the "normal" effect, described above, there are also cases of inverted staggering (e.g. the Pt-Hg and the Ra-Th regions), sometimes even very strong (Pt-Hg region). This is attributed to the special deformation effects (in the Ra-Th region to the permanent octupole deformation [CCT 85, CCT 87, WAK 87, AKN 88, Kä 88], in the Pt-Hg region to the prolate-oblate instability along the isotope chain [BHK 76, UBD 86, DSB 86, WBB 87] ). In polonium normal odd-even staggering is observed.

### 7.3 Hyperfine structure and nuclear moments

The hyperfine structure is another result of the influence of a nucleus on the electronic energy levels. The interaction of the electromagnetic moments of a nucleus with the electromagnetic fields of an electron shell is quantized: the nuclear spin  $I$  and the electron shell angular momentum  $J$  are coupled to a quantum number  $F = |I - J|, \dots, I + J$  which results in the splitting of the electronic levels into  $2I + 1$  (or  $2J + 1$ , whichever value is smaller) sublevels.

Of all the electromagnetic  $2^k$ -pole moments of a nucleus only the even- $k$  electric and the odd- $k$  magnetic moments are non-zero (this can be shown on the basis of parity considerations). Of these practically only the magnetic dipole ( $k=1$ ) and electric quadrupole ( $k=2$ ) moments have a significant influence on the electronic energy levels, all the higher moments can be in most cases neglected. The energy shift of a particular hyperfine sublevel with respect to an unperturbed level (i.e. the center of gravity of a hyperfine multiplet) can be then expressed as follows:

$$E_F = E_J + A \cdot \frac{K}{2} + B \frac{\frac{3}{4}K(K+1) - I(I+1)J(J+1)}{2IJ(2I-1)(2J-1)}, \quad (7.7)$$

where  $K = F(F+1) - I(I+1) - J(J+1)$ . Energy differences between the HFS sublevels are of the order of 1 MHz - 1 GHz. The hyperfine splitting  $A$  and  $B$  factors describe the magnetic dipole and electric quadrupole interactions, respectively. They are defined as follows:

$$A = \frac{\mu_I \cdot H(0)}{IJ}, \quad (7.8a)$$

$$B = eQ \phi_{zz}(0), \quad (7.8b)$$

where  $\mu_I$  and  $Q$  are the magnetic dipole and the electric quadrupole moments, respectively,  $H(0)$  is the magnetic field of the electron shell at the place of the nucleus and  $\phi_{zz}(0)$  is the gradient of the electric field.

For two of the measured odd-mass polonium isotopes the magnetic dipole moments were measured by the nuclear magnetic resonance on oriented nuclei (NMR-ON):  $^{205}\text{Po}$  and  $^{207}\text{Po}$  [HWF 83]. The values are:  $\mu_I(^{205}\text{Po})=0.760(55)$  n.m. and  $\mu_I(^{207}\text{Po})=0.793(55)$  n.m., the latter measured directly and the former derived from the ratio  $g_I(^{205}\text{Po})/g_I(^{207}\text{Po})=0.960(2)$  (the error is thus also transferred). We have used the  $\mu_I(^{207}\text{Po})$  value to calculate the magnetic dipole moment of  $^{209}\text{Po}$ ; the value obtained is

$$\mu_I(^{209}\text{Po}) = \mu_I(^{207}\text{Po}) \cdot \frac{A_I(^{209}\text{Po})}{A_I(^{207}\text{Po})} \cdot \frac{I(^{209}\text{Po})}{I(^{207}\text{Po})} = 0.606(50) \text{ n.m.}$$

The error given accounts also for the neglect of a possible hyperfine anomaly ( $\pm 5\%$  tolerance for the ratio  $A_I(^{209}\text{Po})/A_I(^{207}\text{Po})$  has been assumed).

As for the electric quadrupole moments, there are no direct measurements available so far. Theoretical estimates of the relation between  $Q$  and  $B$  for the ground state of the Po atom were performed by Olsmats et al. [OAL 61], using Breit and Wills theory of the HFS; these, combined with their experimental  $B$  values, led to:  $Q(^{205}\text{Po})=0.17$  barn and  $Q(^{207}\text{Po})=0.28$  barn. The  $B$  value for  $^{207}\text{Po}$  [OAL 61] was also used by other authors [LR 74] to re-evaluate the electric quadrupole moment by use of the relativistic Hartree-Fock (HF) and optimized Hartree-Fock-Slater (OHFS) methods; the corresponding values are:  $Q(^{207}\text{Po})=0.29$  barn (HF) and  $Q(^{207}\text{Po})=0.28$  barn (OHFS) [LR 74, p.247], in agreement with the value from [OAL 61], quoted above. Therefore the estimates of  $Q(^{205}\text{Po})$  and  $Q(^{207}\text{Po})$  from [OAL 61] can be assumed to be reasonable, in contradiction to their analogous estimates for  $\mu_I$  (see Table 7.6) which agree neither with the experimental data nor with the estimates based on a single particle shell model (see Chapter 8). Thus, as long as no direct measurements of quadrupole moments for polonium isotopes are available, the above values can be assumed to be the best estimates. The nuclear moments for the odd-mass Po isotopes investigated in this work are compiled in Table 7.6.

Table 7.6 Nuclear moments for the odd-mass Po isotopes investigated.

mass number	$\mu_I$ [n.m.]	$Q$ [b]	reference
209	0.606(45)	—	this work
207	0.793(55) 0.27	0.28 0.29 (HF) 0.28 (OHFS)	[HWF 83] [OAL 61] [LR 74] [LR 74]
205	0.760(55) 0.26	0.17	[HWF 83] [OAL 61]

## 8 Discussion

### 8.1 Mean square charge radii

#### a) Global features

Of all the models describing the structure of nuclei in the ground state the droplet model [MS 69] has been so far found most successful in reproducing the experimental data, concerning both the macroscopic parameters, e.g. binding energies and the microscopic parameters: mean square charge radii and electric multipole moments. The original version of the model applied actually only to nearly spherical nuclei (so-called spherical droplet model - SDM, ignoring deformations) but later on the model was developed to include deformations [MS 83].

The droplet model gives a rather detailed description of both the neutron and the proton distributions. The radii of the sharp distributions are obtained by minimizing the macroscopic energy of the system; it follows that most nuclei have a neutron skin due to an excess number of neutrons (e.g. for Po the neutron skin thickness amounts to  $\sim 5\%$  of the equivalent sharp radius for the proton distribution). On the other hand, protons are "redistributed" due to Coulomb repulsion, so the actual distribution is somewhat more extended than the predicted uniform distribution. Due to diffuseness both the neutron and the proton distributions expand still further. The uniform distribution and the redistribution are shape-dependent, the contribution from the diffuseness, on the contrary, has no shape dependence and is constant for all the nuclei; therefore it is of no importance if only the changes of the square radii  $\delta \langle r^2 \rangle$  are concerned and not the square radii  $\langle r^2 \rangle$  themselves.

The size and shape of the proton distribution are accessible to experimental studies and on this basis the adequacy of the model can be checked. The spherical droplet model with the currently used standard set of parameters [MS 83] predicts  $\delta \langle r^2 \rangle$  values which are in good agreement with experimental ones, however, with an exception of the isotopes at and immediately above neutron shell closures, where the square charge radii increase more rapidly [cf. AFG 86]. To improve the overall agreement with the experiment a revised set of parameters was suggested [BT 85] which, however, makes only the slope steeper but doesn't reproduce the kink at the shell closures.

Another attempt towards a better description of the  $\delta \langle r^2 \rangle$  tendency was a semi-empirical formula of Wesołowski [We 85], being actually a droplet model formula including deformation and shell corrections. It has been found to reproduce the experimental data remarkably well [cf. AFG 86], in particular it predicts the kink at the shell closures.

The spherical droplet model (i.e. without including deformations) has been found to describe rather well the changes of the mean square charge radii  $\delta\langle r^2 \rangle$  in the vicinity of proton magic numbers, e.g. in Pb (one of the neighboring elements of Po) below the neutron shell closure at  $N=126$ . Therefore, having so far otherwise no means to determine  $\delta\langle r^2 \rangle$  in Po, we assumed a calibration based on the SDM:  $\delta\langle r^2 \rangle^{206, 208} \equiv \delta\langle r^2 \rangle^{206, 208}_{\text{SDM}} = -0.104 \text{ fm}^2$  (see Section 7.2) as long as there are no experimental data concerning  $\delta\langle r^2 \rangle$  or  $\langle r^2 \rangle$  or theoretical calculations of the electronic factor (formula (7.4); Hartree-Fock calculations are in progress [Fr 90]) available, which would provide a more reliable calibration of our results. The value assumed doesn't seem unpalatable when compared to the experimental  $\delta\langle r^2 \rangle$  values in the neighboring elements for the isotope pairs with the same neutron numbers  $N=122$  and  $124$  (Table 8.1). The same procedure has been also applied to obtain  $\delta\langle r^2 \rangle$  values from the isotope shifts in thallium [BBC 87].

The  $\delta\langle r^2 \rangle$  in Po, evaluated with the assumption of the above scaling, are plotted in Fig.8.1, together with the spherical droplet model predictions for the remaining isotope pairs. For comparison the predictions of the SDM with a revised set of parameters and of a Wesołowski formula are displayed. The error bars account for the neglect of the mass effect in isotope shifts, and thus cannot be understood as *independent* for each value; they rather determine the lower and upper limit of the range within which the whole pattern can be shifted. In order to account for the uncertainty of the calibration all the error values would have to be increased by a certain fraction of the corresponding  $\delta\langle r^2 \rangle$  values so that the whole pattern might be tilted about the zero point within the limits determined in this way. The standard SDM describes the tendency in changes of the mean square charge radii in Po quite well except for  $^{210}\text{Po}$ , which lies exactly at the neutron shell closure, and  $^{200}\text{Po}$ , where already some onset of permanent deformation is expected [MGK 86]. The same statement might also apply to the revised SDM if this were taken for calibration. There is, however, one argument against doing so, namely that the predicted  $\delta\langle r^2 \rangle$  values are generally larger than the experimental  $\delta\langle r^2 \rangle$  values found in the neighboring elements; in particular  $\delta\langle r^2 \rangle^{206, 208} = -0.132 \text{ fm}^2$  which is considerably larger than any of the values listed in Table 8.1 and thus not very plausible.

Wesołowski formula predicts in general slightly lower  $\delta\langle r^2 \rangle$  values than the standard SDM; since our calibration is not absolute, it cannot be said whether it really describes the variation of the mean square charge radii better than the droplet model, as in the case of some other elements. Because the polonium isotope chain investigated ends exactly at the shell closure at  $N=126$ , also the kink, predicted by the formula, could not be observed.

Table 8.1 Experimental  $\delta \langle r^2 \rangle$  for the isotope pairs with  $N=122$  and  $124$  in the elements in the vicinity of Po.

element	Z	$\delta \langle r^2 \rangle_{N=122, N'=124}$	reference
Hg	80	0.1018 ( 5)	[UBD 86]
Pb	82	0.1052 (28)	[AFG 86]
Rn	86	0.0982 ( 3)	[Ot 89]
Fr	87	0.09286(12)	[CCT 87]
Ra	88	0.083 (29)	[AKN 88]

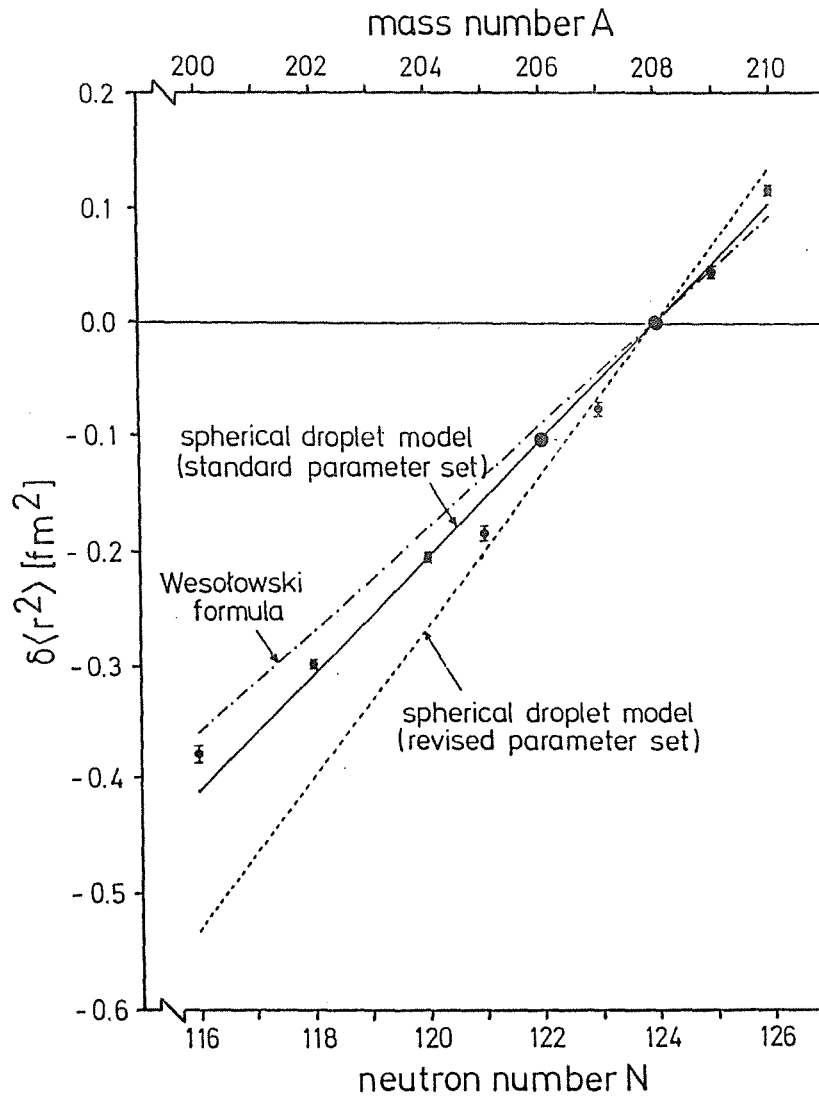


Fig.8.1 Changes of the mean square charge radii in Po evaluated as described in the text. Predictions of the spherical droplet model with a standard and revised set of parameters and of a Wesolowski formula are also displayed for comparison.

According to the standard spherical droplet model the root mean square charge radius of  $^{208}\text{Po}$  (our reference isotope) amounts to  $\langle r^2 \rangle_{208}^{1/2} = 5.557 \text{ fm}$ .

b) Deformation

Change in the mean square charge radius can be a result of a change of both the nuclear volume and shape. Deformations occur mainly for the nuclei far from shell closures for both protons and neutrons; there are e.g. whole regions in the periodic table exhibiting certain kinds of deformation (octupole deformation in Ra-Th region [CTT 85, CTT 87, WAK 87, AKN 88, Kä 88]). Recently, however, evidence has been gathered of existence of permanent quadrupole deformation just below the proton shell closure at  $Z=82$  (neutron deficient isotopes of Hg [BHK 76, UBD 86], Au [WBB 87, WBD 87] and Pt [DSB 86]).

For a quadrupole deformation with axial symmetry the following relation applies:

$$\langle r^2 \rangle = \langle r^2 \rangle_{sph} + \langle r^2 \rangle_{def} = \langle r^2 \rangle_{sph} \left( 1 + \frac{5}{4\pi} \langle \beta^2 \rangle \right), \quad (8.1)$$

where  $\langle r^2 \rangle_{sph}$  is the spherical contribution to  $\langle r^2 \rangle$  (SDM [MS 69, MS 83]) and  $\beta_2$  - a deformation parameter;  $\beta_2 > 0$  means a prolate deformation,  $\beta_2 < 0$  - an oblate deformation. If the deformation parameter is small ( $|\beta_2| \ll 1$ ), which is often the case, an approximate expression is valid for changes of the mean square charge radii:

$$\delta \langle r^2 \rangle^{AA'} = \frac{5}{4\pi} \langle r^2 \rangle_{sph} \delta \langle \beta^2 \rangle^{AA'}. \quad (8.2)$$

The  $\beta_2$  parameters can be evaluated from the transition probabilities of  $0^+ \rightarrow 2^+$  nuclear transitions by means of an approximate formula:

$$\beta_2 = \frac{4\pi}{3Ze r_0^2} \sqrt{B(E2: 0^+ \rightarrow 2^+)}. \quad (8.3)$$

For polonium the data available, concerning the deformation of the ground state, is very scarce. The  $B(E2: 0^+ \rightarrow 2^+)$  value is known only for  $^{210}\text{Po}$ , as obtained from scattering of the deuterons [EBE 73] (in good agreement with theoretical predictions of the shell model including configuration mixing [ZG 85]); it corresponds to a very low value of the deformation parameter  $\beta_2 = 0.0139(14)$ , as quoted in a recent compilation of  $B(E2)$  values and related quantities [RMM 87]. The deformation is thus very small and the  $^{210}\text{Po}$  nucleus can be considered nearly spherical.

Möller and Nix [MN 81] tabulated theoretically calculated values of intrinsic quadrupole moments. The value for  $^{210}\text{Po}$  is 0.1 b; on the other hand, the  $Q_0$  value

from [RMM 87], evaluated from the experimental  $\beta_2$  value on the assumption that the nucleus is permanently deformed and may be treated as a rotational nucleus (this assumption need not necessarily be valid), is 0.448(45), i.e. over a factor of 4 larger. Because of this inconsistency the theoretical  $Q_0$  values for the further Po isotopes [MN 81] cannot be taken as a basis to estimate the deformations of the corresponding nuclei.

c) Odd-even staggering

The odd-even staggering has for a long time presented an unsolved problem in nuclear physics. In general, qualitative descriptions of the phenomenon considered the different influence of an unpaired neutron on one hand and a neutron pair on the other hand on the static [WHF 53] or dynamic quadrupole deformations [So 66, RS 71]. A further step towards the explanation of the effect was an assumption of polarization of the proton core by the valence neutrons [Za 71, Ta 84] or recently of the three- and four-body correlations in nucleon interactions [Za 85, ZRS 87]. Both these recent approaches give a relatively good agreement with experimental data for the elements near or at the proton shell closures (e.g. Pb [Ta 84, ZRS 87]).

In the former approach [Ta 84] various multipole terms of the proton- neutron interactions are considered for  $j^n$  neutron configurations, leading to excited states of the core with the spin  $I_0$ . It is found that only the terms of even parity ( $I_0$  even) exhibit odd-even effects; the polarization of the core is less effective if the number of the valence neutrons is odd. A formula describing the changes of the mean square charge radii is derived, containing a linear term, a quadratic term and a pairing term (the last one expresses the odd-even staggering):

$$\delta \langle r^2 \rangle^{n,0} = -nC - \frac{1}{2} n(n-1)A - \frac{B}{2} \left( \frac{1 - (-1)^n}{2} \right), \quad (8.4)$$

where  $n$  denotes the number of neutron holes in the last neutron shell (for Po the one which fills up at  $N=126$ ); since the effective interactions are not known, a semi-empirical parametrization of  $\delta \langle r^2 \rangle$  values is performed by means of a least-squares fit instead of microscopic calculations of the three parameters involved:  $A$ ,  $B$  and  $C$ . The tendency of  $\delta \langle r^2 \rangle$  for any particular element can be thus described better than e.g. by the droplet model, which does not predict any odd-even effects; however, since only one pairing parameter is used, the formula fails to reproduce correctly the staggering variations (e.g. in Pb [AFG 86]). This applies also to polonium.

The result of a least-squares fit of the Talmi's formula to the experimental data for Po is presented in Fig.8.2. Although there appears a good overall agreement, the

inspection of  $\Delta$  (or  $\gamma$ ) reveals a distinct difference between the experiment and the predictions of the formula.

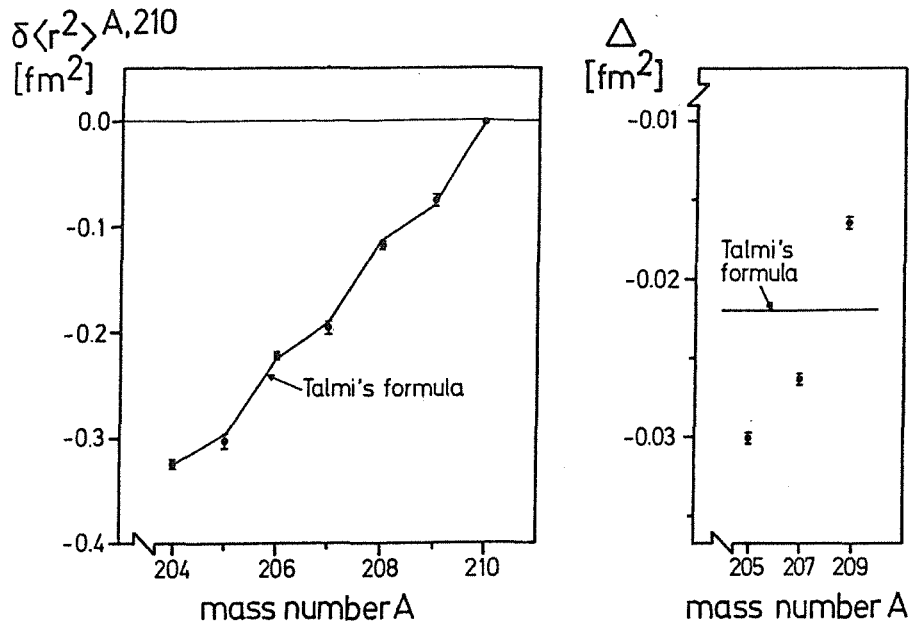


Fig.8.2 Comparison of the experimental data for Po to the predictions of the Talmi approach [Ta 84]: a) changes of the mean square charge radii  $\delta\langle r^2 \rangle$ , b) odd-even staggering parameter  $\Delta$ .

d) Comparison with the neighboring elements

Instead of comparing changes of the mean square charge radii in Po, which are based on an arbitrary scaling, to these in the neighboring elements, we do it rather with the relative isotope shifts [cf. BRH 85] which are experimental quantities. Fig.8.3 presents such a comparison. The isotope shifts have been normalized in the following way:  $\delta v^{N,N'=124} / \delta v^{N=122,N'=124}$ . Since the mass effect, wherever it is known, proves to be small (Hg: [UBD 86], Pb: [AFG 86]) and the same is assumed about Po, the relative isotope shifts are approximately equal to the relative changes of the mean square charge radii.

It can be seen that all these elements exhibit very similar tendencies. The isotope shifts for even-N isotopes tend to decrease with a decreasing neutron number; on the other hand, upon addition of a neutron pair which fills up the shell at  $N=126$  the isotope shift increases steeper (by about 15 - 20%) so that there appears a discontinuity. In the isotope shifts of the odd-N isotopes another important regularity becomes clear, namely an odd-even staggering. It becomes the more pronounced, the further an isotope lies below the neutron shell closure at  $N=126$

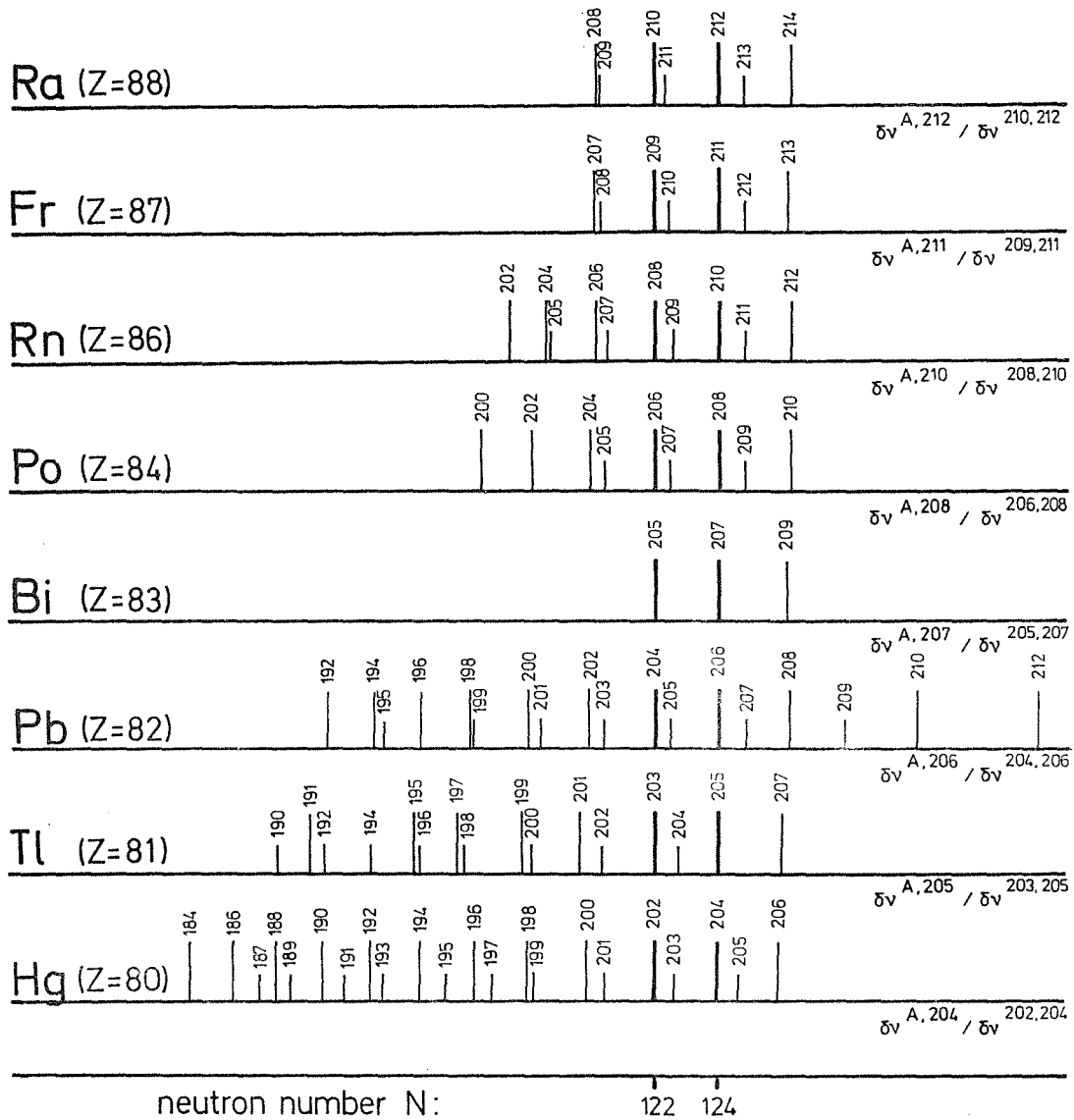


Fig.8.3 Relative isotope shifts for the elements in the vicinity of Po; the isotope shifts between the isotopes with  $N = 122$  and  $124$  have been set equal for all the elements. The isotope shift data are taken from: Hg: [UBD 86], Tl: [BBC 87, MDB 90], Pb: [AFG 86, DEH 88], Bi: [BRS 85], Po: this work, Rn: [BNO 87], Fr: [CTT 85], Ra: [WAK 87].

(i.e. the larger the number of neutron holes). In the case of Pb it can also be seen that the staggering is considerably reduced just above the shell closure. This decrease couldn't be, unfortunately, checked in the case of Po as the isotopes with the mass numbers  $A > 210$  have very short lifetimes and are thus unsuited for off-line studies. The former feature, i.e. the increase of staggering upon increasing the number of neutron holes, however, is visible; for quantitative description the odd-even staggering parameter  $\Delta$  is best suited (see Table 7.4).

Interesting feature of the relative variation of the mean square charge radii in Po is revealed when compared to these observed in Pb - the element with a magic proton

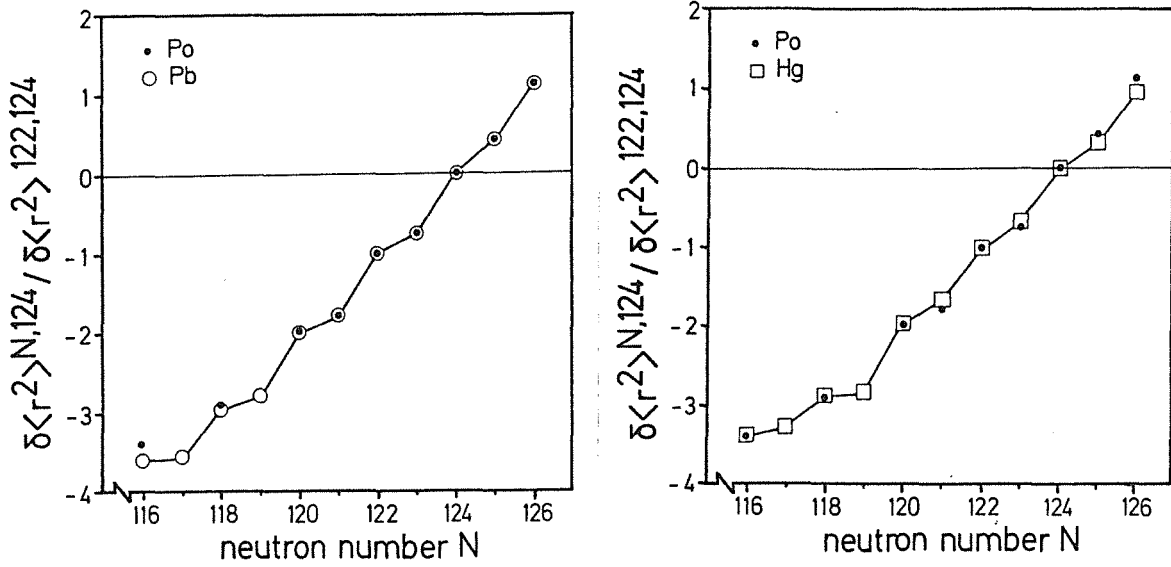


Fig.8.4 Relative variation of the mean square charge radii in Po and neighboring elements: Pb and Hg.

number  $Z=82$ , known to have nearly spherical nuclei all along the isotope chain investigated so far (Fig. 8.4). The relative isotope shifts in Po agree to better than 2% with these in Pb down to the neutron number  $N=120$ ; at  $N=118$  ( $^{202}\text{Po}$ ) a deviation of 6% is observed, which increases to 20% at  $N=116$  ( $^{200}\text{Po}$ ). Such a deviation might be the result of some kind of deformation. When relative  $\delta\langle r^2 \rangle$  in Po are compared to these of Hg - an element lying at the same distance from the proton shell closure at  $Z=82$  as Po, the overall agreement is not that striking as in the case of Pb (especially deviations occur for odd-mass isotopes - the odd-even staggering seems to be more pronounced in Po than in Hg) but, on the other hand, it greatly improves for the two most neutron-deficient isotopes with  $N=118$  and  $116$ .

## 8.2 Nuclear moments

The ground state configurations of  $^{205}\text{Po}$ ,  $^{207}\text{Po}$  and  $^{209}\text{Po}$  predicted by the shell model are:

$$(\pi h_{9/2})^2_0 (\nu p_{1/2})^2_0 (\nu f_{5/2})^3_{5/2}; I=5/2,$$

$$(\pi h_{9/2})^2_0 (\nu p_{1/2})^2_0 (\nu f_{5/2})^1_{5/2}; I=5/2,$$

$$(\pi h_{9/2})^2_0 (\nu p_{1/2})^1_{1/2}; I=1/2,$$

respectively. The single particle shell model predictions of the magnetic dipole moments (Schmidt values) are in some cases found to agree fairly well with the experimental values; on the other hand, there are also cases known where the single particle model fails, indicating that the interactions with the core nucleons cannot always be neglected. The agreement between the calculated "effective"

magnetic moments and the experimental ones is usually much better, if instead of  $g$ -factors for free nucleons so-called "effective"  $g$ -factors are used. Bauer et al. [BSK 73] performed such calculations for a number of nuclear states in the vicinity of  $^{208}\text{Pb}$ . Polonium is not explicitly included, so the results cannot be quoted directly, but the effective magnetic dipole moments for identical neutron configurations in  $^{207}\text{Pb}$  can be adopted for comparison. In Table 8.2 they are compared to the Schmidt values and the experimental values for Po.

In the case of  $^{209}\text{Po}$  the single particle shell model prediction is in a good agreement with the experimental magnetic moment obtained from our HFS measurements. The effective magnetic moment differs from the experimental value by more than the experimental error limit, the discrepancy is, however, not large, being  $\sim 9\%$ . For both  $^{205}\text{Po}$  and  $^{207}\text{Po}$  the single particle values fail to give a good description of the actual magnetic moments: they exceed the experimental values by 70 - 80%. On the contrary, the effective magnetic moment values differ from the experimental ones again by only  $\sim 10\%$ .

Table 8.2 Magnetic dipole moments for the odd-mass Po isotopes: predictions of the shell model and experimental values.

mass number	state	$\mu_I^{s.p.}[\text{n.m.}]$	$\mu_I^{eff}[\text{n.m.}]$	$\mu_I^{exp}[\text{n.m.}]$
209	$P_{1/2}$	0.638	0.553	0.606(45)
207	$f_{5/2}$	1.366	0.851	0.793(55)
205	$f_{5/2}$	1.366	0.851	0.760(55)

As far as the electric quadrupole moments are concerned, our data provide no new information. The  $Q$  values for  $^{205}, ^{207}\text{Po}$ , calculated from the hyperfine  $B$  factors of the electronic ground state [OAL 61], are compared by the authors with the predictions of the individual particle model and found consistent with them.

## 9 Concluding remarks

This work reports on isotope shift and hyperfine structure measurements for a series of polonium isotopes ( $^{200}\text{Po}$ ,  $^{202}\text{Po}$  and  $^{204-210}\text{Po}$ ) by laser induced resonance fluorescence on an atomic beam in the optical transition  $6p^4 \ ^3P_2 \rightarrow 6p^3 7s \ ^5S_2$  ( $\lambda = 255.8 \text{ nm}$ ). The experimental procedure applies intracavity frequency doubling in order to produce coherent UV light; for this purpose a commercial ring dye laser

system has been rebuilt. The measured isotope shifts reflect the relative changes of the nuclear mean square charge radii. These are found to be in good agreement with the predictions of the spherical droplet model down to the neutron number  $N=120$ ; for more neutron-deficient isotopes deviations occur, suggesting the onset of deformation in these nuclides. A striking agreement is found between the relative  $\delta\langle r^2 \rangle$  values in polonium and lead for *all* the isotopes with neutron numbers 120 - 126. The absolute  $\delta\langle r^2 \rangle$  values, obtained by a calibration based on the spherical droplet model, should be considered to be preliminary. A more reliable calibration of our isotope shifts results will be possible as soon as the Hartree-Fock calculations [Fr 90] are completed.

The hyperfine splittings of the ground state in  $^{205}\text{Po}$  and  $^{207}\text{Po}$  agree well with the more precise atomic beam magnetic resonance measurements [OAL 61]. From the ground state splitting in  $^{209}\text{Po}$ , determined for the first time with a high accuracy, the nuclear magnetic dipole moment of this nuclide can be deduced, which is found to agree with both the Schmidt value and the predicted "effective" magnetic moment [BSK 73].

## APPENDIX

### Second harmonic generation

The most important condition for efficient second harmonic generation is that the second harmonic beam and the fundamental beam are in phase with one another, which in turn means, that fundamental and second harmonic should propagate with the same phase velocity (phase-matching condition). In certain cases this condition can be fulfilled in nonlinear crystals at a certain angle  $\Theta_m$  with respect to the optic axis, called phase-matching angle. In the most common case of so-called type I phase matching (fundamental : oo, second harmonic : e) the phase-matching angle is given by the formula :

$$\Theta_m = \arcsin \left[ \frac{(n_o(2\omega))^{-2} - (n_o(\omega))^{-2}}{(n_e(2\omega))^{-2} - (n_o(\omega))^{-2}} \right]^{1/2} \quad (\text{A.1})$$

If  $\Theta_m = 90^\circ$  (refractive index surfaces don't intersect but are tangent to each other) fundamental and second harmonic propagate in the same direction; in all other cases - because of birefringence - the second harmonic beam, being e-polarized, propagates at an angle  $\Theta = \Theta_m + \rho$  with respect to the optic axis, i. e. in the direction of the normal vector to the index surface. The angle  $\rho$ , called the walk-off angle, is given by the formula :

$$\rho = \arctg \frac{\left[ \left( \frac{n_o(2\omega)}{n_e(2\omega)} \right)^2 - 1 \right] \text{tg} \Theta_m}{1 + \left( \frac{n_o(2\omega)}{n_e(2\omega)} \right)^2 \text{tg}^2 \Theta_m} \quad (\text{A.2})$$

The fact that fundamental and second harmonic propagate in slightly different directions reduces the frequency doubling efficiency in all cases with  $\Theta_m \neq 90^\circ$ , especially for highly birefringent crystals. The case  $\Theta_m = 90^\circ$  is called non-critical, because the refractive index matching is maintained over a relatively wide range of wavelengths (about a few nm), while  $\Theta_m \neq 90^\circ$  is called a "critical" phase matching.

According to [BK 68] the generated second harmonic power can be expressed as follows :

$$P(2\omega) = K P^2(\omega) l k(\omega) e^{-\alpha l} h(\sigma, \beta, x, \xi, \mu) = C P^2(\omega) \quad (\text{A.3})$$

where:

$$K = \frac{2\omega^2}{n_o^2(\omega) n_e(2\omega) c^3 \epsilon_o} d_{eff}^2 \quad (\text{A.4})$$

with

$l$  - crystal length

$k(\omega)$  - propagation constant for the fundamental

$\alpha'$  - absorption parameter ( $\alpha' = \alpha(\omega) + \frac{1}{2}\alpha(2\omega)$ )

$d_{eff}$  - effective optical nonlinear constant and

$P(\omega)$  - fundamental power.

Only the function  $h$  in (A.3) is discussed in more detail in what follows, since other values are clear. Parameters which enter the function  $h$  represent the following properties:

$\sigma$  - phase mismatch between the fundamental and second harmonic,

$\beta$  - double refraction of the crystal,

$\kappa$  - absorption parameter,

$\xi$  - focusing of the fundamental beam and

$\mu$  - position of the focus inside the crystal.

The parameters  $\sigma$  and  $\kappa$  can be optimized and they are assumed to have their best values in what follows;  $\beta$  and  $\xi$  are determined by the given crystal type.  $\kappa$  is assumed to be irrelevant, i.e. no absorption is assumed throughout. In practical cases two of the above parameters are of particular interest:

$$\xi = \frac{l}{w_o^2 k(\omega)} \quad , \quad (\text{A.5})$$

called the focusing parameter, and

$$\beta = \frac{2\rho}{w_o k(\omega)} \quad ; \quad (\text{A.6})$$

$w_o$  is the fundamental beam waist size. Instead of  $\beta$ , often the so-called double-refraction parameter  $B$  is used:

$$B := \frac{\beta}{\sqrt{\xi}} = \frac{\rho \sqrt{lk(\omega)}}{2} \quad (\text{A.7})$$

For a given crystal type (i.e. given  $\rho$ ) there always exists optimum focusing, where the function  $h$  has its maximum - it is a compromise between high fundamental power density (which requires a small waist with the disadvantage of a high angular divergence) and small beam divergence in order to maintain the angular phase matching condition (which on the other hand required a large waist). In the case  $\Theta_m \neq 90^\circ$  a small beam divergence is of particular importance, because the phase matching condition is already affected by the birefringence, therefore weaker focusing is preferred in comparison to the case  $\Theta_m = 90^\circ$ . The dependences of  $h$  on  $B$  and  $\xi$  is presented in fig.A.1. It can be seen, that optimization with respect to  $\xi$  is often not very critical, which is an important fact to note in the case of intracavity frequency doubling, where the waist size is determined by the optical configuration of the resonator.

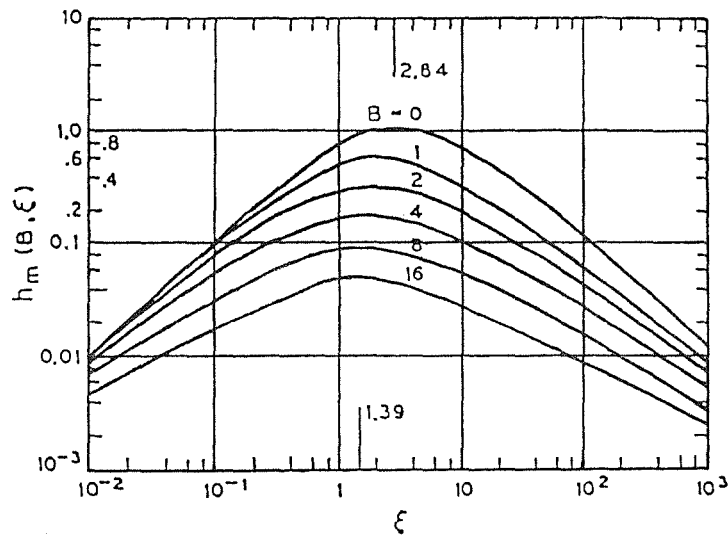


Fig. A.1 Dependence of the function  $h_m(B, \xi)$  on the focusing parameter  $\xi$  for various double refraction parameter ( $B$ ) values; subscript 'm' means that the other parameters ( $\sigma$  and  $\xi$ ) have been optimized and no absorption ( $\kappa$ ) is assumed [BK 68, fig.2].

Intracavity frequency doubling in the CR 699-21 resonator by means of a BBO crystal of length  $l=5$  mm (see Section 3.5) can be considered a case of weak focusing ( $\xi = 0.2 < 0.4$ ), so for determining of further interesting properties of the generated second harmonic beam, beside the power, an approximate theory [BAD 65] can be applied. In this limit the fundamental beam in a rough approximation is considered as a plane-parallel wave all along the crystal so far as its divergence

is concerned. The neglect of the beam divergence is justified especially in the case of highly birefringent crystals, where the walk-off angle  $\rho \gg \delta_0$ , the latter being the fundamental beam far field half-angle. In our case  $\rho = 4.86^\circ$  (see Section 3.5) while  $\delta_0 = 0.21^\circ$ .

Second harmonic generation in the critical phase matching case takes place mainly into the direction half-way between the propagation directions of the fundamental and second harmonic (the latter is called walk-off direction). This can be seen from fig.A.2 [BAD 65, fig.5], which presents the second harmonic intensity on the exit surface of the crystal along the line being the intersection of this surface and the phase matching plane. As a dimensionless parameter the so-called normalized thickness  $t$  is introduced:

$$t = \frac{\sqrt{2} \rho l}{n_o} , \quad (\text{A.8})$$

which is a measure of the distance between the exit points of the fundamental and second harmonic, starting from a common point on the entrance surface. It can be seen that for  $t \gg 1$  (in our case  $t = 22.2 \gg 1$ ) actually the whole second harmonic intensity is spread rather homogeneously between the fundamental beam and walk-off directions. As a consequence, the second harmonic beam is not a Gaussian beam: it has a Gaussian intensity distribution in the direction perpendicular to the phase-matching plane (vertical direction) with a beam radius  $w_{vert}$  on the exit surface

$$w_{vert} = w_0 \quad (\text{A.9a})$$

and an almost rectangular intensity distribution in the phase-matching plane (horizontal direction) with a corresponding beam radius  $w_{horiz}$

$$w_{horiz} = \frac{tw_0}{2} = \frac{\rho l}{\sqrt{2}} . \quad (\text{A.9b})$$

The ratio  $w_{horiz}/w_{vert}$  is called "aspect ratio"  $A$

$$A = \frac{\rho l}{\sqrt{2} w_0} ; \quad (\text{A.10})$$

it is a measure of the beam elongation in the walk-off direction on leaving the crystal (for non-astigmatic Gaussian beams  $A = 1$ ). Because the beam divergence

is inversely proportional to the waist size, in the far field the second harmonic beam is elongated in the vertical direction.

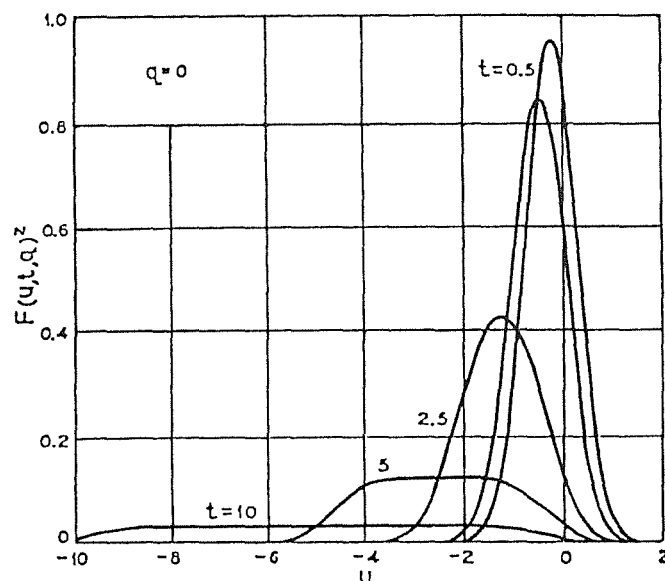


Fig. A.2 Second harmonic intensity on the exit surface of the crystal for various  $t$  values;  $u$  is a dimensionless variable ( $u = -\sqrt{2}(\rho x/w_0)$ , where  $x$  is a coordinate in the phase-matching plane representing the distance from the exit point of the fundamental) [BAD 65, fig.5].

In the case of weak focusing and high birefringence the following asymptotic expression for the second harmonic power is obtained (formula (2.46) in [BAD 65] )

$$P(2\omega) = \frac{\sqrt{\pi} \rho l}{w_0} K P^2(\omega) \quad . \quad (A.11)$$

Temperature and angular sensitivities of a frequency doubling process are defined as follows [EDV 87]:

$$\beta_{\Theta} = \left. \frac{\delta \Delta k}{\delta \Theta} \right|_{\Theta = \Theta_m} \quad (A.12a)$$

$$\beta_T = \left. \frac{\delta \Delta k}{\delta T} \right|_{T = T_0} \quad (A.12b)$$

$\Delta k$  being the wave-vector mismatch between the fundamental and second harmonic:  $k = 2k(\omega) - k(2\omega)$ . From these one can obtain the temperature and angular bandwidths for SHG:

$$\Delta\Theta = \frac{kA}{l\beta_{\Theta}} \quad (\text{A.13a})$$

$$\Delta T = \frac{kA}{l\beta_T} \quad (\text{A.13b})$$

where the constant  $A$  depends on that how the bandwidth is defined; for FWHM bandwidth  $A = 1.39155738$ .

The frequency bandwidth can be calculated as follows:

$$\Delta\nu = \frac{\Delta\Theta}{\left(\frac{\delta\Theta}{\delta\nu}\right)} \quad (\text{A.14})$$

where  $\delta\Theta/\delta\nu$  is the angular dispersion.

## References

- [ABH 86] M.Anselment, K.Bekk, A.Hanser, H.Hoeffgen, G.Meisel, S.Göring, H.Rebel, G.Schatz, Phys. Rev. C 34(1986)1052
- [AFG 86] M.Anselment, W.Faubel, S.Göring, A.Hanser, G.Meisel, H.Rebel, G.Schatz, Nucl. Phys. A 451(1986)471
- [AHS 87] P.Aufmuth, K.Heilig, A.Steudel, At. Data Nucl. Data Tab. 37(1987)456
- [AKN 88] S.A.Ahmad, W.Klempt, R.Neugart, E.W.Otten, P.-G.Reinhard, G.Ulm, K.Wendt and the ISOLDE Collaboration, Nucl. Phys. A 483(1988)244
- [AO 61] S.Axensten, C.M.Olsmats, Ark. f. Fys. 19(1961)461
- [BAD 65] G.D.Boyd, A.Ashkin, J.M.Dziedzic, D.A.Kleinman, Phys. Rev. 137(1965)A1305
- [BBC 87] J.A.Bounds, C.R.Bingham, H.K.Carter, G.A.Leander, R.L.Mlekodaj, E.H.Spejewski, Phys. Rev. C 36(1987)2560
- [BBP 87] S.A.Blundell, P.E.G.Baird, C.W.P.Palmer, D.N.Stacey, J. Phys. B 20(1987)3663
- [BFG 89] C.J.Batty, E.Freidman, H.J.Gils, H.Rebel, Adv. Nucl. Phys. 19(1989)1
- [BHK 76] J.Bonn, G.Huber, H.-J.Kluge, E.W.Otten and the ISOLDE Collaboration, Z. Phys. A 276(1976)203
- [BK 68] G.D.Boyd, D.A.Kleinman, J. Appl. Phys. 39(1968)3597
- [BNO 87] W.Borchers, R.Neugart, E.W.Otten, H.T.Duong, G.Ulm, K.Wendt and the ISOLDE Collaboration, Hyp. Int. 34(1987)25
- [Bo 88] M.G.Boshier, Ph.D. Thesis, Oxford University 1988 (unpublished)
- [Br 70] S.Brandt, Statistical and Computational Methods in Data Analysis, North-Holland Publishing Company, Amsterdam-London (1970)
- [BRS 85] M.Barboza-Flores, O.Redi, H.H.Stroke, Z. Phys. A 321(1985)85
- [BSK 73] R.Bauer, J.Speth, V.Klemt, P.Ring, E.Werner, T.Yamazaki, Nucl. Phys. A 209(1973)535
- [BT 85] D.Berdichevsky, F.Tondeur, Z. Phys. A 322(1985)141

- [Bü 84] S.Büttgenbach, Hyp. Int. 20(1984)1
- [CCT 85] A.Coc, C.Thibault, F.Touchard, H.T.Duong, P.Juncar, S.Liberman, J.Pinard, J.Lerme, J.L.Vialle, S.Büttgenbach, A.C.Mueller, A.Pesnelle and the ISOLDE Collaboration, Phys. Lett. B 163(1985)66
- [CCT 87] A.Coc, C.Thibault, F.Touchard, H.T.Duong, P.Juncar, S.Liberman, J.Pinard, M.Carre, J.Lerme, J.L.Vialle, S.Büttgenbach, A.C.Mueller, A.Pesnelle and the ISOLDE Collaboration, Nucl. Phys. A 468(1987)1
- [Ch 66] G.W.Charles, JOSA 56(1966)1292
- [CWJ 85] Chen Chuangtian, Wu Bochang, Jiang Aidong, You Guiming, Sci. Sinica B 28(1985)235
- [DCH 75] C.F.Dewey, W.R.Cook, R.T.Hodgson, J.J.Wynne, Appl. Phys. Lett. 26(1975)714
- [De 73] W.Demtröder, Phys. Rep. 7C(1973)224
- [De 76] H.J.Dewey, IEEE J. Quant. Electr. QE-12(1976)303
- [DEH 88] U.Dinger, J.Eberz, G.Huber, R.Menges, S.Schröder, R.Kirchner, O.Klepper, T.Kühl, D.Marx, G.D.Sprouse, GSI Report 88-1 (1988), p.17
- [DKM 90] A.Dorn, W.Kälber, G.Meisel, KfK Report 4709B(1990)
- [DSB 86] G.D.Dracoulis, A.E.Stuchbery, A.P.Byrne, A.R.Poletti, S.J.Poletti, J.Gerl, R.A.Bark, J. Phys. G 12(1986)L97
- [DTS 73] F.B.Dunning, F.K.Tittel, R.F.Stebbins, Opt. Comm. 7(1973)181
- [EBE 73] C.Ellegaard, P.D.Barnes, R.Eisenstein, E.Romberg, T.S.Bhatia, T.R.Canada, Nucl. Phys. A 206(1973)83
- [EDV 87] D.Eimerl, L.Davis, S.Velsko, E.K.Graham, A.Zalkin, J. Appl. Phys. 62(1987)1968
- [FH 90] B.Feurer, A.Hanser, KfK Report 4660(1990), Contr. 3.4
- [Fr 90] B.Fricke, private communication
- [GL 78] S.Gerstenkorn, P.Luc, Atlas du Spectre d'Absorption de la Molécule d'Iode, Centre National de la Recherche Scientifique, Paris, 1978
- [GWU 87] GWU Lasertechnik, private communication

- [HBD 78] J.M.Halbout, S.Blit, W.Donaldson, IEEE J. Quant. Electr. **QE-15** (1978)1176
- [HWF 83] P.Herzog, H.Walitzki, K.Freitag, H.Hildebrand, K.Schlösser, Z. Phys. A **311**(1983)351
- [Ka 86] K.Kato, IEEE J. Quant. Electr. **QE-22**(1986)1013
- [Kä 88] W.Kälber, Ph.D. Thesis, Universität Heidelberg 1988 (KfK Report 4513(1989))
- [Kä 90] W.Kälber, private communication
- [Ki 84] W.H.King, "Isotope Shift in Atomic Spectra", Plenum Press, New York 1984
- [KID 72] H.W.Kogelnik, E.P.Ippen, A.Dienes, Ch.V.Shank, IEEE J. Quant. Electr. **QE-8**(1972)373
- [Ko 56] H.Kopfermann, "Kernmomente", Akademische Verlagsgesellschaft, Frankfurt a.M. (1956), p.247
- [Kn 87] D.Knauß, unpublished report, KfK 1987
- [Kr 80] H.Kriz, Diploma thesis, Universität Bonn 1980 (unpublished)
- [LJ 59] I.Lindgren, C.M.Johansson, Ark. f. Fys. **15**(1959)445
- [LR 74] I.Lindgren, A.Rosén, Case Studies At.Phys. **4**(1974)93
- [MDB 90] R.Menges, U.Dinger, N.Boos, G.Huber, S.Dutta, R.Kirchner, O.Klepper, T.Kühl, D.Marx, G.D.Sprouse, to be published
- [MGK 86] A.Maj, H.Grawe, H.Kluge, A.Kuhnert, K.H.Maier, R.A.Meyer, J.Recht, N.Roy, Z. Phys. A **324**(1986)123
- [MN 81] P.Möller, J.R.Nix, At. Data Nucl. Data Tabl. **26**(1981)165
- [MS 69] W.D.Myers, W.J.Swiatecki, Ann. Phys. **55**(1969)395
- [MS 83] W.D.Myers, K.-H.Schmidt, Nucl. Phys. A **410**(1983)61
- [NOR 84] W.Nazarewicz, P.Olanders, I.Ragnarsson, J.Dudek, G.A.Leander, P.Möller, E.Ruchowska, Nucl. Phys. A **429**(1984)269
- [OAL 61] C.M.Olsmats, S.Axensten, G.Liljegren, Ark. f. Fys. **19**(1961)469
- [Ot 89] E.W.Otten, in: Treatise on Heavy-Ion Science, vol.8: Nuclei far from Stability, p.517 ff; ed. D.A.Bromley, Plenum Press (1989)

- [Pi 89] P.Pietruk, Diploma thesis, Universität Karlsruhe 1989  
(unpublished)
- [Ra 89] P.Raghavan, *At. Data Nucl. Data Tabl.* **42**(1989)189
- [Re 89] H.Rebel, in: *Recent Advances in Nuclear Physics*, p.223 ff; eds.  
M.Petrovichi and N.V.Zamfir, World Scienc., Singapore-New  
Jersey- London-Hongkong (1989)
- [RMM 87] S.Raman, C.H.Malarkey, W.T.Milner, C.W.Nestor,Jr., P.H.Stelson,  
*At. Data Nucl. Data Tabl.* **36**(1987)1
- [RS 82] H.Rebel, G.Schatz, *Lasers in Nuclear Physics*, p.197 ff, eds.  
C.E.Bemis and H.K.Carter, Harwood Academic Publ., London -  
New York (1982)
- [RS 71] B.S.Reehal, R.A.Sorensen, *Nucl. Phys. A* **161**(1971)385
- [Sc 90] R.Schruft, Diploma thesis, Universität Karlsruhe 1990
- [Se 69] E.C.Seltzer, *Phys. Rev.* **188**(1969)1916
- [SKK 91] R.Schruft, W.Kälber, D.Kowalewska, G.Meisel, *KfK Report* 4875  
(1991), Contr. 3.3
- [So 66] R.A.Sorensen, *Phys. Lett.* **21**(1966)333
- [St 84] A.Steiger, *KfK Report* 3820(1984)
- [Ta 84] I.Talmi, *Nucl. Phys. A* **423**(1984)189
- [TAB 83] R.C.Thompson, M.Anselment, K.Bekk, S.Göring, A.Hanser,  
G.Meisel, H.Rebel, G.Schatz, B.A.Brown, *J. Phys. G* **9**(1983)443
- [UBD 86] G.Ulm, S.K.Bhattacharjee, P.Dabkiewicz, G.Huber, H.-J.Kluge,  
T.Kühl, H.Lochmann, E.-W.Otten, K.Wendt, S.A.Ahmad,  
W.Klempt, R.Neugart and the ISOLDE Collaboration, *Z. Phys. A*  
**325**(1986)247
- [WAK 87] K.Wendt, S.A.Ahmad, W.Klempt, R.Neugart, E.W.Otten,  
H.H.Stroke, *Z. Phys. D* **4**(1987)227
- [WB 77] A.H.Wapstra, K.Bos, *At. Data Nucl. Data Tab.* **19**(1977)177
- [WBB 87] K.Wallmeroth, G.Bollen, M.J.G.Borge, J.Campos, A.Dohn,  
P.Egelhof, J.Grüner, H.-J.Kluge, U.Krönert, F.Lindenlauf,  
R.B.Moore, A.Rodriguez, A.Venugopalan, J.L.Wood and the  
ISOLDE Collaboration, *Hyp. Int.* **34**(1987)21

- [We 85] E.Wesołowski, J. Phys. G 11(1985)909
- [WHF 53] L.Wilets, D.L.Hill, K.W.Ford, Phys. Rev 91(1953)1488
- [Za 71] L.Zamick, Ann. Phys. 66(1971)784
- [Za 85] D.Zawischa, Phys. Lett. B 155(1985)309
- [ZG 85] D.Zwarts, P.W.M.Glaudemans, Z. Phys. A 320(1985)487
- [Zi 85] D.Zimmermann, Z. Phys. A 321(1985)23
- [ZRS 87] D.Zawischa, U.Regge, R.Stapel, Phys. Lett B 185(1987)299

## Acknowledgements

The present work has been performed in the Institut für Kernphysik of the Kernforschungszentrum Karlsruhe. I would like to thank Prof. Dr. G. Schatz for enabling me to do this work and for his kind interest and encouragement. Kernforschungszentrum Karlsruhe has kindly supported my studies by a stipend.

I would like to thank all the members of the laser spectroscopy group: Dr. K. Bekk, DP S. Göring, Dr. A. Hanser, Dr. W. Kälber, Dr. G. Meisel, Prof. Dr. H. Rebel, DP J. Rink and Mr. R. Schruft for their help and assistance in all the experiments establishing the basis of this work.

I am especially thankful to Prof. Dr. H. Rebel for his stimulation toward this subject, his many valuable suggestions and encouragement, and Dr. G. Meisel for many fruitful discussions and support in all the problems concerning this work.

I would like to express my appreciation to Dr. A. Hanser and Mr. B. Feurer for constructing the atomic beam apparatus used in this work and their substantial contribution to all the undertaken modifications and improvements in handling radioactive nuclides.

I would like to thank Prof. Dr. J. Dembczynski of the Poznan Technical University for his kind support and encouragement to perform the laser spectroscopic studies in Kernforschungszentrum Karlsruhe.